Machine Learning Approaches for Adaptive Optics in Microscopy

Dissertation by Ivan Vishniakou
Supervised by Prof. Dr. Matthias B. Hullin

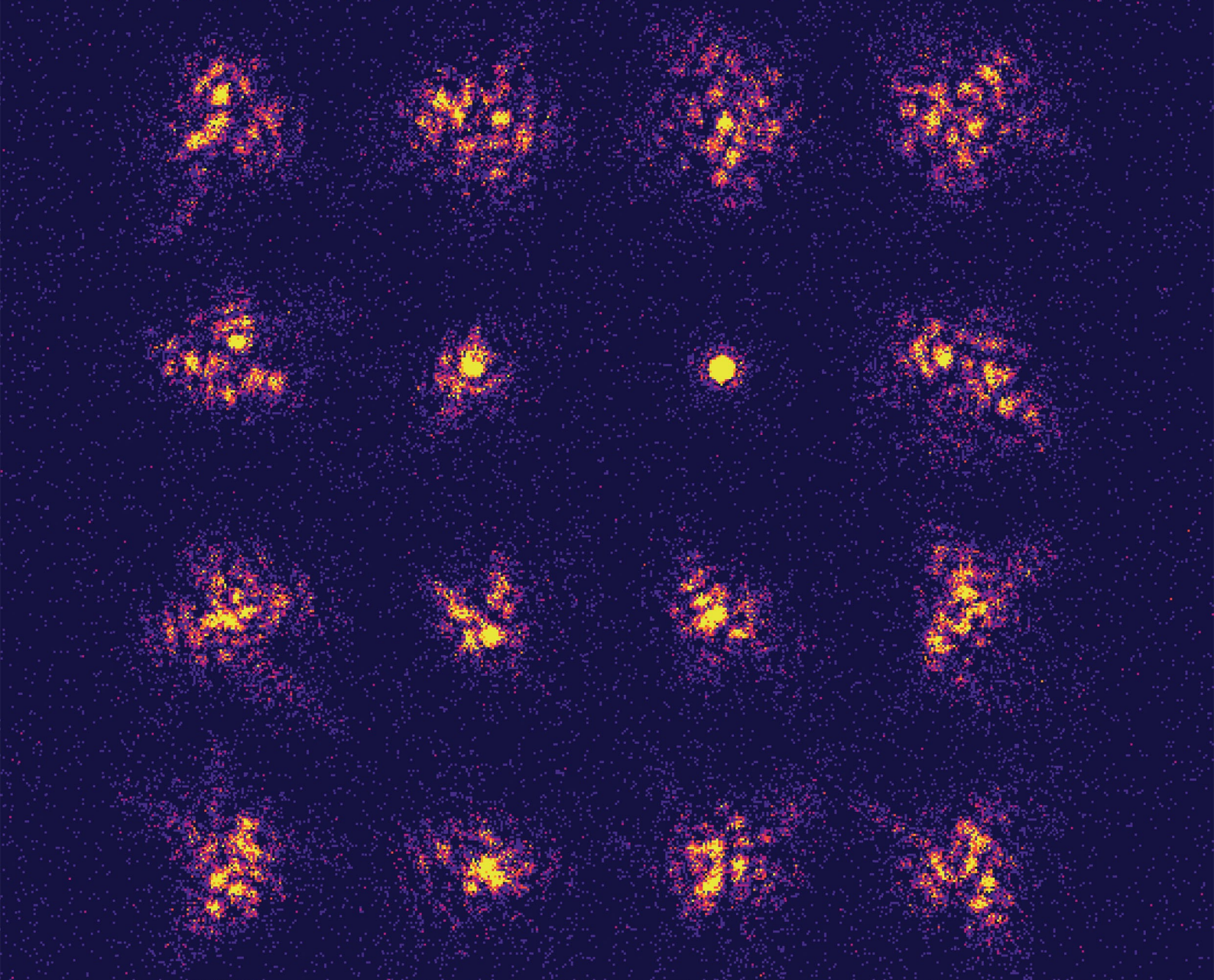

Bonn, 2023

Machine learning approaches for adaptive optics in microscopy

Dissertation

zur

Erlangung des Doktorgrades (Dr. rer. nat.)

der

Mathematisch-Naturwissenschaftlichen Fakultät

der

Rheinischen Friedrich-Wilhelms-Universität Bonn

vorgelegt von

Ivan Vishniakou

aus

Minsk, Belarus

Bonn, Dezember 2021

Angefertigt mit Genehmigung der
Mathematisch-Naturwissenschaftlichen Fakultät
der Rheinischen Friedrich-Wilhelms-Universität Bonn

1. Gutachter: Prof. Dr. Matthias Hullin
2. Gutachter: Prof. Dr. Reinhard Klein

Tag der Promotion: 04.07.2022
Erscheinungsjahr: 2023

Contents

Abstract

Microscopic imaging is an essential tool for science. For instruments that operate close to the physically possible diffraction limit, a main remaining challenge are aberrating operating conditions. For microscopy, such conditions are routinely encountered for example in biology, where tissue samples induce increasingly stronger aberrations with increasing imaging depth. Similar problems are also encountered in astronomy where atmospheric turbulences hinder ground-based telescopes.

Adaptive optics – a method originally developed for earthbound telescopes – can be applied in microscopy to compensate for sample-induced aberrations. However, a major challenge for microscopy lies in measuring aberrations and therefore in finding wavefront corrections.

This thesis presents machine learning methods developed for aberration sensing and correction compatible with two-photon laser scanning microscopy. A first approach uses deep learning with labelled datasets of focus images and corresponding aberrations. These datasets were created using a spatial light modulator, and were then used to train neural networks for detecting the aberrations in the system.

A second approach for adaptive optics was developed that uses optimization of a forward model to infer the unknown aberration. This technique relies on a mathematical model of image formation, including initially unknown aberration parameters. The actual aberrated system was probed by controlled light modulations and the computational model was matched to observations using gradient-based optimization, which was efficiently implemented using a machine learning framework with automatic differentiation and GPU-accelerated computing. This method was first demonstrated in a proof-of-principle experiment in two different configurations with scattered light and then using fluorescence in a two-photon laser scanning microscope.

List of abbreviations

AO	Adaptive Optics
BS	Beam Splitter
CNN	Convolutional Neural Network
DC	Dichroic Mirror
DIP	Deep Image Prior
DM	Deformable Mirror
DMD	Digital Micromirror Device
FFT	Fast Fourier Transform
FWHM	Full Width at Half Maximum
GPU	Graphics Processing Unit
MAE	Mean Absolute Error
MO	Microscope Objective
NA	Numerical Aperture
PH	Pinhole
PMT	Photomultiplier Tube
PSF	Point Spread Function
SHWS	Shack-Hartmann Wavefront Sensor
SLM	Spatial Light Modulator
SM	Scanning Mirror

Acknowledgements

During my PhD study I was blessed to receive a great deal of support and assistance from many people to whom I would like to express my sincere gratitude.

I would like to thank my supervisor Dr. Johannes Seelig for the opportunity to work in his research group and be involved in so many exciting projects, as well as for his guidance and encouragement through all my years of work at caesar.

I am very grateful to Prof. Dr. Matthias Hullin for his feedback and participation in my thesis advisory committee (TAC) meetings, and for serving as my thesis referee and giving me the chance to defend my thesis at the University of Bonn.

I would also like to thank Prof. Dr. Reinhard Klein for kindly agreeing to be the second referee of my thesis, as well as Prof. Dr. Thomas Schultz and Prof. Dr. Ulrich Kubitscheck for joining the examination committee.

I would like to thank Dr. Kevin Briggman for joining my TAC meetings and providing feedback, mentoring and guidance.

I am very grateful to my colleagues and friends who I met at the institute and with whom I shared many beautiful and fun moments. Finally, I express my profound gratitude to my parents and my brother for all the support and encouragement throughout my studies.

Thank you!

CHAPTER 1

Introduction

It is often said that a picture is worth a thousand words and indeed, looking at things is often the most intuitive way to understand them. This is reflected in the fact that imaging has become an invaluable tool in science for studying nature from the very small to the very large. The advancements in technology allow us to see better by perfecting optics and sensors, and to develop imaging systems that come close to the theoretically possible limits.

At the same time, computation and digital signal processing are now routinely used for improving imaging. By using prior knowledge about the image formation process, computational imaging can help gain information that goes beyond the limits of traditional optical systems (for example in lucky imaging in astronomy or super-resolution imaging in microscopy). Some methods even completely discard common optical elements (such as in lensless imaging or ghost imaging), relying on algorithms that can be extended to a very broad range of applications across imaging modalities (ultrasound, radio waves, etc.). Such close integration of computation and imaging for example enables affordable miniature mass-market cameras in every mobile device.

Similar to other computational imaging approaches, adaptive optics relies on the integration of computational algorithms and imaging systems. The goal of adaptive optics is to improve the signal-to-noise ratio and therefore the image quality in situations with weak signals resulting from non-ideal imaging conditions. Adaptive optics was originally developed to overcome such non-ideal imaging conditions in astronomy and to correct atmospheric aberrations in ground-based telescopes. However, it can also be applied similarly in microscopy, for example when dealing with scattering biological tissue.

In this thesis we present our experiments that combine computational as well as image

processing approaches with adaptive optics. In particular, the computational approaches take advantage of machine learning frameworks closely integrated with the simulation of the experimental imaging setups, with the goal of improving two-photon fluorescence microscopy under non-ideal imaging conditions.

1.1 Background

Obtaining an image with traditional optics means collecting light coming from a scene with a lens and focusing it into an image. The resulting image can be recorded with a detector which registers the intensity and potentially color of light arriving in different locations or pixels. This is the basic principle underlying photography, valid for manual tracing of images with a camera obscura [1] as much as for modern digital cameras with photosensitive electronic detectors that almost instantaneously read out the signal and save it in digital format ready to view or process. The quality of an image can be judged by how accurately it captures a scene, be that geometry, color, or also the amount of detail or resolution. With increasing resolution, finer details of an object can be distinguished in the image. This is especially important in a scientific context, where imaging is used to study the unknown, for example far away objects in space viewed through a telescope or when looking with a microscope at very small structures.

In this introduction we briefly cover the physics of image formation as relevant for optical microscopy, describe the phenomena that can disturb it, and how they can be counteracted or corrected. This description and reasoning are carried out in the framework of Fourier (wave) optics [2].

1.1.1 Wave optics

Light propagating in free space is described by a complex-valued function of coordinates and time $U(\mathbf{r},t)$ which satisfies the wave equation. Solving for this wave function using separation of variables results in a solution that is a product of a time-dependent high frequency oscillation, with the frequency of light ν, and a complex amplitude $U(\mathbf{r})$ which is only position dependent:

$$U(\mathbf{r},t) = U(\mathbf{r}) \exp(j2\pi\nu t).$$

For optical waves the frequency of the time component lies in the range of 10^{11} – 10^{16} Hz, making it challenging to measure individual oscillations [3], and therefore typically

time-averaged intensities, equal to the absolute square of the complex amplitude, are recorded [4, chapter 2.2]:

$$I(\mathbf{r}) = |U(\mathbf{r})|^2.$$

A sensor or photosensitive material responds in proportion to this quantity, and for modelling of imaging applications therefore solving for and analyzing this complex amplitude is sufficient. The complex amplitude $U(\mathbf{r})$ needs to satisfy the time-independent homogeneous Helmholtz equation

$$\nabla^2 U + k^2 U = 0.$$

This equation can be solved analytically for some elementary cases like a plane wave or a spherical wave. Due to the linearity of the Helmholtz equation, any solution can be expressed as a superposition of elementary solutions, for example plane waves. A plane wave solution describes a wave propagating in the direction of the wave vector $\mathbf{k}$ [4, Chapter 2.2]:

$$U(\mathbf{r}) = A \exp(-j\mathbf{k} \cdot \mathbf{r}) = A \exp[-j(k_x x + k_y y + k_z z)].$$

Although true plane waves, as defined here, are not encountered in nature (since they extend laterally to infinity), close approximations over some finite volume exist, for example light arriving from a distant point source to an observer.

Another concept used in the following is that of **wavefront**. A wavefront is defined as a surface of equal phase of optical waves, and for a plane wave it is a sequence of planes separated in space by a wavelength. The direction of propagation of light is normal to the wavefront at every point, so a plane wave describes a beam of parallel rays.

An arbitrary wave can be described as a complex amplitude defined over a region of interest, for example over the entrance pupil of an optical system. Alternatively, it can also be represented as a composition of plane waves travelling in different directions, which is called the angular spectrum of plane waves. This representation allows to calculate the evolution of the wave along its travelling direction. The spectrum of plane waves is a distribution of complex amplitudes and corresponding angles of propagation direction with respect to the optical axis. All the plane waves are propagated by the free space transfer function dependent on the travel distance and are finally summed again to reconstruct the complex amplitude in the new plane (angular spectrum method [5, Chapter 3]).

The calculus of complex amplitudes also conveniently reflects wave interactions: constructive or destructive interference depending on whether complex amplitudes are summed in phase or out of phase, respectively. Optical elements can be represented as complex transmission factors applied to the complex amplitude of the wave. In this case, the magnitude represents light permeability (apertures, masks), and the phase leads to phase changes due to refractive elements (lenses, aberrations). Together with the mentioned method to compute light propagation between these optical elements, this offers a complete framework for modelling light propagation in an optical system.

For modelling the polarization of light and its effects, independent polarization components have to be represented as independent complex amplitudes, taking into account relative phase offsets and magnitudes to reflect different possible polarization states.

1.1.2 Imaging systems and aberrations

Projection of an image with a (convex) lens relies on focusing light by changing its direction of propagation. For this purpose, a lens is made of a material with higher refractive index than the surrounding medium. Describing a lens in terms of geometrical optics [4, Chapter 1], this leads to a deflection of rays according to Snell's law. Additionally, the circularly symmetrical shape and curvature of the lens ensure that parallel incident rays will meet in the same point in the focal plane.

In terms of wave optics, a lens imposes a phase delay on the wavefront which varies with distance from its central axis and in this way transforms a plane wave into a converging spherical wave (or *vice versa* a diverging spherical wave into a plane wave). The sphericity of the wavefront means that all of its parts meet at a single point with the same phase and interfere constructively, which creates a focus. The offset of the focus from the lens's optical axis depends on the angle at which the plane wave arrives at the lens. In this way the lens separates plane waves coming from different directions by projecting them onto different points of the focal plane and thus forms an image. This is also known as the Fourier transform property of a lens, since it transforms a frequency representation (angle with respect to optical axis) into a spatial representation (lateral offset from optical axis).

A general imaging system can be regarded as mapping points of an object plane onto points in the image plane. If this mapping is flawless, i.e., each point of the object plane is mapped onto a distinct point of the image, all the details of the object are reproduced in the image. However, if this imaging process is perturbed in some way, the resulting image

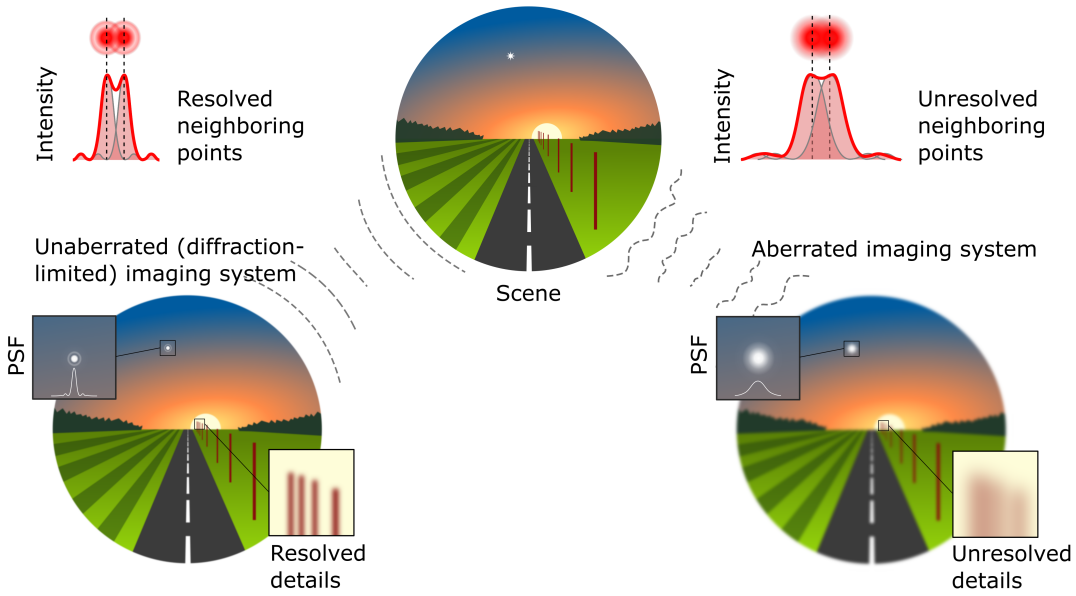

Figure 1.1: Schematic of image formation in an unaberrated (left) and aberrated (right) system. A wider PSF results in overlap of the images of neighboring points, making finer details indistinguishable.

deteriorates. If for example a plane wave coming from a distant point source is aberrated on its way so that some parts of it are delayed, the wavefront is not planar anymore. This wave will therefore no longer be transformed by the lens into a perfectly spherical wave and as a result some parts of the wavefront will arrive at the focus out of phase. This reduces the brightness of the focus due to destructive interference and also makes the focus broader and changes its shape. In this case, images of neighboring points start to overlap and may become indistinguishable, making finer details of the object unresolved in the image (Fig. 1.1). The loss of intensity additionally results in lower signal in the image. If the signal is too weak, it might get lost or significantly distorted by the measurement noise.

The shape and intensity of the focus are generally described by the so-called point spread function (PSF) – the imaging system's response to a plane wave. The PSF is an important characteristic of an imaging system affecting its resolution and signal-to-noise ratio. Since the PSF characterizes how a point source is imaged by the optical system, an image of a continuous object can be expressed as a convolution of the object function and the PSF [6, Chapter 9.5]. It has to be noted however, that this holds only for the case where the PSF is identical across the entire field of view of the imaging system. In practice,

because the waves arriving from slightly different directions take different paths through an aberrating volume, point objects may map to differing PSF images depending on their location in the field of view. This is referred to as **anisoplanatism** of the system, and the region of the image where the PSF remains unchanged is referred to as **isoplanatic patch** [7]. Additionally, one has to distinguish the image formation process for coherent and incoherent systems, and therefore whether interference contributes to image formation or not [8].

An ideal PSF, resulting in a perfect image, would be the Dirac delta function. In reality this is however not achievable due to effects related to the wave nature of light. Even under ideal imaging conditions, there is a limit to the achievable resolution as light cannot be focused tighter than the diffraction limit. The diffraction limit naturally emerges when calculating the free space transfer function for the angular spectrum of plane waves over distances substantially longer than the wavelength (far field): the magnitudes in the spectrum of spatial frequencies exceeding the inverse of the wavelength exponentially decay, not allowing details finer than the wavelength to propagate. This therefore imposes a minimal possible focus size that can be created by any system [4, Chapter 4.1].

Overcoming the diffraction limit (super-resolution) is possible [5, Chapter 6] by combining controlled illumination and computational reconstruction [9, 10]. As one example, structured illumination microscopy uses controlled laterally periodic illumination interacting with the sample's spatial frequencies and Fourier space reconstruction to increase the spatial bandwidth of the imaging system and therefore the resolution [11]. Another example for super-resolution imaging is near-field scanning optical microscopy: since the diffraction limit emerges for far field imaging, sub-wavelength resolution is possible in the near-field [12]. This technique is however limited to surfaces and therefore finds only limited applications in biology.

Independent of whether a standard or super-resolution far field imaging method is used, they all rely on the control of light at the diffraction limit. This motivates perfecting the optical components to compensate for deteriorating factors such as for example dispersion – the dependence of the refractive properties of light on the wavelength. Due to dispersion, a lens, as a refractive element, will focus different wavelengths at different focal planes. These so-called chromatic aberrations can be partially overcome by special lens design (achromats) [13].

However, even a perfectly manufactured imaging system will not reach its theoretical, diffraction-limited resolution when the operation conditions are sub-optimal. For example, in ground-based astronomy, atmospheric turbulence causes image distortions. Or in optical microscopy *in vivo* in the brain, samples often have a spatially as well as temporally varying refractive index. Since in both these cases image distortions are short-lived, they cannot be universally compensated solely by changing the design of the optical system. This motivates the search for solutions that allow an optical system to actively adapt to changes in imaging conditions at fast time scales.

1.1.3 Adaptive optics

In adaptive optics (AO) an element is added to the optical system that can be adjusted to adapt to changing imaging conditions and revert their deteriorating effects. In the case of atmospheric turbulences affecting ground based astronomical observations, moving layers of air of varying temperature and refractive index introduce random wavefront aberrations (random phase delays in different parts of the arriving wavefront). This results in what appears as twinkling of the stars to the naked eye, or a blurry image in the telescope.

The first adaptive optics systems to correct for such aberrations were conceptualized for ground based telescopes already in the 1950's [14], suggesting to correct apparent object displacements with a controlled tip-tilt mirror. In [15] John W. Hardy described the development of the first AO system for a satellite tracking telescope intended for military use. Throughout the 1970's the main research effort was directed towards two novel engineering problems. First, to create an adaptive element that would be fast and precise enough for atmospheric aberration correction, and second, to find a way to identify these aberrations, i.e., to design a wavefront sensor. The first problem was solved by constructing a deformable mirror as an adaptive element. This mirror was a thin continuous surface with segments which could be displaced with piezoelectric actuators in the range of about 10μm with submicrometer precision to achieve a desired profile. To address the second problem, a shear interferometer [16] was adapted for wavefront sensing with non-monochromatic light.

Since then, wavefront sensors and deformable mirrors, running in a closed loop of sensing and correcting aberrations (Fig. 1.2), have become a standard method in many earthbound telescopes [17]. In these telescopes, a deformable mirror adjusts its surface to restore the sphericity of a wavefront and therefore improves focusing. Changing the length

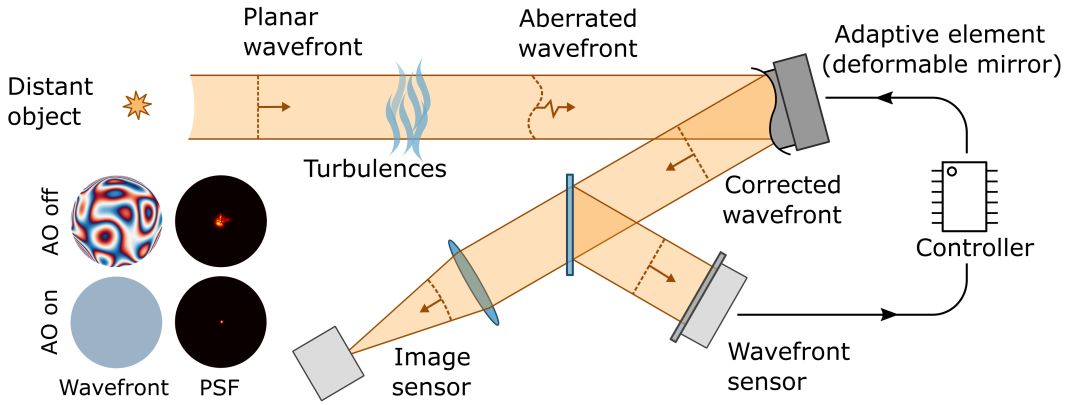

Figure 1.2: Conceptual schematic of adaptive optics for aberration correction as used in astronomy. A planar wavefront from a distant object gets distorted by atmospheric turbulences, and the distortion is compensated by an adaptive element (deformable mirror). The compensation is calculated based on the residual aberration measured with a wavefront sensor in a closed loop.

of the light path locally, depending on its position in the aperture, the mirror performs the role of a spatial light modulator (SLM), undoing the distortions to the wavefront caused by the atmospheric turbulences. This is achieved by applying a phase modulation to the SLM which is the inverse of the wavefront aberration, thus resulting in the correction of the PSF. Ideally, this would improve the image across the whole field of view. However, if the optical system has pronounced anisoplanatism, the improvement is observed only within the isoplanatic patch. The area of correction can be extended by using several SLMs optically conjugated to different planes within the aberrating volume (multi-conjugate AO) [18].

Spatial light modulation can not only be achieved with deformable mirrors. Depending on the modulated property of the light field, one can distinguish amplitude, phase, and polarization modulation. A variety of devices has been developed for modulating these different properties of light, each coming with its own engineering characteristics and limitations. By operating principle they can be split into two major groups: reflective and refractive SLMs.

Reflective devices control the shape of their reflective surface. Deformable or membrane mirrors (DM), with a continuous surface shaped with either piezoelectric or electrostatic actuators [19], and segmented mirrors, consisting of rigid segments independently actuated with several degrees of freedom [20], allow phase modulation by varying the

light path length. Digital micromirror devices (DMDs) consist of thousands of small mirrors arranged in a regular grid, each toggled between either of two possible states, providing binary amplitude modulation of the wavefront. Due to the small size and periodic arrangement of the micromirrors, they can also act as diffraction grating [21].

Refractive devices utilize the delay of the phase of light propagating through a medium of higher refractive index. They impose phase modulation by either varying the refractive index, as in liquid crystal-based devices [22], or by varying the thickness of the refractive elements, such as fluid-filled expandable cavities in optofluidic devices [23]. As opposed to reflective adaptive elements, these are better suited for monochromatic light because of dispersion. Additionally, liquid crystal-based devices require linear polarization of the incident light.

Although these devices can control only one parameter of the light field, either amplitude or phase, modulation of both parameters at the same time is possible by either appropriate alignment of the modulator with respect to the beam or by grouping adjacent modulating elements into so-called superpixels. For example, phase and amplitude control can be achieved with an amplitude-only binary DMD through off-axis angled placement adding a phase prefactor to each of the micromirrors [24]. *Vice versa*, amplitude can be controlled with a phase-only SLM by grouping adjacent elements into superpixels and adding phase differences between them to attenuate the resulting amplitude of the superpixel [25, 26]. Full control of polarization and complex amplitude is also possible, allowing to create even more complex structured light beams [27, 28].

Such fine and precise manipulation of light has found numerous applications beyond adaptive optics and imaging, for example in lithography [29], laser fabrication [30], 3D printing and additive manufacturing [31], optical tweezers [32], digital holography [33], or pulse shaping [34]. This list is by no means exhaustive, and novel applications are emerging as the technology advances and the modulation devices become less expensive and more widely used.

For imaging applications of adaptive optics, and in particular for optical microscopy, however the main problem remains to find the correction needed to compensate for aberrations, i.e., determining the distorted wavefront shape.

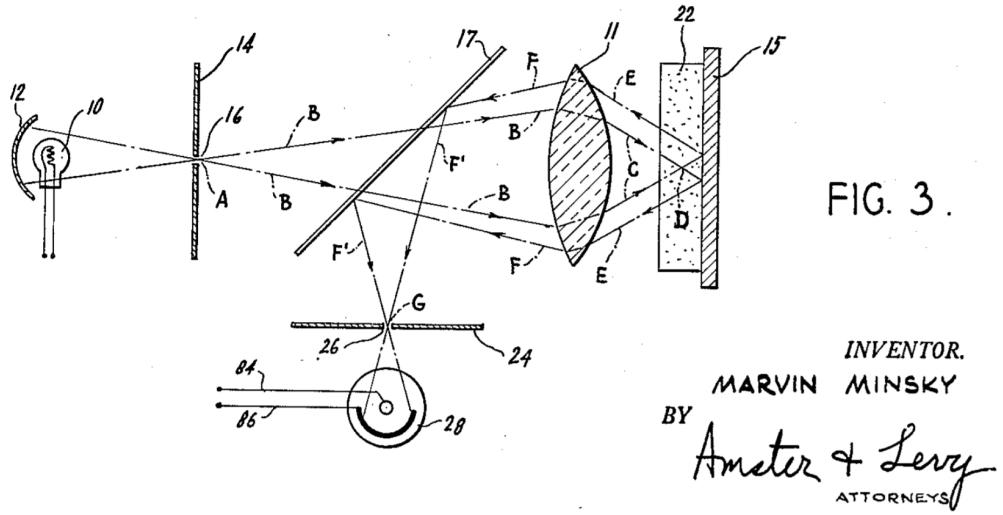

Figure 1.3: Schematic of the confocal microscope for reflected light detection presented in Marvin Minsky's patent in 1957. The illuminated pinhole serves as a light source which is focused onto the sample with an objective. The same objective collects the reflected light, which is then diverted to the photosensor for measuring light intensity at the focal spot. A pinhole, confocal to the illumination pinhole and the sample plane, rejects out of focus light and improves depth selectivity. Scanning of the sample is needed to acquire an image of the region of interest. Reproduced from [36].

1.1.4 Two-photon fluorescence laser scanning microscopy

In two of the experiments described in this thesis, a two-photon laser scanning microscope was used for fluorescence imaging. Laser scanning microscopy can be traced back to the confocal microscope invented by Marvin Minsky [35]. In confocal microscopy, a specimen is illuminated by a focused light beam that is scanned across the sample one point at a time. The light returning from the sample is imaged onto a pinhole placed in the plane optically conjugate to the focal plane in the sample (hence confocal). The image is finally obtained by scanning the focus across the region (or volume) of interest and measuring the confocal intensity in each position (pixel or voxel).

The pinhole blocks light originating from outside of the focal volume, such as reflections from the surface or tissue layers above and below the focal plane. The detected intensity only passes through the pinhole if it originates from the focal plane and is measured by a point detector (for example a photomultiplier). This configuration suppresses out-of-focus light and increases the axial resolution compared with a widefield microscope, which made confocal imaging an important tool for studying typically three-dimensional and densely labeled biological samples.

Typically, this microscope is used in an epidetection configuration, meaning that the same objective is used to deliver illumination and to collect light returning from the sample. The returning light is diverted to the detection path with a semitransparent mirror as shown in Fig. 1.3.

A similar configuration can be used with a laser as the light source [37]. This enables a wide range of imaging modalities, for example fluorescence imaging, often also using pulsed high-power lasers for exploiting nonlinear effects. Fluorescence imaging is the most widely used approach for microscopy with biological samples thanks to the many methods for chemical [38] and genetic [39] labelling. Such labels are used for example for structural imaging or visualizing gene expression, or in neuroscience for imaging changes in calcium concentration in neurons [40] – allowing to monitor the dynamics of neurons and biological neural networks.

Nonlinear effects are exploited in two- [41] or multi-photon [42] fluorescence excitation, which improve imaging in particular in scattering samples such as tissue. Because the near-simultaneous absorption of two or more photons is needed to induce fluorescence, its generation becomes proportional to the intensity exponentiated to the number of photons needed, i.e., square for the two-photon, cubic for three-photon, etc. This makes the fluorescence PSF smaller and improves the resolution compared to single-photon excitation at the same wavelength. Additionally, the longer wavelengths of light typically used for multi-photon excitation (in the near infrared range) are less susceptible to refraction and scattering. This allows imaging deeper into tissue, for example for *in vivo* imaging in the brain [43].

A major advantage of multi-photon-induced fluorescence is that excitation is confined axially to the focal plane only due to the properties of the excitation PSF. Therefore, no pinhole is needed in the detection path and fluorescence can be detected with a collecting lens in front of the photomultiplier tube. This allows collecting scattered fluorescence light that would otherwise be rejected by the pinhole and increases the signal-to-noise ratio in particular in aberrating samples such as brain tissue.

The setup for two-photon imaging experiments described in this thesis is shown schematically in Fig. 1.4 and in full detail in Fig. 2.7. An expanded laser beam with wavelength $\lambda = 920$ nm is focused with a water immersion objective in the sample and scanned across the region of interest using linear and resonant galvanometer scanning

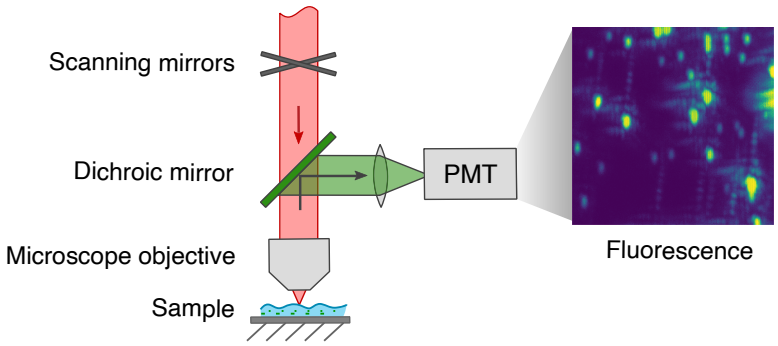

Figure 1.4: Conceptual schematic of a two-photon laser scanning microscope. An expanded laser beam is focused with an objective and scanned across the sample with two mirrors, while induced fluorescence is collected with the same objective, separated from the excitation path with a dichroic mirror, and measured with a photomultiplier (PMT). The image is reconstructed by associating the PMT signal with the position of the scanned focus. A detailed schematic of the setup used in our experiments is reproduced in Fig. 2.7.

mirrors. The focused light excites fluorescence in a labelled sample through a two-photon process, resulting in the emission of fluorescence at about half the excitation wavelength. Excitation at 920 nm as typically used in our experiments thus results in fluorescence in the blue to green range (detected around 500 nm). The induced fluorescence from the focal volume is collected with the same objective, separated with a dichroic mirror and detected by a photomultiplier tube (PMT). We refer to the corresponding optical paths through the microscope as excitation and detection paths, respectively. Two- or three-dimensional images of fluorescence intensity are then computationally reconstructed from the PMT signal by associating the position of the focus (determined by the position of the scanning mirrors and additionally the axial position of the objective for three dimensional images) during scanning and the fluorescence intensity measured at each corresponding location. For image reconstruction the continuous mirror positions are binned into pixels; this processing as well as hardware control are done with ScanImage software [44].

A liquid crystal phase-SLM is placed in the optical path to enable beam shaping for adaptive optics. Since a close to monochromatic laser source is used, a refractive adaptive element with high refresh rate and resolution can be used.

1.1.5 Wavefront sensing

Aberration is the result of light passing through a medium with locally varying refractive index. As discussed in the previous sections, the variation in refractive index leads to irregular phase delays in different regions of the wavefront and consecutively to the deviation of light from the expected path for which the imaging system was designed. This alters the point spread function of the system and as a result worsens the image quality. In order to correct for such irregularities in the wavefront with AO, the aberrations first need to be measured.

At the time of the creation of the first AO telescopes, the effect of atmospheric aberrations was quantitatively studied and it was found that most variations of the wavefront can be accurately approximated as a sum of a few basic surface shapes (defocus, astigmatism, coma, etc.) [45]. They can be conveniently represented by polynomials that are defined over the aperture, for example Zernike modes [46, 47].

In the work discussed in this thesis we frequently use Zernike polynomials to represent wavefront shapes. Zernike modes are an orthonormal basis of polynomials defined on a unit disk, which is convenient for many applications in optics, where radially symmetrical beams and elements are very common. These polynomials generate balanced aberration surfaces, i.e., minimize the surface variance for any combination of modes, and are well studied in applications that require the parametrization of aberrations [48, 49].

Zernike polynomials are functions of two variables. In polar coordinates, each polynomial can be generated by specifying two indices – the radial and azimuthal spatial frequencies. Using Noll's indexing scheme [50] they can be sequentially ordered. This allows representing an arbitrary surface as a linear combination of Zernike modes conveniently parametrized as a vector of corresponding coefficients. The larger the number of modes that are included in the expansion, the finer are the details of the surface that can be represented.

Methods for measuring aberrations in optical system can be divided in two main categories:

Sensor-based approaches aim to directly measure the shape of the wavefront. This raises two practical problems: first, an isolated PSF of the system has to be measured, and second, this measurement has to be phase sensitive. The first issue can be addressed by imaging an isolated point source producing a well-defined wavefront. The problem

of measuring phase can be solved by using a wavefront sensing device that converts phase variations into intensity variations, for example a Shack-Hartmann wavefront sensor (SHWS) [51] or an interferometer [15]. This overall approach is commonly used in astronomy where a distant star can serve as a point source, a so-called guidestar. To avoid having to rely on the presence of a suitable star in the area of observation, artificial guidestars can be created, for example through laser-excited resonance fluorescence in the sodium layer of the atmosphere [52].

Direct wavefront sensing has the advantage that it yields a wavefront measurement in a single shot. It has become the standard approach in astronomy, allowing for fast correction control loops. Direct wavefront sensing is however not as conveniently implemented in microscopy, because it requires imaging of an isolated point source which naturally are typically not present in biological samples. Therefore, similar to artificial guidestars in astronomy, point sources have to be introduced into the sample (labelling).

The **sensorless** approach does not require direct measurements of the wavefront. Instead, the aberrations are probed by displaying different corrections on the spatial light modulator while assessing whether the image quality is improved or not. This can be seen as an optimization process with some image quality metric as the target function, and correction modulation as the optimization variable. This method is very widely applicable, and can be formalized into a general framework [53]. The disadvantage of this method is that multiple measurements need to be taken before an optimum (possibly also only a local optimum) is reached, which is limiting for real-time corrections. Additionally, in microscopy repeated exposure of the specimen is preferably avoided due to photobleaching and phototoxicity.

A challenge that is specific to wavefront sensing in microscopy arises in confocal imaging with reflected light. Different from fluorescence imaging, this does not require labeling the sample and this method is therefore broadly applicable. In confocal scanning microscopy the illumination is focused inside the sample. Therefore, light reflected from the focal plane and returning into the detection path could potentially be used for wavefront sensing independent of labelling, similar to a guidestar. However, because the light source for illumination and the detectors are located on the same side of the aberrating medium (epidetection configuration), the wavefront can only be measured after light has passed through the aberration twice, as illustrated in Fig. 1.5. In this roundtrip, some components

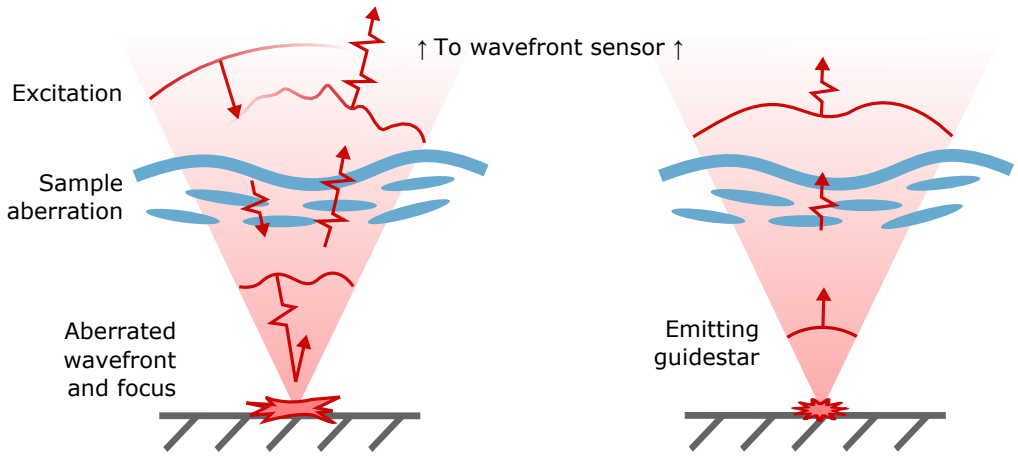

Figure 1.5: Schematic of wavefront sensing in a microscope with reflected excitation light as well as with a guidestar. When reflected excitation light is used for wavefront sensing, it can be measured after passing through the sample aberration twice, and one therefore has to disentangle the contribution of the excitation pass to correct the focus inside the sample (left). If a point source (guidestar) is emitting light from within the sample, direct wavefront sensing is possible since the wavefront only carries the single pass aberration (right).

of the aberration can be cancelled out or get amplified, depending on the aberration symmetry and the reflectivity of the specimen. Disentangling the aberrations occurring on this forward- and return pass, commonly referred to as the dual-pass problem, is however necessary for microscopy in an epidetection configuration if a reflected focus should be used as a guide star.

Generally, depending on the type of the microscope, different aberrations contribute to the image formation process and therefore need to be corrected. In confocal reflection or confocal fluorescence microscopy one needs to correct both excitation and detection aberrations; in multi-photon microscopy one needs to correct excitation aberrations, or in wide field microscopy only detection aberrations [54].

In the following section we review the wavefront sensing approaches that are commonly used in laser scanning microscopy.

1.2 Related work – adaptive optics in microscopy

Sensorless AO

The first AO system for a multi-photon microscope [55] was implemented with a deformable mirror with 37 electrostatic actuators. The shape of the mirror was optimized with a genetic algorithm with the aim of maximizing fluorescence intensity [56], which correlates with the quality of the focus. Running 10 generations with a population size of 100 took about 3 minutes (with the updating speed of the deformable mirror at the time being the bottleneck preventing faster performance). Optimization of fluorescence intensity using hill-climbing and optionally other image metrics was demonstrated in [57]; [58] discusses optimization strategies based on genetic algorithms or hill-climbing, as well as image-based metrics. An example of an image metric other than brightness is the magnitude of the low spatial frequency band of an image [59].

When an optimizer is agnostic of the function it minimizes, treating it as a black box, the process of optimization can be rather inefficient. It will therefore require many iterations of sample probing to find the direction of improvement and to converge, especially in a multidimensional search space. One can improve the situation by incorporating some prior knowledge into the algorithm, either about the sought aberration or about the physical process generating the optimized signal. This approach is also referred to as **model-based** optimization.

For example, if all degrees of freedom of the SLM are treated as independent parameters (as in the references mentioned above), a rather large number of measurements is needed for the optimization process to converge. However, as experiments on commonly used, weakly aberrating specimens have shown [60], often aberrations can be represented using a small number of low-order Zernike modes. This motivates the use of an aberration model to reduce the solution search space and to mitigate oversampling. This idea was implemented in the first demonstration of an adaptive confocal fluorescence microscope [61], where 7 low-order Zernike modes (astigmatism, coma, trefoil and spherical aberration) were corrected with a deformable mirror. The modes were detected independently with indirect modal sensing: each mode was applied to the mirror with alternating positive and negative magnitude, and the corresponding fluorescence intensity was measured as the average photon count in all image pixels. The difference in intensity between the negative- and positive-biased measurements for each mode indicated the magnitude of its contribution to

the sample aberration. The deformable mirror had the same number of degrees of freedom (37) as in [55], but significantly fewer measurements were needed due to the representation and sensing of aberrations using Zernike modes.

A different example of model-based representation of aberrations was shown in [62], where an aberration across the pupil was tiled in several segments, and phase tip and tilt were determined for each of them independently. Images of the sample were taken with illumination coming from one segment of the pupil at a time and phase ramps caused these images to be proportionally displaced in the corresponding direction. By comparing the lateral displacements of the resulting images, local phase ramp magnitudes and orientations were determined and finally combined into a whole pupil aberration phase function.

The concept of using a physical model to introduce *a priori* knowledge of the problem is shown in [63]. The pupil aberration was represented as a Zernike mode expansion, and the corresponding PSF intensity was analytically calculated as a function of each mode's presence. This model was then used as a heuristic for an optimization algorithm and to develop a solution space sampling strategy, requiring $2N+1$ measurements for an expansion of aberrations with N modes. In [59] similarly an analytical model was established but for a different metric – spectral density of low spatial frequencies in the image as a function of aberrations, allowing to obtain a correction through optimization based on the fluorescence image. This strategy was applied for two-photon microscopy in [64] and allowed detecting 11 Zernike modes of an aberration with 23 probing measurements.

Sensor-based AO

Wavefront sensing requires a point source in the sample at the location where the correction should be applied. Therefore, wavefront sensing methods in microscopy need to solve the problem of introducing a point source inside the sample. Such a point source avoids the dual-pass problem described above (Fig. 1.5), and allows direct wavefront sensing.

Sample labelling is often the technically easiest way to introduce a point source: in [65] direct wavefront sensing was demonstrated by injecting fluorescent beads into the sample. The beads acted as point emitters under the excitation light and allowed to directly measure the aberration with a Shack-Hartmann wavefront sensor. This was practically applied in a wide field [66] and a confocal fluorescence microscope [67]. In the incoherent fluorescence process the phase aberration of the excitation beam is lost, so that emitted

light coming from a point source carries only a single pass aberration. A similar approach can be applied with two-photon excitation and was demonstrated in [68]. Alternatively to injecting beads, expressing fluorescent proteins allows genetic labelling in a less invasive way and in targeted neural structures. In this situation, the fluorescence of cell bodies or dendrites can be used for generating guidestars with laser illumination for wavefront correction [69].

In addition, whereas point detectors with large areas (such as PMTs) are not very sensitive to scattering, imaging with a camera, as required for a wavefront sensor, can become problematic due to noise and scattering for the dim signals often observed in fluorescently labeled biological samples. Such problems motivate the use of reflected excitation light as an alternative for measuring corrections, since these signals are not limited by the fluorescence photon budget.

However, to overcome the problem of the accumulation of excitation and detection path aberrations, one needs to detect light coming only from the focal area. This has been demonstrated with coherence gating in [70], where an interferometer was combined with confocal reflectance imaging. By adjusting the length of the reference arm of the interferometer, one can selectively detect light reflected from the focal volume, discarding reflections from deeper or shallower layers. Therefore, only light coming from a confined volume at the focal plane is modulated by the interferometer, thus resulting in a scattering point source as required for direct wavefront sensing. This was practically demonstrated in [71]: the phase of the returning light was measured in several steps using different path lengths in the interferometer and aberrations were determined by simulating a Shack-Hartmann wavefront sensor [72]. Due to the technical challenges associated with interferometric detection of scattered light, this approach has not become widely used in microscopy.

Alternatively, a simpler setup for scattered light wavefront sensing with a SHWS, only using a confocal pinhole to remove out-of-focus light while still preserving sufficient wavefront information, was tested in [73]. However, this approach cannot separate forward- and return-pass aberrations and additionally was highly dependent on the sample structure and reflectivity.

Machine learning

Artificial neural networks as supervised machine learning algorithms date back to the idea of a biologically inspired artificial neuron, the so-called perceptron, suggested by Frank Rosenblatt in the 1950's [74]. This computational unit takes a weighted sum of its inputs and thresholds the result, and in this way is able to solve some binary classification problems after correctly setting the weights in a learning procedure. Marvin Minsky and Seymour Papert extensively explored its abilities and limitations in [75], but the lack of efficient training procedures for potentially more powerful multilayered models was limiting at the time.

It was shown later that such a feed-forward network with a single hidden layer and nonlinear activations can serve as a universal function approximator given enough hidden units [76, 77]. Additionally, Rumelhart and Hinton proposed a training procedure for multilayer networks through backpropagation [78], which has become the standard approach for training neural networks. For training, the network output is calculated for a given input. Then, the error between the output and the target is calculated (loss), and the weights of the network are updated along the gradient of the error. Combined with using randomly chosen parts of the training dataset (mini-batches) for each of these iterations, this method is known as stochastic gradient descent. Stochastic gradient descent allows to optimize multilayer artificial neural networks, commonly referred to as deep learning.

The power of deep learning approaches was demonstrated in 2012 by the Hinton group with AlexNet [79] which obtained the best score in the ImageNet Large Scale Visual Recognition Challenge, with an image classification error rate almost twice as low as that of the nearest competitor. This performance was achieved through a combination of several state-of-the art ideas. First, convolutional layers introduced by LeCun [80] replaced computationally costly and parameter-rich fully connected layers with sparsely and only locally connected ones with much fewer parameters. Second, max pooling [81] was used, reducing the number of parameters passed to consecutive layers by selecting the highest-magnitude features. Additionally, AlexNet also used several novel features: ReLU activation functions [82] and dropout regularization [83] to prevent overfitting, alongside with dataset augmentation. Further, using a graphical processing unit (GPU) allowed training a larger model in feasible time. Indeed, the architecture of GPUs turned out to be very well suited for computations with neural networks, which inherently require

many parallel operations [84]. Together, these design decisions have become the defining features of deep learning and contributed to rapidly improving its performance in computer vision, as well as finding applications in other domains.

Modern deep learning frameworks like Tensorflow [85] or PyTorch [86] efficiently implement the algorithms listed above. Working within these frameworks formalizes the problem of specifying the neural network model, providing the training dataset, defining the loss function, and tuning the training hyperparameters.

Deep-learning-based AO

In the work presented in this thesis we use machine learning methods for image-based wavefront sensing. This can be viewed as a regression problem of finding parameters of an aberration model and can be solved for example by (deep) feed-forward neural networks and in particular deep convolutional neural networks (CNNs).

The idea of applying neural networks to wavefront sensing was first introduced in astronomy in the early 1990's, before the modern deep learning architectures were invented. In [87] a perceptron-like model with a single hidden layer with sigmoid activation and linear output was trained on simulated star images to detect and correct atmospheric aberrations for the Multiple Mirror Telescope [88]. Two 13×13 images of the star, from in- and out-of-focus planes served as the input, and the output were tip, tilt and piston modes for each of the six mirrors of the telescope. A convenient feature of this approach is that the network can be trained to directly output adaptive element control signals, omitting intermediate calculations. Further, no additional wavefront sensor is needed and the aberrations are measured in a single shot, only based on the images, which combines the main advantages of sensorless and sensor-based approaches. Another characteristic feature of this approach is that the neural network extracts phase information using two separate image planes; two combined images implicitly carry phase information (phase diversity [89]) which cannot be retrieved from a single image.

More recent works use deep network architectures and handle much higher resolution images. For example [90] used the Inception architecture [91] and 512×512 PSF images to recognize phase, however only for very low-order aberrations. Up to 65 Zernike modes of aberrations were recognized by a convolutional neural network in [92], trained on simulated images of a guidestar under various aberrations.

Deep learning can also be used to enhance sensor-based approaches for recognizing

finer details of aberrations. A Shack-Hartmann wavefront sensor is an array of small lenses (lenslets) placed in front of the camera sensor, each producing its own focus depending on the local shape of the wavefront arriving. Typically, a SHWS is used to determine the slope of the phase for each lenslet by the offset of its focus, and to reconstruct the full wavefront by combining the measurements of all the lenslets. However, a trained deep neural network can pick up finer details of phase variations, serving as a model for a process for which we do not have an explicit inverse function. In [93] up to 120 Zernike modes could be recognized with a trained network from a single SHWS image. This learned mapping can be quite complex: for example, instead of a lenslet array, a random medium can be used to provide phase diversity, and a network can be trained to detect aberrations in this situation [94]. We present the first application of deep learning wavefront sensing for a two-photon microscope in a sensorless configuration in Chapter 2.

However, a limitation of deep-learning wavefront sensing is that the operating range of the model is limited by the data that were presented to the neural network during training. This results in unreliable predictions for inputs beyond the data range covered by the training dataset. Additionally, the resulting wrong predictions cannot easily be detected, other than by failure of the wavefront correction process.

Differentiable modelling

Sensorless model-based methods as mentioned above typically utilize an analytical model to calculate the PSF as a function of aberrations and consecutively the resulting image brightness or another metric. These analytical models could be reliably established for modal expansion of small aberrations, and used as heuristic in an optimization process of finding the sample aberration through several probing measurements.

However a model of an optical system, provided that it is detailed enough, can also be used in a different way: if image formation can be described mathematically, a phase aberration can be represented as an unknown model parameter, which can be found by matching the model's output to the observed output of the actual system. In this situation, phase reconstruction is for example not limited to whether an experimentally encountered aberration is similar to the training dataset, but rather by the accuracy of the model. Another advantage of this model-based approach is that, unlike in sensorless approaches, it does not require iterative sample probing, but only relies on some initial measurements recorded at the beginning of the experiment.

This idea can be traced back to the Gerschberg-Saxton phase retrieval algorithm which discovers the phase of a wavefront from two light intensity measurements made in different planes with known complex amplitude transfer function between them, for example image and Fourier planes. By iteratively computing complex amplitude transformation between these two planes, while constraining the resulting magnitudes to the measurements and keeping the calculated phase, the unknown phase is found when the discrepancy between measured and computed amplitudes converges to a minimum [95].

In [96] James Fineup modelled more complicated optical systems with multiple elements and optimized for an unknown phase factor using the gradients of the model with respect to unknown parameters. These gradients could be computed for either Zernike mode expansions or for discretized aperture phase representations. A major part of this process could be automated with algorithmic differentiation [97]. In [98] this is described as a general approach: first, a model of the optical system, including the unknown parameters, is written down symbolically. Then, an error metric measuring the mismatch between the model and observations is introduced. Finally, gradients of the error with respect to parameters of interest are calculated automatically, and the error is minimized using gradient-based optimization.

This approach very closely resembles differentiable rendering or inverse graphics [99]. Differentiable rendering can be used to infer parameters of a three dimensional scene (such as geometry, lighting, or texture) from rendered images [100, 101, 102]. This is achieved by implementing an end-to-end differentiable rendering equation and by optimizing its parameters with gradient-based methods. Since this relies on the same algorithmic base as deep learning – automatic differentiation and gradient-based optimization – it can be integrated with deep learning frameworks [103].

This integration can be useful in multiple ways. For example, recovering parameters of a three-dimensional scene with optimization is an ill-posed problem prone to converging to local minima. Therefore, using a generator network can provide better solutions [104, 105] similar to a deep image prior [106]. In this case, the unknown parameters are not optimized directly, but are generated by a suitable network which has a regularizing effect on the solution [107]. As a second example, machine learning models that require spatial reasoning, for example estimating geometry or pose, can be trained without requiring labeled three-dimensional data, but in a self-supervised way with two-dimensional images

only [108, 109], and the *a priori* known information can be introduced into the training on the rendering stage [110].

Differentiable physics [111, 112, 113] generalizes this model-based optimization idea to simulations of any dynamical physical process. Keeping track of the calculations through multiple time steps simulating the evolution of the system, the gradients of the end state with respect to the parameters of interest are propagated, for example to search for initial conditions [114, 115, 116]. This can be similarly integrated with machine learning in relevant domains, for example in robotics [117, 118].

Differentiable simulation of optical systems has been demonstrated in several applications. In ptychography, objects are not imaged directly, but reconstructed computationally from coherent interference patterns of scattered light and therefore phase information is crucial for the reconstruction. In [119] differentiable modelling is used to extract phase information from intensity measurements by directly optimizing the unknown parameters to match the model to the observations.

Another example uses a differentiable model together with a deep prior for diffraction tomography [120]. A three-dimensional refractive index distribution of a thick sample is reconstructed from multiple images taken with alternating illumination angles. In this application, a deep prior was used to parametrize the sample volume, and the imaging model incorporated in the loss function generated the images that were compared to the measurements. Similarly, phase imaging can be done with a generative network and an image formation model [121, 122].

Apart from image reconstruction, differentiable simulation can be used to optimize an imaging system's design for better performance. For example in [123], an illumination scheme is optimized to reduce the required number of measurements and to improve the resolution in a Fourier ptychographic microscope for various imaging modes.

1.3 Contributions

In the following sections we discuss the individual technical contributions of the peer-reviewed publications included in this cumulative thesis. The common theme of the contributions is the development of wavefront sensing methods based on machine learning for microscopy in an epidetection configuration as typically used in biology.

1.3.1 Adaptive optics with reflected light and deep neural networks

The main challenge for wavefront sensing in a two-photon laser scanning microscope lies in obtaining reliable signals that carry information about the wavefront aberrations. Biological specimens typically do not contain natural guidestars, i.e., fluorescent point sources. Guidestars therefore need to be introduced, which might be invasive or impractical. However, even in labelled samples the signal is often very weak due to the limited photon budget of small fluorescent structures, such as fluorescent beads with dimensions below the diffraction limit.

Alternatively, when using reflected excitation light imaged in epidetection, the problem of disentangling excitation- and detection path aberrations, as well as suppressing out-of-focus reflections, arises. We solve it by spatial filtering of the returning light through a pinhole similar to [73], and use deep learning-based wavefront sensing on the resulting confocal PSF intensity images, similar to astronomy [90, 92]. We used a convolutional neural network trained on labelled datasets with known excitation and detection path aberrations, training the network to recognize them independently.

To create such a dataset, a phase SLM was used to independently modulate excitation and detection paths of a confocal microscope integrated with the two-photon microscope, and a mirror was used as a fully reflective sample. Confocal volumes were imaged with 3 cameras placed at different focal planes to provide phase diversity. With this setup, 3 datasets were collected: one with entirely independent excitation and detection aberrations, one with closely linked aberrations in both paths, thus imposing the assumption that the aberrations should be similar, and one with only detection path aberrations to simulate the situation of imaging reflective guidestars. Zernike modes were used to generate phase aberrations, resulting in a representation of aberrations as a vector of mode coefficients, which was convenient for neural network output.

Deep convolutional neural networks trained on these datasets were tested in the corresponding imaging scenarios. We could achieve corrections based on reflected excitation light with excitation and detection path aberrations being disentangled by the network. Additionally, guidestar-based corrections were achieved with reflective particles injected into the sample.

1.3.2 Differentiable model-based adaptive optics with transmitted and reflected light

As shown in the previous section, a deep learning approach allows to approximate the inverse model of image formation given an aberration. Training such a model requires a large labelled dataset, and the predictions of the model are bound by this (finite) dataset. In this way, using Zernike modes as an aberration model restricts recognizable distortions in spatial frequency and in amplitude to the maximal mode order and amplitude represented in the dataset. Additionally, the distribution and combination of modes is typically not known, and will vary depending on sample characteristics. This adds to the difficulty of designing accurate datasets representing sample aberrations. Further, phase variations within an aberration of an actual sample are not bounded and can exceed the range over which the model is valid.

In contrast, optimization-based methods are not limited to a prediction range, but use a trial-and-error approach which is based on probing the sample to find a correction. Model-based methods improve the situation by utilizing prior information about the system and thus perform more efficiently.

In this publication we combined model based adaptive optics [124, 63] with gradient-based optimization. Similar to the deep learning approach, we showed that not only a single aberration can be corrected, but also combined excitation and detection aberrations as encountered in an epidetection setup. For this, we built an experimental setup that repeats the geometry of reflection imaging: a collimated beam is reflected off a phase SLM and focused through an aberrating sample onto a mirror. After reflection and a second (return) pass through the aberration, the beam is imaged with a lens onto a camera. An additional camera was placed in the focal plane behind the aberration to monitor the focus inside the sample. For this proof-of-principle experiment we used lenses with a numerical aperture of 0.04. Using Fourier optics and the angular spectrum method, we built a mathematical model for this setup. The input to the system was described as a complex amplitude over a 512×512 discrete grid in the SLM plane that encoded the phase-modulated input beam. Lenses and aberrations were modelled as phase factors of the complex amplitude at the corresponding planes, and the angular spectrum method was again used to calculate beam propagation between intermittent planes as well as to the camera. This resulted in an analytic expression that could be used to calculate a 512×512 pixel camera image output, given the phase modulation and aberration profile as an input. Additionally, the model was

differentiable.

This model was used to infer aberrations in the following way: a sample was placed in the setup and probed with several random phase modulations displayed on the SLM and corresponding images of transmitted (or reflected) light were recorded. Then, the computational model was initialized and optimized by adjusting aberration parameters to match its output to the actually measured camera images based on the provided probing modulations. This optimization process is similar to training a neural network, where free parameters (weights) are adjusted to match the network output to the target measurements. The mismatch between predictions and data was measured by the loss function defined as negative Pearson's correlation coefficient between the images.

We used Tensorflow to implement and optimize the model, since, like any modern machine learning framework, it has all the necessary components: automatic differentiation of expressions and gradient-based optimizers, as well as the ability to easily deploy the calculations on a GPU for better performance. We tested this approach in a single-pass (transmission) configuration as well as a dual-pass (reflection) configuration. We demonstrated that the technique is able to discover and correct transmission aberrations based only on backreflected light, and is thus compatible with an epidetection configuration.

The model optimization is happening "offline" i.e., only based on the initial measurements. Prediction results are not constrained to any particular aberration model and can therefore include high spatial frequencies corresponding to high-order Zernike modes.

1.3.3 Differentiable model-based adaptive optics for two-photon microscopy

In this chapter we applied the differentiable model-based approach outlined above to two-photon microscopy. For this, we modelled fluorescence image formation, taking into account the parameters of the objective and microscope magnification. Further, the two-photon excitation process was included, where fluorescence intensity depends on the square of the excitation light intensity or PSF. Similar to the experiment described above, the resulting differentiable model was then used to infer an aberration based on probing modulations. These modulations were displayed on the SLM and corresponding images of the PSF (generated by imaging fluorescent beads) were recorded. The recorded images were finally compared to images generated with the model using a loss function.

For this, fluorescence images first needed to be preprocessed since the signal had very low intensity. This was especially the case when aberrations were present, which often

yielded noisy images resulting from the low signal levels of only a few photons per pixel combined with shot noise and detection noise. Therefore, spatial low-pass filtering was applied to suppress high frequency noise. The loss function for minimization had two components: the negative correlation coefficient between the target PSF and the model PSF, and the pixelwise sum of the intensities of the prediction. The latter term was introduced, since the correlation coefficient is magnitude-insensitive, and therefore the optimization can find a solution with high correlation, but low intensity (for example by dimming some parts of the PSF through destructive interference or by diverting the light out of the field of view). By including the total intensity in the loss function, solutions were promoted that formed a PSF similar to the target while utilizing all of the light.

This first demonstration of combining differentiable optimization with scanning fluorescence microscopy allowed us to correct aberrations through layers of aberrating materials, such as vacuum grease, using fluorescent guide stars imaged using two-photon excitation.

1.4 Thesis outline

In summary, the main problem for adaptive optics in optical microscopy lies in finding a suitable correction through wavefront sensing to improve the image. A main difficulty in biological imaging results from the epidetection configuration of the microscope where the source of illumination and the detector can only be placed on the same side of the aberration. This configuration requires specialized solutions for direct wavefront sensing without sample labelling. The existing approaches, as reviewed in Section 1.2, show a trade-off between several complicating characteristics: increasing setup complexity for coherence gating, the need to introduce labels into the sample for sensor-based AO, or the requirement of multiple measurements (sensorless AO) and the corresponding slow correction refresh rate in dynamic samples.

At the same time, this also suggests guidelines for improving wavefront sensing in microscopy. First, improved methods should ideally be compatible with laser scanning microscopy with minimal setup modifications. Second, methods that don't require sample labelling would be most broadly applicable. And third, to reduce phototoxicity and increase imaging speed, rely on only a small number of measurements.

In this thesis, we show that machine learning methods can successfully address some of the problems outlined above. In particular, we show for the first time that neural networks are useful for wavefront sensing in two-photon imaging and can recognize aberrations

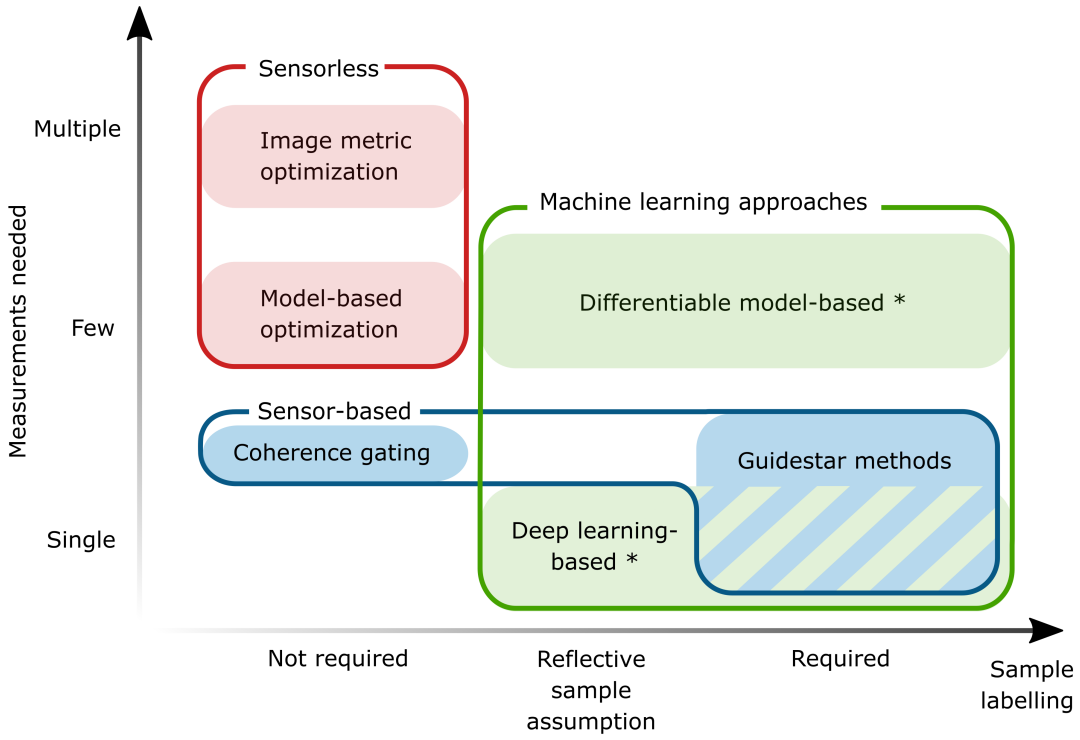

Figure 1.6: Comparison of the existing wavefront sensing methods and those developed in this thesis for adaptive optics in microscopy according to their main characteristics: number of measurements needed and requirement of sample labelling. Methods contributed in this thesis are marked with (*).

based on single PSF measurement. This is shown in Chapter 2 where we use deep learning to identify aberration corrections based on confocal images of the excitation light. Further, we propose and demonstrate a solution for combined excitation and detection aberrations using deep neural networks. A comparison of the existing methods and those developed in this thesis is shown in Fig. 1.6.

In Chapters 3 and 4, we show for the first time that using differentiable model optimization, wavefront aberrations can be inferred, based only on a small number of initial measurements, by taking advantage of prior information about the imaging system embedded in a model. A differentiable model is used for identifying aberrations in the excitation and detection path in a proof-of-principle experiment in Chapter 3. In Chapter 4 we develop a differentiable model of fluorescence image formation in a two-photon microscope and use it to correct aberrations.

1.5 List of publications

The following publications comprise the core contributions of this thesis and are presented as Chapters 2, 3 and 4 respectively:

- Ivan Vishniakou and Johannes D Seelig. Wavefront correction for adaptive optics with reflected light and deep neural networks. *Optics express*, 28(10):15459–15471, 2020, https://doi.org/10.1364/OE.392794
- Ivan Vishniakou and Johannes D Seelig. Differentiable model-based adaptive optics with transmitted and reflected light. *Optics Express*, 28(18):26436–26446, 2020, https://doi.org/10.1364/OE.403487
- Ivan Vishniakou and Johannes D Seelig. Differentiable model-based adaptive optics for two-photon microscopy. *Optics Express*, 29(14):21418–21427, 2021, https://doi.org/10.1364/OE.424344

CHAPTER 2

Adaptive optics with reflected light and deep neural networks

This chapter was published as a peer-reviewed paper in the *Optics Express* journal by the *Optical Society of America* in 2020 [125].
The authors are Ivan Vishniakou and Johannes D. Seelig.
https://doi.org/10.1364/OE.392794

2.1 Introduction

Diffraction limited imaging in many samples, for example in biological tissue, is limited due to aberrations and scattering. In this situation, combining laser scanning microscopy with adaptive optics can improve image resolution by correcting for aberrations using wavefront shaping [128, 129, 130, 131]. Using reflected light for wavefront shaping has the advantage that it relies on intrinsic sample contrast [132] and is therefore independent of sample labeling [70, 71, 128]. Additionally, even for fluorescently labeled samples, particularly for dim or sparsely labeled samples, the scattered light signal can be larger than the fluorescent signal [70, 71, 54].

Imaging with reflected light comes however with the difficulty that excitation and detection aberrations are not easily separated [54, 133, 134, 135]. In reflection-mode imaging, the signal depends on the excitation point spread function (PSF), which undergoes aberrations, the scattering object, and the detection PSF, which can undergo different aberrations [133, 134, 136].

For making an accurate correction of the excitation focus under these conditions, therefore contributions to aberrations accumulated in the excitation and reflected detection

pathway through the sample need to be disentangled. For strongly scattering samples, separation of illumination and detection pathways has been achieved using matrix methods [136, 133, 134, 135], which however require a large number of phase sensitive measurements to obtain a correction. For weakly scattering samples, one option to separate excitation and detection aberrations is to use a wavefront sensor that only detects light that is reflected from a tightly constrained focal volume. This can be achieved using coherence gating with high-bandwidth light sources combined with interferometric detection [70, 71]. A technically less demanding approach was implemented using confocal imaging with a pinhole sufficiently large to retain wavefront information [73]. In this situation, however, due to the extended confocal volume, aberrations measured with a wavefront sensor depended on a combination of sample and detection characteristics [73, 54, 131].

More recently, approaches for wavefront sensing based on deep neural networks have been developed [87, 137, 90, 138, 92, 139, 140, 141, 94, 93, 142]. These neural network methods directly compare measured light distributions to computationally generated ones. These approaches work so far only for a configuration that requires the correction of a single pass through a scattering medium, such as the atmosphere in astronomy and therefore cannot be applied for reflected light detection. In the epi-detection configuration commonly used in biological imaging, aberrations in the excitation and detection pathways need to be considered.

Here, we extend the deep learning approach for transmission wavefront sensing to reflection-mode imaging in an epi-detection configuration. Reflected foci for different aberrating samples are generated by independently modulating the excitation as well as detection path of the microscope using a spatial light modulator. With this setup, imaging for example a reflecting planar object through an aberrating layer can be modeled by modulating both the excitation, as well as the detection pathway while at the same time recording the light reflected off a mirror at the sample plane. Imaging a guide star through an aberrating layer can be modeled by only modulating the detection pathway while forming a focus on the mirror with the unmodulated excitation pathway.

Datasets generated in this way are used to train deep neural networks. We show that after training, these neural network models can disentangle excitation and detection aberrations of scattering samples. We verify the resulting excitation corrections using two-photon imaging.

2.2 Results

The experimental approach is shown schematically in Fig. 2.1. A two-photon microscope is combined with a spatial light modulator (SLM) and reflected light detection for wavefront sensing and correction. The reflected focal spot is monitored at three different focal planes using cameras (see for example [87, 143, 140]). Different from other reflection-mode adaptive optics approaches [61, 70, 71, 73] we separate excitation and detection such that both pathways can be modulated independently.

This is motivated by the fact that excitation and detection aberrations can differ. Generally, the incoming beam undergoes aberrations which alters the PSF at the focal plane. This secondary light source again undergoes sample aberrations on the return path. Due to the extended nature of the secondary light source, the return path does not necessarily overlap with the excitation path, thus resulting in different aberrations for the two pathways. This is illustrated with a simulation in Fig. 2.3 (see Methods for details on simulation). Fig. 2.3 a shows the simulated optical system, a simplified version of the actual setup: light is focused through an aberrating phase mask onto a reflecting surface with a lens. The reflected light passes again through the lens and the phase mask and is focused onto a detector with a second lens. Fig. 2.3 b shows the resulting reflected focus image (bottom row) after passing a plane wave (top row) through the optical system (see figure legend for details). As seen in Fig. 2.3 c, for a weak aberration consisting of radial even Zernike modes, the combined aberrations accumulated in the excitation and detection pathway double (as expected, see [54]), resulting in the interference pattern in the focal volume (bottom row). In contrast, odd radial Zernike modes cancel [54], and a diffraction limited focal volume is preserved (Fig. 2.3 d, bottom row). However, for stronger aberrations from odd radial Zernike modes (Fig. 2.3 e) differences in the excitation and detection pathway lead to only incomplete cancellation of aberrations in the focal volume. Differences in excitation and detection path lead to the asymmetric reflected phase pattern (Fig. 2.3 e, second row from top) and result in a distorted reflected focal volume. This also suggests that in such a situation the odd components can be detected.

Taking such differences in excitation and detection aberrations into account, we generated datasets modeling three different sample configurations. First, we modeled the situation of a planar reflecting object with entirely uncorrelated excitation and detection aberrations with randomly selected Zernike modes of up to order 28 in both pathways

(Network 1, see Methods for details). Secondly, modeling the expected similarity between excitation and detection aberrations in weakly scattering samples, we used a dataset with a variance of ± 30 % between excitation and detection Zernike coefficients to constrain the sample space (Network 2). Third, to model scattering from a guide star, we generated a dataset with only detection modulations, while focusing with the unmodulated excitation beam at the mirror surface (Network 3).

These datasets of (pairs of) phase modulations together with the corresponding reflected focus images, were then used for training deep neural network models. The pairs of phase patterns in the excitation and detection path served as an output, and images of the reflected focal spots from the three cameras in different focal planes served as the input. After training, these networks predict Zernike coefficients for the excitation as well as the detection pathway based on images of the focal light distribution obtained when imaging through scattering samples. In this way, a correction of the excitation beam that is not confounded by aberrations in the reflected beam can be extracted.

2.2.1 Methods

Setup

The setup, shown schematically in Fig. 2.1 and in detail in Fig. 2.7, consists of a custom-built two-photon microscope equipped with a resonant scanner and controlled through ScanImage [44] with an added detection path for reflected light. Both the excitation path, as well as the reflected detection path are independently modulated with a spatial light modulator (SLM).

The excitation beam is expanded, reflected off the SLM, demagnified, and imaged onto the scanner through a polarizing beam splitter (PBS) (see legend of Fig. 2.7 for details). The (linear) polarization direction is adjusted for maximum transmission through the PBS with a half-wave plate. The scanner is imaged onto the back focal plane of the objective. A quarter wave plate is placed after the tube lens to achieve circular polarization and to optimize reflected light transmission through the PBS with orthogonal linear polarization with respect to the excitation light [71]. Reflected light is detected in a descanned configuration through the polarizing beam splitter, imaged onto a different part of the SLM and imaged onto a pinhole. The pinhole is imaged onto three cameras in different focal planes using 50/50 beam splitters and relay lenses. One camera focal plane was selected at the focus, one in front and one behind the focus (see for example

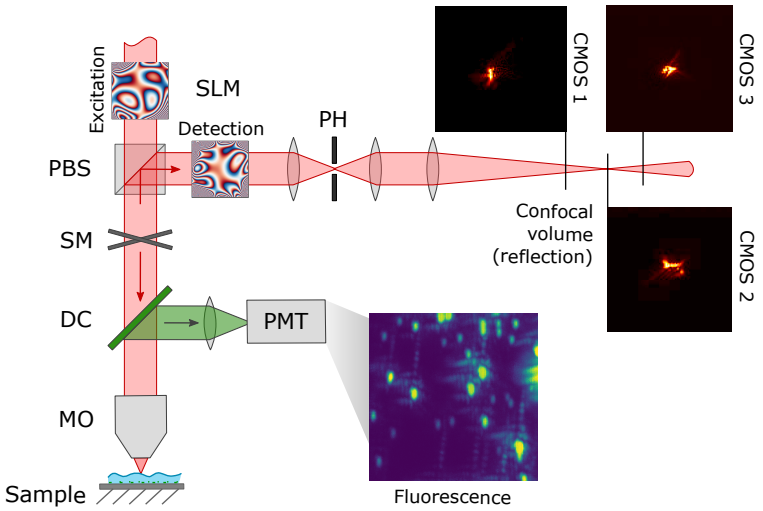

Figure 2.1: Setup schematic. Fluorescence is observed using two-photon scanning microscopy. Excitation and detection pathways are each controlled with an SLM. Reflected light is imaged in an epi-detection configuration onto three cameras. MO = microscope objective, DC = dichroic mirror, SM = scanning mirrors, PBS = polarizing beam splitter, SLM Excitation = spatial light modulator in excitation pathway, SLM Detection = SLM in detection pathway, PH = pinhole, CMOS 1-3 = cameras, PMT = photomultiplier tube. See legend to Fig. 2.7 for details.

[87, 143, 140]).

For independent excitation and detection path modulation, the SLM was divided into two equal parts, each having a size of 960×1080 pixels. The SLM was controlled through custom software written in Python using Blink SDK provided by Meadowlark Optics. To precisely center the phase modulations displayed on the SLM with respect to the beam, for initial alignment a center-symmetric phase pattern was displayed subsequently in both parts of the SLM. The center pixel of the respective SLM window was found by moving the pattern until the reflected focus was center-symmetric. The polarization direction of the beam imaged onto the SLM was optimized for modulation using lambda-half plates in both the excitation and detection pathways (see Fig. 2.7).

Relationship between excitation and detection path phase patterns

To calibrate the relation between excitation and detection pathways, which was required for experiments with guide stars (see below), we calculated a linear correspondence model (matrix) between excitation and detection Zernike modes. For this purpose a mirror was placed at the sample plane and random modulations were displayed in the excitation path.

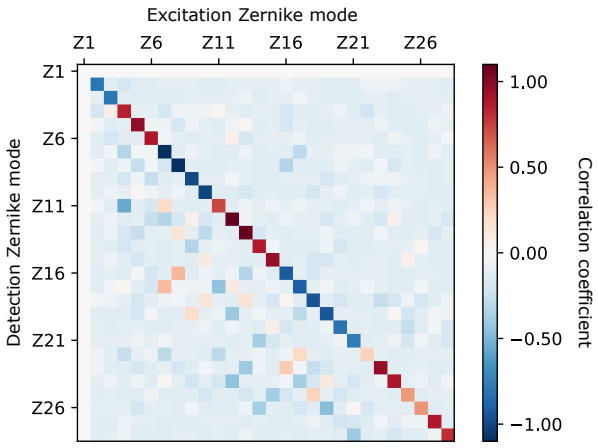

Figure 2.2: Linear correspondence model between Zernike modes displayed in the excitation and detection pathway (see Methods for details). Even components in the excitation are sensed with the same magnitude in the detection, and odd ones are sensed with a negative magnitude.

The resulting reflected confocal images were fed into Network 3 (trained on detection modulations only). With a set of 10 000 modulations applied in the excitation path and predicted as detection-path aberrations, a matrix relationship was determined (Fig. 2.2). The magnitude difference between excitation and detection phase corrections in the two pathways was taken into account in all generated datasets. The matrix shows that, as expected, even components in the excitation are sensed with the same magnitude in the detection, and odd ones are sensed with a negative magnitude.

Simulations

Using a Rayleigh-Sommerfeld solver [144], we simulated light propagation through the microscope and sample and monitored the point spread function at the sample and reflected focal plane (Fig. 2.3). The simulated pathway is illustrated in Fig. 2.3 a: a flat wavefront enters the microscope objective, propagates to the surface of an aberrating layer (which adds a spatial phase modulation to the beam), reaches the mirror (the PSF is calculated in this plane), is reflected back, passes again through the lens and the aberrating layer and is finally focused with a lens in the reflected focal plane (see legend of Fig. 2.3 for parameters used).

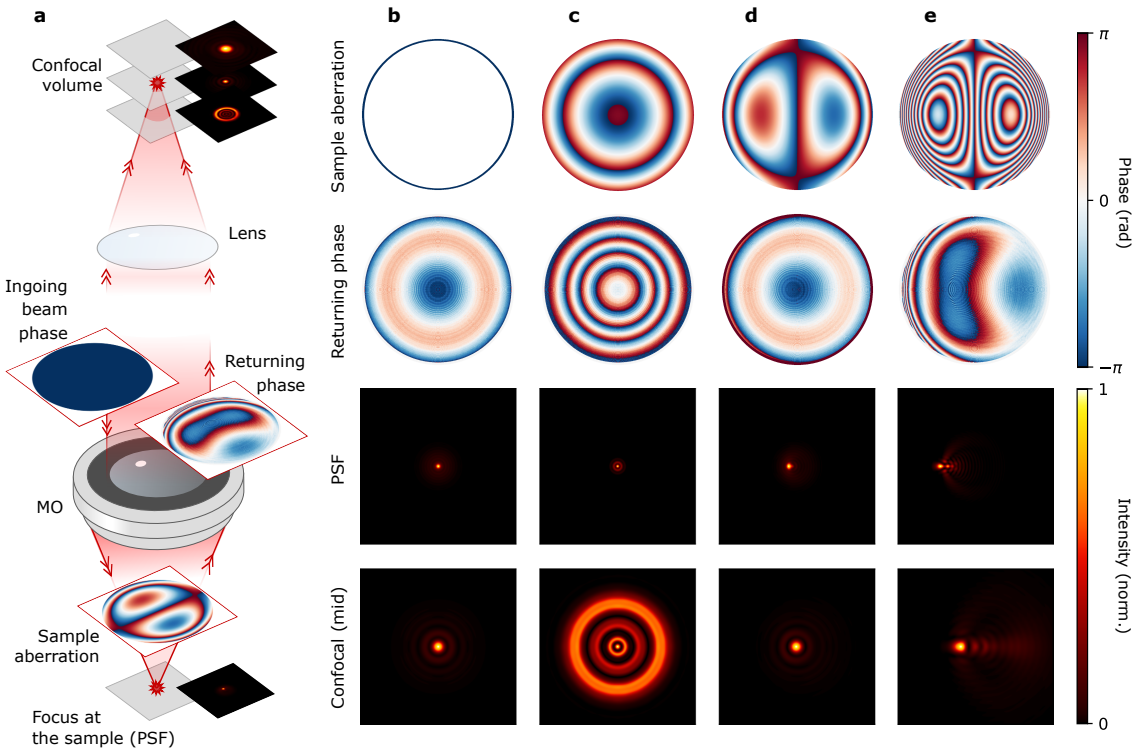

Figure 2.3: Simulation of impact of different aberrations on resulting reflected focal volume. **a** Schematic of the simulated optical system (see Methods for details). A flat wavefront enters the microscope objective and undergoes sample-induced phase modulation at the distance of 0.5 mm from a mirror surface on the excitation and reflected return path; the returning beam is focused with a 200 mm lens. The PSF at the sample and reflected focal planes are simulated. **b** Example with no aberrations. Top row: flat wavefront, second row: reflected wavefront, third row: focus at sample plane, bottom row: focus at reflected volume. **c** Aberration of even radial order which magnifies itself on the return path. **d** Self-correcting aberration of odd radial order. **e** Same as **d**, but with higher magnitude of phase aberration, demonstrating the failure of self-correction in this situation.

Data processing and neural network approach

The CNN architecture consisted of a cascade of 4 convolutional layers with ReLu activations (64 filters 11×11 with stride 4×4 and batch normalization, 64 filters 5×5 with stride 2×2 and batch normalization, 128 filters 3×3 with 2×2 max pooling, and 192 filters 3×3 with 2×2 max pooling respectively). These layers are followed by a dense layer with 3072 elements, sigmoid activation and 0.3 dropout regularization, and an output dense layer with linear activation, the size of which corresponds to the number of predicted Zernike modes. The networks were trained by minimizing mean absolute error (MAE) of the prediction with Adam optimizer at learning rate 0.0001.

The confocal volume (imaged in 3 planes) was normalized by dividing by 255 to bring the 8 bpp image to the $0 \ldots 1$ range and was stacked into a $192 \times 192 \times 3$ tensor serving as input for the network. The output was the corresponding phase modulation, represented as vector of Zernike coefficients $(Z1 \ldots Z28)$; in cases where both excitation and detection modulations were used, they were both concatenated into as single vector $(Z1_{\text{exc}} \ldots Z28_{\text{exc}}, Z1_{\text{det}} \ldots Z28_{\text{det}})$. Each random modulation was generated by shuffling a harmonic sequence $1.5\pi/n$ and randomly choosing the sign of each of its elements. For both excitation and detection the Z1 (piston) mode was set to 0.

2.2.2 Disentangling excitation and detection phase modulations

We first tested whether neural networks could extract random, independent phase modulations displayed in the excitation and at the same time in the detection pathway based on the resulting reflected focus patterns. We therefore generated a dataset by displaying different random Zernike modes of up to order 28 simultaneously in each pathway. A mirror was placed at the sample plane of the microscope and the resulting reflected focus images were recorded. This models a planar sample with entirely uncorrelated excitation and detection aberrations.

A network (Network 1) was trained on 180 000 such pairs of excitation and detection phase modulations and the resulting sets of confocal images. Fig. 2.6, top row, shows examples of predicted and target excitation and detection phase modulation with representative mean absolute errors. The mean absolute error (MAE) of the examples is also indicated in the full MAE distribution shown in the bottom row. The histogram of mean absolute error (MAE, Fig. 2.6, bottom row) between prediction and target modulations is compared to the error for random pairing (gray). These results show that the trained neural

network can reliably disentangle and predict independent excitation and detection phase patterns based on reflected confocal images resulting from the combined modulation.

2.2.3 Focusing through aberrating layers

We next tested whether such networks could be used to separate excitation and detection aberrations based on reflected images from actual scattering samples and whether the resulting corrections could be used for focusing through the encountered aberrations. In these experiments, we focused through a layer of vacuum grease onto a reflecting surface. To be able to directly monitor the focus after the scattering layer, we focused on a fifty-fifty beam splitter. This resulted in a reflected focus image and at the same time allowed monitoring the focus at the sample surface with a transmission camera for a stationary beam (non-descanned transmission detection, see Fig. 2.7). To monitor the correction during scanning, we placed fluorescent beads (0.1 μm diameter) on the beam splitter surface and detected fluorescence using two-photon imaging.

Corrections were computed using Network 2 which was trained on a dataset of 180 000 examples with a variance of $\pm$30 % between excitation and detection Zernike coefficients. This allowed better coverage of the sample space compared to Network 1 (with similar sized training datasets) and was sufficient for correcting aberrations in weakly scattering samples. Examples of network predictions with representative MAEs are shown in Fig. 2.6, top row. The MAE of the examples is indicated in the MAE distribution shown in Fig. 2.6, bottom row.

Representative examples of two-photon images of fluorescent beads on the reflecting surface with and without excitation correction are shown in Fig. 2.4. Due to aberrations the center plane of the confocal volume is difficult to determine, and corrections were therefore obtained by averaging between three and five images of the confocal volume at different axial positions around the estimated center (separated by 2-5 micrometers). Confocal images were normalized the same way as training images (see Methods) and independently fed through the network and the predictions were averaged. The network output is a vector of Zernike coefficients and excitation and detection aberration were generated. To correct for aberrations, the complex conjugate of the network output was displayed on the SLM.

Fig. 2.4 a shows that aberrations in the fluorescence images can be corrected based on the reflected excitation light using the trained neural network. The improved focus

(monitored with a transmission camera, 2.4 b and f), leads to improved resolution and signal as seen in 2.4 a and c, and e and g, respectively. (Note that the beads were placed on top of a beam splitter, so reflection from the beam splitter will likely distort the axial profile shown in Fig. 2.4 a and e on the right side.) Overall, the decomposition into an excitation and detection pathway leads indeed to the formation of an improved focus suitable for two-photon imaging.

We implemented a second imaging approach based on deep learning with scattering guide stars. Since for a guide star the observed focus distortion in the sample is a result of only return path aberrations, we trained a network on detection-only modulations (Network 3). Examples of predicted and target corrections are shown in Fig. 2.6, top row. The MAE of the examples is shown in the distribution in the bottom row.

The confocal volume was imaged and corresponding aberrations of the return path were predicted with the network. The correction is carried over to the excitation path using the correspondence model between excitation and detection path Zernike modes (see Methods and Fig. 2.2). The sample consisted of a mixture of scattering guide stars (9 μm diameter silver coated silica microspheres, Cospheric) and 0.1 μm fluorescent beads embedded in 1 % Agarose. (The transmission focus was not monitored directly in this case, since the focus was inside a volume, not at an interface as above.) The sample was again imaged through a layer of vacuum grease. Experiments were performed as above, with averaging over between three and five focal planes. Fig. 2.5 a and Fig. 2.5 d show two representative examples of corrections achieved with this approach. Both resolution and intensity improve due to the applied corrections.

2.3 Discussion

We have developed an adaptive optics approach for laser scanning microscopy based on reflected light imaging and deep neural networks. For network training large datasets of aberrated focus images were generated by combined excitation and detection pathway phase modulations, modeling the aberrations observed from extended reflecting objects in scattering samples. After training on such datasets, deep neural networks can extract underlying excitation and detection phase aberrations of modeled and actual samples based on reflected focus images (Fig. 2.6). We validated this approach using two-photon imaging of fluorescent beads distributed on a mirror through an aberrating sample as well as by directly imaging the transmitted focus (Fig. 2.4 and Fig. 2.5). The resulting corrections

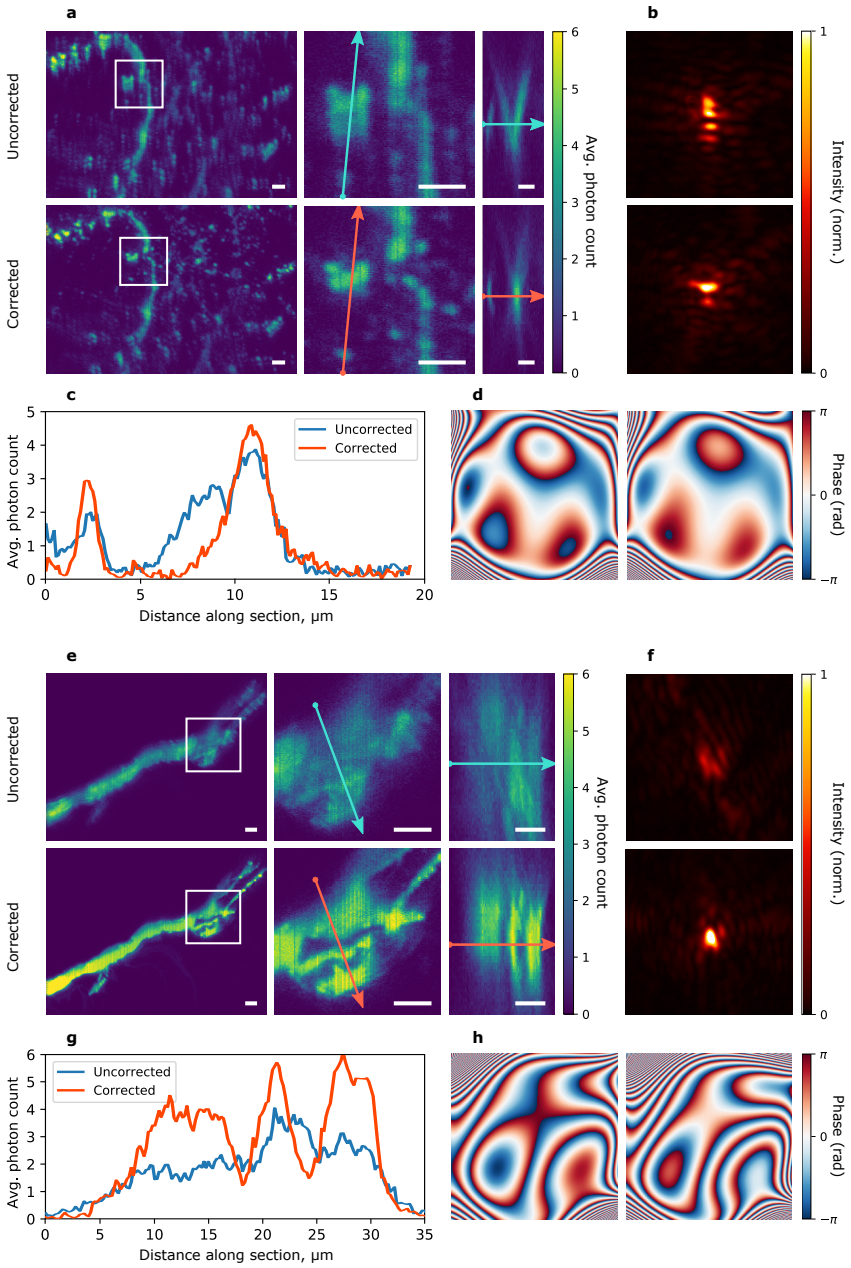

Figure 2.4: Aberration correction for imaging through scattering layer on planar reflector. **a** Left: example of corrected and uncorrected image of fluorescent beads distributed on reflector surface imaged through a layer of vacuum grease. Center: white frame in left figure. Right: axial cross section through lines in center figure recorded in a z-stack with 1 μ m step size. **b** Top: uncorrected focus at center of field-of-view in **a**. Bottom: corrected based on reflected light. Colorscale is saturated in the corrected image, so that aberrations in the uncorrected image are visible. **c** Cross sections for uncorrected (blue) and corrected (red) images along the lines indicated in figure a, center. **d** Left: excitation and Right: detection phase mask. **e-h** Same as **a-d** for a second example. All scale bars are 5 μm.

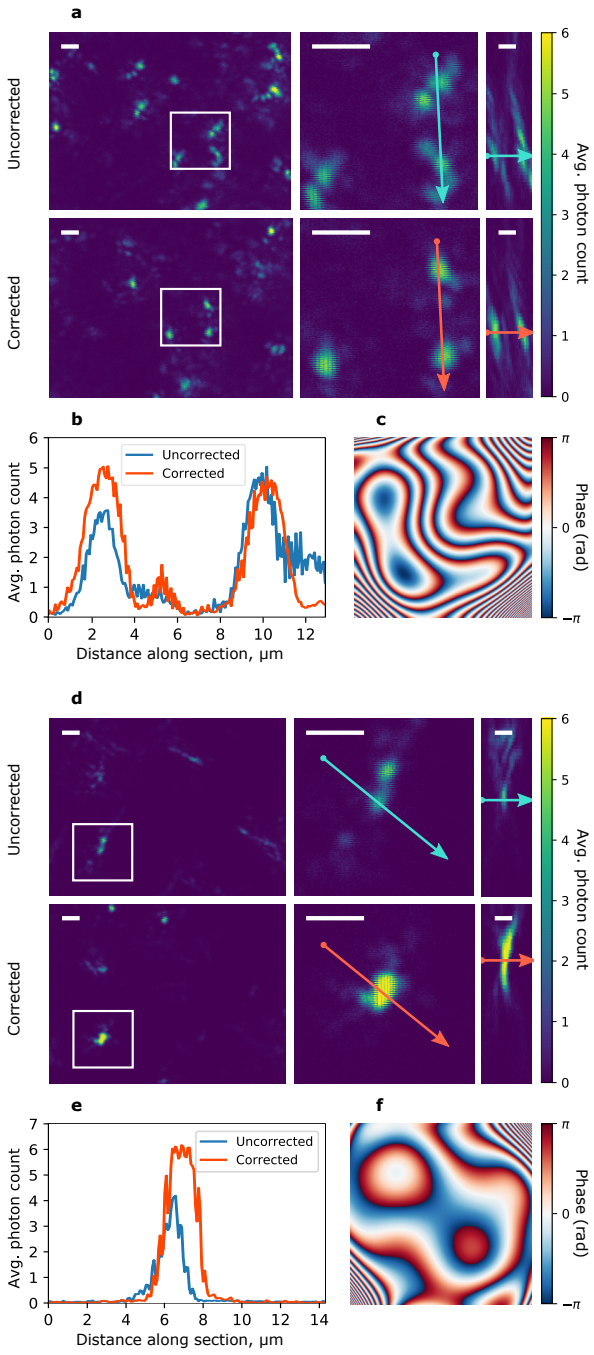

Figure 2.5: Aberration correction for imaging through scattering layer with guide stars. **a** Left: example of corrected and uncorrected image of fluorescent beads distributed in a volume of Agarose mixed with scattering guide stars imaged through a layer of vacuum grease. Center: white highlighted box in left figure. Right: axial cross section through lines in center figure recorded in a z-stack with 1 μ m step size. **b** Cross sections for uncorrected (blue) and corrected (red) images along the lines indicated in **a**, center. **c** Excitation phase mask. **d-f** Same as **a-c** for a second example. All scale bars are 5 μm.

achieved for a planar object rely neither on a tight focal volume nor a guide star, as typically necessary for wave front sensing.

In a second approach, we obtained corrections by combining guide stars and deep neural networks. In this situation, training data was modeled using only detection path modulations and the corresponding corrections were then displayed in the excitation pathway for excitation correction.

Reflected light detection generally has the advantage of being independent of sample labeling [70], but comes with the difficulty of separating excitation, detection, and sample contributions to the scattered signal [134, 136]. We addressed here the problem of separating excitation and detection aberrations with a deep neural network approach and independent phase modulation of both pathways. While we used either a reflecting surface or a guide star as reflectors, sample scattering characteristics could for example be included by recording training data from biological samples.

For two-photon imaging experiments we introduced a coupling between excitation and detection corrections with a variance of ± 30 % between excitation and detection Zernike coefficients to constrain the space of possible aberrations and to limit the required amount of training data. Using larger datasets will allow relaxing this constraint and to address larger differences in excitation and detection aberrations as observed in more strongly scattering samples [134]. Additionally, we obtained best corrections by averaging over three to five different excitation focal planes and larger data sets will likely improve single shot predictions suitable for the fast frame rates required for dynamic biological samples.

Aberration corrections could additionally be improved by including higher order Zernike modes. In the current implementation, Zernike polynomials of up to order 28 were used, similar to previous approaches using wavefront sensors [71]. Up to 120 orders have for example been measured in a transmission configuration using a combination of deep neural networks and wavefront sensors [93], suggesting that higher order modes could also be detected in reflection mode imaging. In addition to larger datasets, also different network architectures that would benefit from such larger datasets could be used, such as ResNet [145] or Inception [92].

Alternatively to Zernike polynomials (deep) neural networks can also be trained with different basis sets (see for example [146]) which could potentially better match actual sample scattering characteristics. As an alternative to generating training data with an

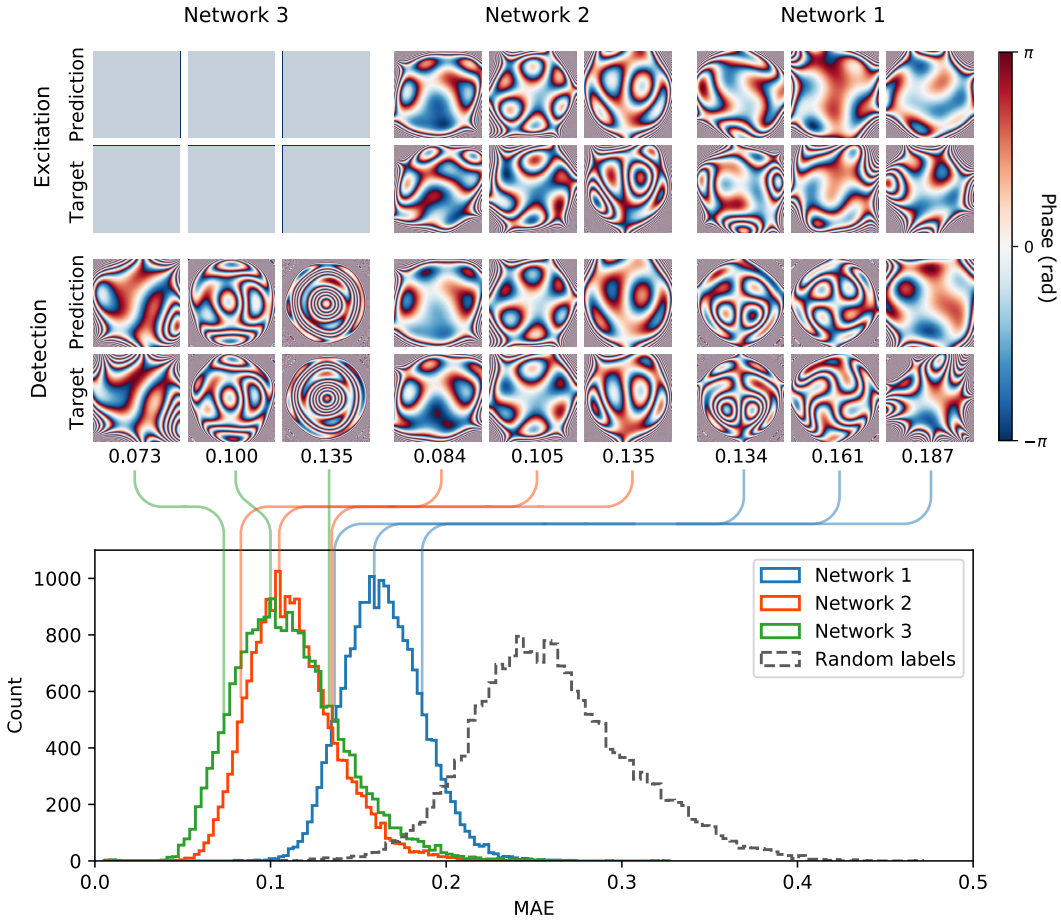

Figure 2.6: Top row: Examples of pairs of network predictions and targets for all three networks used for excitation pathway. Samples are drawn as indicated by colored lines at respective positions in the pertaining error distributions. Center row: Same as top row for detection pathway phase patterns. Bottom: Histograms of mean absolute error (MEA) between predicted and target phase masks for the three different networks, compared with errors obtained for random pairings.

SLM, also entirely computationally generated datasets could be used (as for example in [90, 92]). This would allow simulating datasets with scattered light distributions matched to those observed in samples of interest. Overall, the approach outlined here offers a versatile framework for excitation and detection aberration corrections that is independent of sample labeling and can be integrated with laser scanning microscopy.

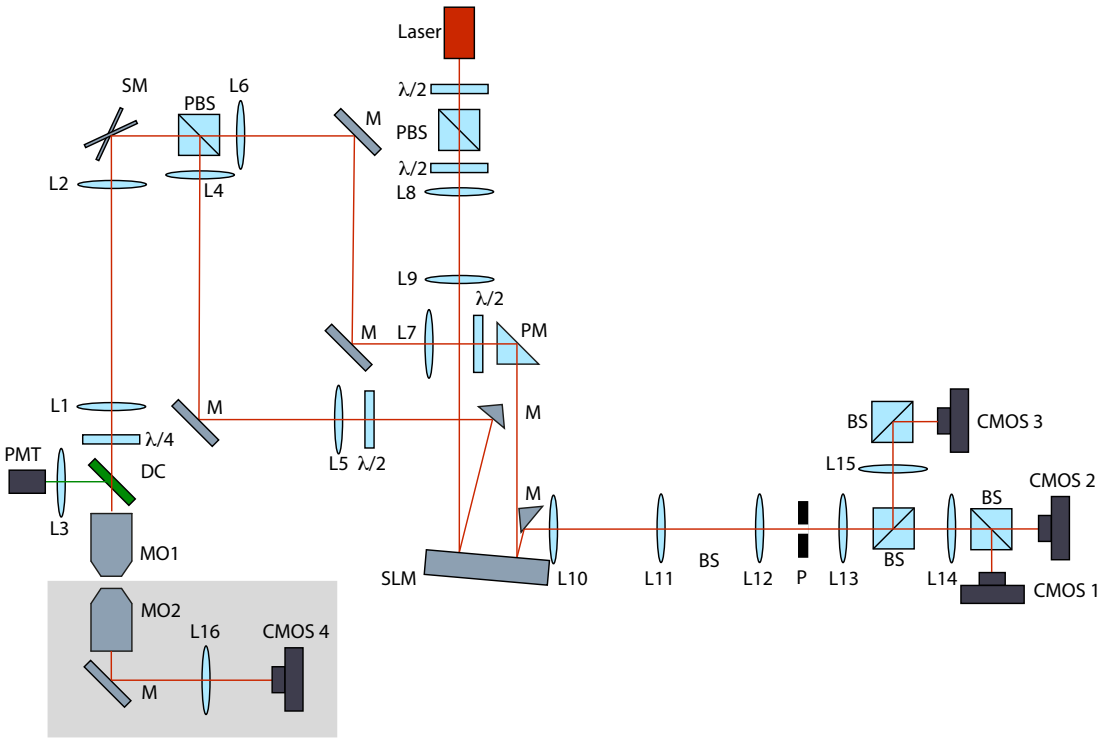

Figure 2.7: MO1 = Nikon 16 x, N.A. 0.8, water immersion objective (CFI75 LWD 16X W), MO2 = Olympus 40x, N.A. 0.8, LUMPLFLN. All lenses were from Thorlabs, achromatic doublets, antireflection coated for 650 to 1050 nm. Focal lengths were (in mm) L1 = 300, L2 = 30, L3 = 50, L4 = 125, L5 = 300, L6 = 100, L7 = 400, L8 = 75, L9 = 250, L10 = 150, L11 = 150, L12 = 40, L13 = 50, L14 = 75, L15 = 75, L16 = 300. PBS = polarizing beam splitter, BS = beam splitter, (both antireflection coated for 650 nm to 1050 nm), $\lambda/2$ = polymer zero order half-wave plate (WPH05ME-980), PM = reflecting prism mirror, P = pinhole with 300 μm diameter, CMOS = CMOS cameras (Basler, acA640-750um), SLM = spatial light modulator (Meadowlark, HSP1920-1064-HSP8), M = mirror, DC = dichroic mirror, SM = resonant scanning mirror, PMT = photomultiplier tube for fluorescence detection (two-photon imaging). The transmission pathway (light-gray box) was only used for observing the resulting corrections for a stationary excitation beam and was not used to compute corrections.

CHAPTER 3

Differentiable model-based adaptive optics with transmitted and reflected light

This chapter was published as a peer-reviewed paper in the *Optics Express* journal by the *Optical Society of America* in 2020 [126].
The authors are Ivan Vishniakou and Johannes D. Seelig.
https://doi.org/10.1364/OE.403487

3.1 Introduction

Machine learning offers novel approaches to correct for aberrations encountered when imaging through scattering materials, [128, 129, 130, 136] from astronomy [87, 90, 138, 92] to microscopy with transmitted (for example [141, 93, 147]) and reflected light [125]. To find aberration corrections in these situations, machine learning typically relies on large synthetic datasets. Large datasets are required, first, because the many parameters of deep neural networks need to be adjusted to work under a wide range of conditions and all these conditions need to be covered in the training data. Secondly, machine learning models are typically agnostic about the underlying image generating process. Therefore, even *a priori* known information, for example the transformations inside the optical system, needs to be learned from data.

In practice, training datasets are often based on combinations of Zernike polynomials [87, 90, 138, 92, 141, 93, 147, 125] which might however not accurately capture all aspects of experimentally encountered aberrations. Additionally, for more strongly scattering samples, which require increasingly higher orders of Zernike modes, covering all potential

scattering situations by sampling a sufficient number of different mode combinations eventually results in very large datasets. This is in particular the case if aberrations in multiple layers are combined, for example when using reflected light in an epidetection configuration [125].

While finding inverse models through such data driven strategies is well suited for situations where the underlying physical model is undetermined, the image formation process in an optical system is typically at least partially known. This is the basis of model-based adaptive optics, where optical systems modeling is combined with optimization to find an unknown phase aberration [148, 149, 150, 151]. Similar situations where models based on a well known underlying physical process are learned from data are also encountered in other imaging modalities [152], and more broadly many areas of engineering and physics (for example [99, 153, 154, 155, 123, 121, 122, 120]). To take advantage of such prior information, methods have been developed that combine physical process models with machine learning optimization.

For such optimization, first a model is described as a differentiable function mapping input to output. Since the function is differentiable, one can take advantage of automatic differentiation, which is more accurate and computationally efficient than finite differences [156, 157, 158], and is one of the cornerstones of machine learning frameworks such as Tensorflow. Automatic differentiation is used in these frameworks to compute gradients for optimization of a loss function with respect to parameters of interest. The loss function compares model output to a target output and the discrepancy is minimized by adjusting model parameters ([99, 153, 154, 155, 123, 121, 122, 120]).

Here, we employ this model optimization strategy for adaptive optics: we describe light propagation through the optical system, including unknown aberrations represented as parameters, with a differentiable model (Fig. 3.1). For matching the input-output relationship of the computational model to the experimental setup we record a number of output images resulting from corresponding input phase modulations and optimize model parameters using Tensorflow. We show that this allows extracting an accurate description of the introduced aberrating layer(s) as verified by focusing in transmission through a single layer, as well as in a reflection, through two layers. In the latter epidetection configuration only reflected light is used for optimization and transmission focusing.

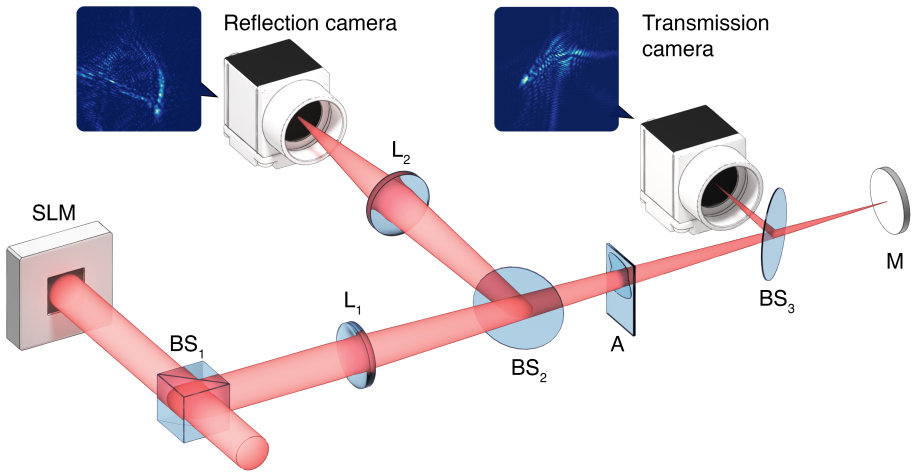

Figure 3.1: Schematic of experimental setup. Light reflected off a spatial light modulator (SLM) passes through an aberration (A) and is focused onto a camera (transmission camera, shown with illustration of imaged light distribution). For experiments in an epidetection configuration, light reflected off the mirror M at the sample plane is additionally recorded with a second camera (reflection camera). BS = beam splitter, L = lens (see main text and Methods for details).

3.2 Results

The experimental setup is shown schematically in Fig. 3.1. An expanded and collimated laser beam is reflected off a spatial light modulator (SLM) with a beam splitter cube (BS_1) and a part of the beam is imaged onto a camera (transmission camera) over a beam splitter (BS_3). For experiments with reflected light, the remaining part of the beam is additionally sent to a mirror at the sample plane (same focal plane as the transmission camera) which serves as a proxy for a reflecting sample. Light reflected by the mirror is imaged onto a second camera (reflection camera) with a beam splitter (BS_2). Aberrations (a layer of nail polish on a microscope slide, see Methods) are introduced between beam splitters BS_2 and BS_3. The beam undergoes aberrations once to the transmission camera, and twice to the reflection camera.

A single transmission pass through the setup is described by the function (see Methods for details)

$$S(\phi_{\mathrm{SLM}}, \phi_{\mathrm{aberration}}) = \left| P_{f_1}\left(\exp\left[i\phi_{\mathrm{aberration}}\right] \exp\left[i\phi_{\mathrm{lens}}\right] P_{f_1}\left(U_0 \exp\left[i\phi_{\mathrm{SLM}}\right]\right)\right)\right|^2, \qquad (3.1)$$

where P_d is a propagation operator over the distance d, U_0 is the complex amplitude of the

unmodulated beam at the SLM, ϕ_{lens} is the phase representation of the lens L_1, and f_1 is its focal length; ϕ_{SLM} is the (known) SLM phase modulation, and $\phi_{\text{aberration}}$ is the (unknown) introduced aberration.

For computational efficiency, the aberration is simulated at the same plane as lens L_1 (see Methods). Finding the unknown aberration which maximizes the similarity, measured with Pearson's correlation coefficient r, of the simulated camera images $S(\phi_{\text{SLM}}, \phi_{\text{aberration}})$ and experimentally recorded images I was solved in Tensorflow using automatic differentiation and gradient-based optimization (see Methods):

$$\phi_{\text{aberration}} = \underset{\phi_{\text{aberration}}}{\arg\max}(r\,[S(\phi_{\text{SLM}}, \phi_{\text{aberration}}), I]). \tag{3.2}$$

To further refine the focus after a first optimization step, a second step was performed with a new set of modulations and corresponding images. In this second step, the correction obtained in the first optimization step was added to all modulations displayed, $\phi_{\text{SLM}} + \phi_{\text{correction}_1}$. The final correction was the sum of the first and second step correction $\phi_{\text{correction}_1} + \phi_{\text{correction}_2}$. We used 180 modulations for transmission and 540 for reflection experiments in each of the two iteration steps.

As seen for two representative examples in Fig. 3.2 a, b and d, e, respectively, optimization (which results in the corresponding phase profile in Fig. 3.2 c, f) leads to closely matching (correlation coefficient r is indicated in Fig. 3.2 b, e) measured and predicted light distributions at the sample (transmission camera) after applying the correction at the SLM. The similarity is quantified with the loss function $1 - r$ in Fig. 3.2 o. To verify the achieved correction, the optimized aberration found at the plane of lens L_1 was propagated back to the SLM (see Methods) and the corresponding correction (Fig. 3.3 c and f) was displayed. This led to a focus at the sample or camera plane as shown with two representative examples in Fig. 3.3 b, e (Fig. 3.3 a, d shows the focus before correction) together with an increase in enhancement by a factor of 10 and 3.4, respectively (see Methods for definition of enhancement and details). (Note the difference in color scale between different images, normalized to maximum (max) values indicated in the subfigures.)

In an epidetection configuration, as typical for imaging in biological samples, only reflected light can be used for finding a correction. Reflected light however accumulates a first aberration encountered in the excitation pass and a (generally different) second aberration in the reflection pass [136, 125]. These need to be disentangled for example

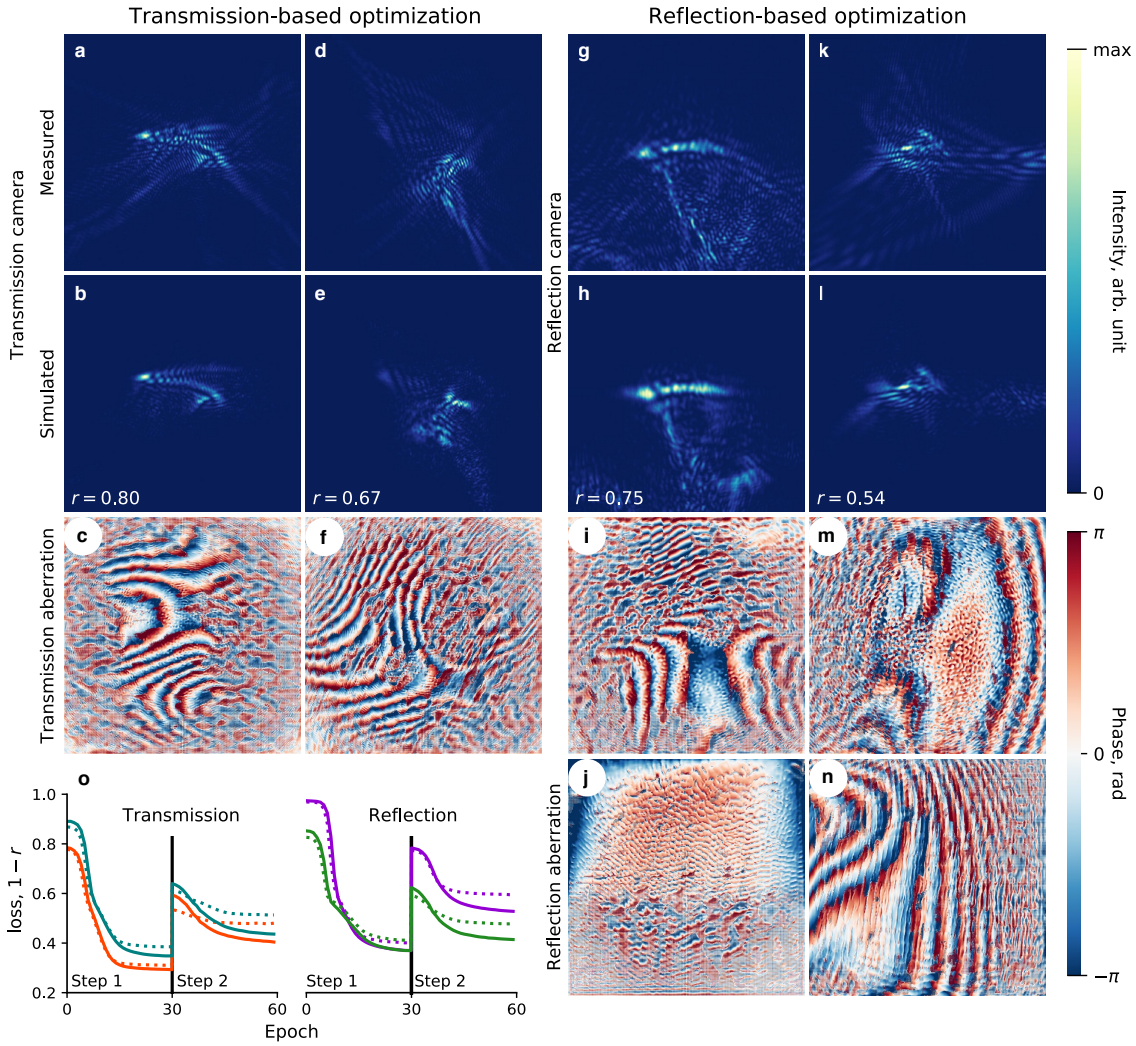

Figure 3.2: Model matching and optimization: **a-f** Transmission-based. **a, d** Two examples of measured, aberrated transmission light distributions and **b, e** matching simulated light distributions after the first optimization step. **c, f** Corresponding phase profile (obtained at lens plane, after first optimization step). **g-n** Reflection-based. **g, k** Two examples of measured, aberrated, reflection light distributions and **h, l** matching simulated light distribution after first optimization step. **i, m** Corresponding transmission and **j, n** reflection phase results after first optimization step at the planes of lenses L_1 and L_2, respectively. **o** Transmission, orange: loss function for training of first example (a-c), and validation (dotted). Vertical line separates first and second optimization step, see Methods. Transmission, teal: same as orange for second example (d-f). Reflection, green: same for reflection experiment (g-j). Reflection, violet: same for second example in reflection experiment (k-n). r in b, e, h, l is Pearson's correlation coefficient (with corresponding image in in a, d, g, k), field of view is 1766 μm by 1766 μm.

to recover a transmission pass correction required for generating a focus inside a sample. For focusing in transmission using only reflected light therefore the function S (equation 3.1) is extended (see Methods) to include the reflection pass from the mirror at the sample plane through the aberration to the second camera (reflection camera), now including an aberration in the transmission as well as in the reflection pass. This model is fitted to match observed reflected light distributions by optimizing at the same time two independent aberrations. Optimization is performed as before (see Methods).

Two representative examples of predicted and measured light distributions at the sample plane (transmission camera) are shown in Fig. 3.2 g, h and k, l, respectively, and the loss function quantifying the similarity is shown in Fig. 3.2 o (correlation coefficient r between predicted and measured distributions is indicated in Fig. 3.2 h, l). The corresponding transmission and reflection phase aberrations at the plane of lens L_1 and L_2 are shown in Fig. 3.2 i, j and m, n, respectively. To verify the correction, we generated a focus at the sample plane by displaying the corresponding transmission correction on the SLM (see Methods). Fig. 3.3 shows two representative examples (g-i and j-l) of aberrated focus, corrected focus, and corresponding correction (resulting in an increase in enhancement by a factor of 10.4 and 8.7, respectively, see Methods). In reflection-based transmission control, the obtained focus was not necessarily centered in the field of view (as for example seen in Fig. 3.3 j, k), due to tilt introduced by the sample that was not corrected. Importantly, in reflection-based transmission control experiments, focusing in transmission is achieved only using reflected light, compatible with an epidetection configuration.

For reflection-based transmission control, aberrations in two different focal planes are independently computed at the same time. This is similar to multiconjugate adaptive optics, where typically however an additional SLM is used to correct for a second focal plane [159, 160, 161]. Additionally, while we generated single focal spots, arbitrary other focal distributions could be generated as well (for example for applications in optogenetics).

3.3 Methods

3.3.1 Experimental setup and data acquisition

The laser was from Toptica (iBeam smart, 640 nm), the spatial light modulator from Meadowlark (SLM, ODP512-1064-P8), cameras were from Basler (acA2040-55um). All optical parts were from Thorlabs: BS_1 in Fig. 3.1 was BS016, BS_2 and BS_3 were EBS2.

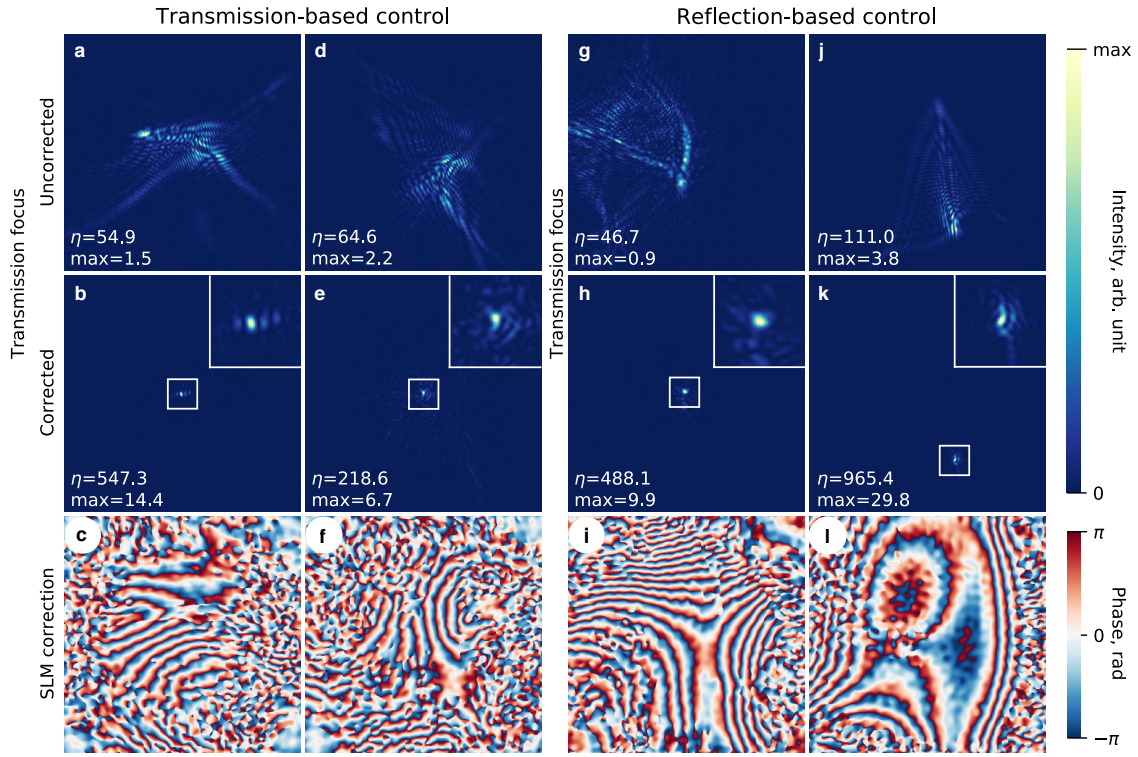

Figure 3.3: **a-f** Focusing in transmission. **a, d** Two examples of aberrations recorded in transmission. **b, e** Focus after correction with blow-up of focal spot (white frame and inset). **c, f** Wavefront correction at SLM after two-step optimization. **g-l** Focusing in transmission using reflected light. **g, j** Two examples of aberrations recorded in transmission. **h, k** Transmission focus after correction only using reflected light, with blow-up of focal spot (white frame and inset). **i, l** Transmission wavefront correction at SLM after two-step optimization recovered from only reflected light measurements. In each subfigure, max indicates maximum of colorbar, η is enhancement (see Methods), field of view is 1766 μm by 1766 μm.

Lenses were visible achromats, L_1 with focal length 300 mm (AC254-150-A) and L_2 with 150 mm (AC254-150-A). Data were collected by placing an aberrating sample in the optical path between BS2 and BS3 (see Fig. 3.1), displaying random SLM phase modulations, and recording the resulting 512×512 images with the transmission camera, and additionally with the reflection camera for reflection experiments. Random SLM phase modulations were generated by summing the first 78 Zernike modes with random coefficients drawn from a normal distribution with standard deviation π and displayed at a resolution of 512×512 pixels on the SLM.

The light intensity in transmission and reflection can vary by several orders of magnitude, exceeding the dynamic range of the cameras. Therefore, in order to capture the full range of intensities, multiple frames with different exposure times were recorded (each frame with a 12-bit per pixel resolution). In transmission, each frame was recorded with exposures of 60, 120, and 250 ms, respectively, and the resulting image was the sum of the recorded frames weighted by the inverse of the exposure time. Saturated pixels as well as pixels below the noise threshold were discarded. For the reflection camera, images were taken with exposures of 60, 120, 250, 500, and 1000 ms, respectively. Additionally, transmission light intensity was reduced with a neutral density filter wheel (NDM2/M, Thorlabs).

3.3.2 Computational model

Light travelling through the setup is modeled as a complex amplitude $U(x,y,z)$, initialized with $U_0 = U(x,y,0)$, and propagating through a sequence of planar phase objects and intermittent free space along the optical axis (z-axis; x, y, z are spatial coordinates). A wavefront $U(x,y,d)$ interacting with a phase object $\phi(x,y,d)$ at plane d is described as a multiplication

$$U(x,y,d)\exp\left[i\phi(x,y,d)\right]. \tag{3.3}$$

Free space propagation of the wavefront over a distance d is calculated using the angular spectrum method with the following operator [5]:

$$\begin{aligned} U(x,y,z+d) = P_d(U(x,y,z)) = \iint A(f_X,f_Y;z)\,\mathrm{circ}\left(\sqrt{(\lambda f_X)^2+(\lambda f_Y)^2}\right) \\ \times H \exp\left[i2\pi(f_X x + f_Y y)\right] \mathrm{d}f_X\,\mathrm{d}f_Y. \end{aligned} \tag{3.4}$$

Here, $A(f_X, f_Y; z)$ is the Fourier transform of $U(x,y,z)$, f_X, f_Y are spatial frequencies, the circ function is 1 inside the circle with the radius in the argument and 0 outside [5], and $H(f_X, f_Y) = \exp\left[i2\pi\frac{d}{\lambda}\sqrt{1-(\lambda f_X)^2-(\lambda f_Y)^2}\right]$ is the optical transfer function. The intensity measured by the camera is given by

$$I(x,y,z) = |U(x,y,z)|^2 . \tag{3.5}$$

3.3.3 Model optimization

We used a Python library for diffractive optics [144] to calculate the known factors of (3.1). By providing the focal lengths and setup dimensions, discretized versions of the optical transfer functions for the propagation operators and the phase representation of the lenses were determined. The resulting function which relates displayed, known SLM phase modulations and unknown sample aberrations to camera images, was then transferred to Tensorflow. The position of the scatterer, as seen in expression (3.1), was simulated at the plane of lens L_1. This saves computations and memory, since each intermediate plane requires additional wavefront propagation calculations. Similarly, for computational efficiency, a single lens L_2 with focal length $f_2 = \frac{f_1}{2}$ was used to focus reflected light onto the reflection camera. While the parameters of the optical model for transmission and reflection were adjusted manually to match the setup, they can equally be tuned using the optimization approach described below, for example to obtain a system correction.

The model of light propagation in the setup, equation (3.1), was incorporated in the loss function according to equation (3.2):

$$\text{loss} = 1 - r\left[S(\phi_{\text{SLM}}, \phi_{\text{aberration}}), I\right], \tag{3.6}$$

where ϕ_{SLM} and $\phi_{\text{aberration}}$, are the phase modulations at the SLM and due to the introduced aberration, respectively. All variables are 512×512 real-valued tensors, and $\phi_{\text{aberration}}$ is the optimization variable.

Similar to the training of neural networks, we split the data into training and validation sets and used batches. We used Adam optimizer with learning rate 0.1 and batch size 30. Optimization with the loss function resulted in matching simulated and experimentally recorded images and yielded the phase profile of the aberration in the setup. The quality of the solution was quantified with the correlation between modelled and recorded images

in the validation part of the dataset and was used as the criterion for stopping the optimization. Convergence of the optimization process depended on the magnitude and spatial frequencies of the aberration and the number of samples. Typically a solution with $r > 0.6$ was sufficient for focusing.

For experiments with reflected light, the simulation of the setup was extended to include the reflected light pass,

$$\begin{aligned} S(\phi_{\text{SLM}}, \phi_{\text{trans}}, \phi_{\text{refl}}) = \mid & P_{f_1}(\exp[i\phi_{\text{lens}_2}]\exp[i\phi_{\text{ref}}] \\ & \times P_{2\cdot f_1}(\exp[i\phi_{\text{trans}}]\exp[i\phi_{\text{lens}}]P_{f_1}(U_0\exp[i\phi_{\text{SLM}}]))) \mid^2, \end{aligned} \tag{3.7}$$

and the loss function (3.6) is optimized with variables ϕ_{trans} and ϕ_{ref}.

3.3.4 Evaluation

After $\phi_{\text{aberration}}$ is found through optimization at the lens plane, the corresponding correction at the SLM is found by propagating the conjugate phase of the aberration backwards to the SLM plane $\phi_{\text{correction}} = \arg(P_{-f_1}(\exp[-i\phi_{\text{aberration}}]))$. Additionally, we smooth the found correction with a low-pass spatial frequency filter: discrete Fourier transform is applied to $\exp[i\phi_{\text{correction}}]$ and frequencies exceeding 0.1 of the pattern resolution are discarded. When displayed on the SLM, $\phi_{\text{correction}}$, this results in a compensation of the aberration.

Aberrations were introduced with a thin layer of transparent nail polish distributed on a microscope slide (inserted between BS_2 and BS_3). Two different aberrating samples were used for transmission and reflection experiments. Generally, the strength of aberrations varies depending on sample positioning. Optimization parameters (such as number of phase modulations or learning rate) were only adjusted once for transmission experiments, and once for reflection experiments. As a simple measure for quantifying the shape of the uncorrected light distributions, we use its maximum extension as measured by the length of the first principle component of the pixels above a 30 % intensity threshold, σ. To quantify the change in the distribution before and after correction we compared the uncorrected and corrected distribution, $\sigma_{\text{rel}} = \sigma_{\text{u}}/\sigma_{\text{c}}$. To additionally quantify the quality of the aberration correction, we also used an enhancement metric defined as ratio of maximum intensity to mean intensity in the frame, $\eta = \max(I)/\text{mean}(I)$, comparing it before and after correction $\eta_{\text{rel}} = \eta_{\text{c}}/\eta_{\text{u}}$. The distribution of these values $(\eta_{\text{rel}}, \sigma_{\text{rel}})$ for a series of 7 transmission experiments was: (10.0, 25.3), (1.7, 6.5), (3.4, 12.1), (2.6, 10.4),

(0.8, 1.2), (16.2, 25.4), (3.8, 9.8), $\langle \eta_{\mathrm{rel}} \rangle = 5.5 \pm 5.2$, $\langle \sigma_{\mathrm{rel}} \rangle = 13.0 \pm 8.5$; and in a series of 7 reflection-based transmission control experiments was: (10.5, 17.6), (10.4, 32.6), (11.6, 11.1), (7.2, 13.0), (8.7, 4.3), (4.4, 12.3), (1.9, 2.6), $\langle \eta_{\mathrm{rel}} \rangle = 7.8 \pm 3.3$, $\langle \sigma_{\mathrm{rel}} \rangle = 13.4 \pm 9.2$.

3.4 Discussion

Differentiable model-based approaches for image reconstruction have been introduced in several domains of imaging [152], for example in ptychography [123]. Instead of directly optimizing model parameters, an additional deep neural network (a deep image prior [106, 162]) has also been introduced, for example for phase imaging [121, 122] or ptychography [120].Even without such additional regularization, the optimization converged reliably to smooth phase patterns (Fig. 3.2 c, f, i, m, j, n and Fig. 3.3 c, f, i, l), but for example a DIP could also be combined with the introduced method to further reduce the number of samples used for optimization.

The number of required samples depends on the magnitude and spatial frequencies of the aberrations, requiring more samples with stronger aberrations. This can be compared to the training of deep neural networks, where the number of required samples for model training similarly increases with increasing aberrations. Compared to deep neural networks, including a physical model of the imaging process allows finding aberration corrections with a small number of samples (albeit only for a single field of view at a time). Different from neural networks which are trained on a predetermined distribution of aberrations (for example based on Zernike polynomials), optimization is achieved independently in each pixel without prior assumptions about aberrations.

Similar to other techniques that require multiple measurements for finding a correction [136, 148], a limitation of the presented approach for dynamic samples is the time it takes to find a correction. The optimization time, several minutes on a single GPU, could be reduced by using multiple GPUs. Generally, the gap between optimization and control (corresponding to rapidly changing corrections in response to aberrations) is expected to narrow with increasing computational power [163].

Thanks to advanced computational frameworks [144, 85], the introduced model-based optimization can easily be combined with any optical setup equipped with a spatial light modulator and a camera without requiring additional hardware such as wavefront sensors or interferometers. For example, the described technique could be combined with imaging through scattering materials in a microscope with a high numerical aperture objective in an

epidetection configuration [125]. In summary, we expect that the developed method will be useful in many situations that can benefit from correcting aberrations through single and multiple layers.

CHAPTER 4

Differentiable model-based adaptive optics for two-photon microscopy

This chapter was published as a peer-reviewed paper in the *Optics Express* journal by the *Optical Society of America* in 2021 [127].
The authors are Ivan Vishniakou and Johannes D. Seelig.
https://doi.org/10.1364/OE.424344

4.1 Introduction

Using adaptive optics for imaging in aberrating samples requires finding appropriate corrections, which can be determined using wavefront sensors [128, 129, 130, 136]. Alternatively, a variety of so-called sensorless approaches, that don't require a wavefront sensor, have been developed. One class of algorithms takes advantage of optimization. For example, iteratively modulating and updating an excitation wavefront depending on the resulting fluorescence intensity can be used for finding aberration corrections [164, 130].

Other approaches for adaptive optics additionally take advantage of prior information about the optical system by including system information in a computational model [148, 165, 166, 149, 124, 150, 151]. In this case, optimization can be used for finding aberrations which enter the model as undetermined parameters. Different from the above mentioned optimization approaches, all data is already provided at the beginning of the optimization process and not recorded iteratively [150].

More recently, the development of machine learning frameworks such as Tensorflow has enabled optimizing computationally demanding models in many areas of physics and

engineering (for example [99, 167, 111, 168, 123, 121, 122, 120]) and also in optical imaging [123, 126, 152].

This approach can be applied for adaptive optics [126]. Using a differentiable model of the optical system, focusing in transmission through a single aberrating layer as well as in a reflection, epidetection configuration through two aberrating layers was achieved [126]. Here, we extend this differentiable model-based adaptive optics method to scanning two-photon microscopy with a high numerical aperture objective as used for *in vivo* imaging in brain tissue.

For this, a fluorescent guide star in an aberrated sample is probed with a small number of excitation modulations. The resulting dataset of pairs of excitation modulations and guide star images is sufficient for constraining model optimization in Tensorflow. This approach allows including detailed setup information in the optimization process and finds corrections independent of prior assumptions about the statistics of aberrations. We show experimentally that aberrations in a sample can be determined and corrected.

4.2 Differentiable model-based approach for adaptive optics

Modern machine learning frameworks efficiently implement model training by gradient based minimization of a loss function describing the mismatch between the output of a model and a target. They provide gradient-based optimizers and an automatic differentiation [156] framework, which leaves for the user only the task of implementing the desired model and loss function using a composition of differentiable functions. Here, we implement a model that simulates two-photon image formation in a scanning microscope depending on a set of free parameters which correspond to the sample aberration and are found through optimization (Fig. 4.1). An advantage of this approach is also the efficient implementation of optimization and model evaluation on a GPU, for example in Tensorflow, which was used here.

This approach is schematically illustrated in Fig. 4.1. First, a computational model is fitted to the two-photon microscope. This model accurately describes propagation of the laser beam through the microscope, including the spatial light modulator and the high numerical aperture objective, as well as image formation with the detected fluorescence. Then, aberrations are found by optimizing free model parameters corresponding to the undetermined sample aberrations (see Fig. 4.1 for details).

4.3 Setup and image preprocessing

The setup is schematically shown in Fig. 4.1. A custom built two-photon scanning microscope was used with components similar to the one described in [125]. A laser beam (920 nm, Chameleon Discovery, Coherent) was expanded and reflected off a spatial light modulator (Meadowlark, HSP1920-1064-HSP8). The spatial light modulator was imaged onto the resonant scanning mirror with a pair of lenses. The scanning mirrors were imaged into the back focal plane of the objective and fluorescence was detected with a dichroic mirror and a lens focusing detected light onto a photomultiplier tube (Hamamatsu, H7422PA-40) using photon counting. The same excitation and fluorescence detection arrangement was used as described in [125], however, with a different objective (Nikon CFI Apo 60X W NIR, N.A. 1.0, 2.8 mm W.D.) and correspondingly adjusted tube and scan lenses (all lenses used in the setup were achromatic doublets from Thorlabs). The microscope was controlled with Scanimage [44] which was integrated with custom software written in Python for SLM control and for synchronizing probing modulations with image acquisition using Scanimage API callbacks.

Fluorescence images were recorded using photon counting at 512×512 pixels resolution at 30 Hz. This resulted in sparse images with low counts of photons per pixel, with many discontinuities (gaps) in intensities hindering the correct estimation of the similarity with model output. Therefore all fluorescence images were preprocessed with a low-pass filter: a discrete Fourier transform was applied to the images and frequencies exceeding 0.15 of the pattern resolution were discarded before inverse transformation. Examples of images before and after preprocessing are shown in Fig. 4.2 (columns two and three, respectively).

4.4 Computational modeling and optimization

4.4.1 Computational model of the optical setup

To implement differentiable model-based adaptive optics for two-photon microscopy, first a differentiable model of the setup needs to be established. The main elements of the setup model are illustrated in Fig. 4.1, right side. The model consists of, first, a phase modulation describing the spatial light modulator (SLM), second, a phase function describing the focusing objective, and, third, a (unknown) sample phase aberration. The optimization process is schematically illustrated in Fig. 4.1 (see figure legend for details).

The computational model is based on Fourier optics. Light propagation along the optical axis (z-axis; x, y, z are spatial coordinates) is represented as a complex amplitude $U(x,y,z)$. The wavefront propagates in free space and through a sequence of planar phase objects along the optical axis. The interaction of the wavefront $U(x,y,d)$ with a phase object $\phi(x,y,d)$ at plane d is described as a multiplication:

$$U(x,y,d)\cdot\exp\left[i\phi(x,y,d)\right]. \tag{4.1}$$

Free space propagation of the wavefront over a distance d is calculated using the angular spectrum method with the following operator [5]:

$$\begin{aligned} U(x,y,z+d) = P_d(U(x,y,z)) = \iint A(f_x,f_y;z)\,\mathrm{circ}\left(\sqrt{(\lambda f_X)^2+(\lambda f_Y)^2}\right) \\ \times H\exp\left[i2\pi(f_X x+f_Y y)\right]\mathrm{d}f_X\,\mathrm{d}f_Y. \end{aligned} \tag{4.2}$$

Here, $A(f_X,f_Y;z)$ is the Fourier transform of $U(x,y,z)$, f_X and f_Y are spatial frequencies, the circ function is 1 inside the circle with the radius in the argument and 0 outside [5], and $H(f_X,f_Y)=\exp\left[i2\pi\frac{d}{\lambda}\sqrt{1-(\lambda f_X)^2-(\lambda f_Y)^2}\right]$ is the optical transfer function. Light intensity as measured at the sensor is given by

$$I(x,y,z)=\left|U(x,y,z)\right|^2. \tag{4.3}$$

For two-photon imaging [41] the induced fluorescence intensity is proportional to the square of the excitation intensity:

$$I_\mathrm{f}\propto I^2=\left|U\right|^4. \tag{4.4}$$

Using these equations, the image of a fluorescent bead in the microscope (or the PSF) is simulated with the following function, taking into account that the propagating wavefront is modulated by the SLM and phase aberration of the sample:

$$I_\mathrm{f}=S(\phi_\mathrm{SLM},\phi_\mathrm{aberration})=\left|P_{f_\mathrm{MO}}(U_0\cdot\exp\left[i(\phi_\mathrm{SLM}+\phi_\mathrm{MO}+\phi_\mathrm{aberration})\right])\right|^4, \tag{4.5}$$

where ϕ_SLM is the SLM phase modulation, $\phi_\mathrm{aberration}$ is the phase surface of the aberration,

U_0 is the beam cross-section (complex) amplitude, and f_{MO} and ϕ_{MO} are the focal length and the corresponding phase modulation of the microscope objective, respectively. The SLM modulation is modelled directly at the same z-plane as the objective, which allows omitting nonessential computations, since it is imaged onto the back focal plane of the microscope objective. The aberration is also modelled at the same plane, saving computations and simplifying the correction: since the phase function of the aberration is found at the SLM plane, its inverse can be directly applied to the SLM without any additional computations of propagation between different planes.

4.4.2 Fitting the computational model to the experimental setup

The goal of the optimization process is matching the computational model to experimental observations with correlations as a similarity measure. The model images therefore have to match in each pixel with the images observed in the microscope in the absence of sample aberrations. When responses to probing SLM modulations are measured under these aberration-free conditions, model optimization is expected to yield a flat aberration. Optimization without sample aberrations therefore can be used for validating the correspondence between the model and the microscope. The model equation (4.5) contains fixed parameters U_0 (Gaussian amplitude profile with flat phase, $\sigma = 2.85$ mm), $\lambda = 920$ nm, $f_{\mathrm{MO}} = 1700$ mm, and corresponding ϕ_{MO} which were matched to the experimental setup by taking into account pupil sizes $d = 4.0$ mm, field of view size ($60 \times 40 \mu$m at zoom level 10), and the resolution of imaging and simulation (512×512 pixels). Significant elongation of f_{MO} allows approximate lateral upscaling of simulated images for matching the microscope zoom level without resampling of the angular spectrum. Additionally, minor rotational misalignments of the SLM in the image plane were observed and adjusted for by corresponding counter-rotations of the recorded fluorescence images, since such rotations could not be corrected by adjusting the SLM phase. A fixed zoom level and field of view were used for all experiments and the model was adjusted for these conditions. The parameters were tuned in the following procedure: first, a sparse aberration-free fluorescent guide star (1 μm diameter fluorescent beads embedded in 3 % agarose) was imaged under various modulations (Zernike modes Z1 through Z10 displayed one-by-one with alternating magnitudes). The parameters were then manually tuned to closely match computed to actual images. For this, zoom level and SLM orientation were varied while displaying a set of different SLM phase modulations. This procedure needed only to be done once

and was therefore performed manually, but a computational optimization would also be possible. The resulting model was validated by running the model optimization for finding corrections in the absence of introduced sample aberrations. After successful parameter optimization, the residual aberrations of the system were close to zero, indicating that the computational model accurately described the experimental microscope setup. As shown in Fig. 4.2, after tuning of the model parameters, good correspondence between experimentally observed and computationally generated patterns was achieved (shown here after optimization in an aberrating sample, see below).

4.4.3 Model optimization and loss function

Sample aberrations introduce an unknown phase function into the optical setup. To mirror this situation computationally, a phase surface is added as a set of free parameters to the model [126]. This unknown phase surface needs to be adjusted through optimization in such a way that it describes the introduced sample aberration. After successful optimization, the aberration phase surface is known, as verified by the model again matching the optical setup (Fig. 4.2), and can therefore be corrected.

We found that optimization with a single image of the fluorescent bead and corresponding single SLM phase modulation did often not result in satisfactory results since multiple possible phase modulations can generate similar planar PSF images. To constrain the optimization process, we therefore probed the guide star with a set of different excitation modulations as in [126] by displaying randomly generated phase patterns on the SLM and imaging the resulting changes in the aberrated guide star.

In total, 20 such pairs of SLM phase aberrations and corresponding two-photon images served as the input to the computational model. Images were recorded using photon counting at a frame rate of 30 Hz. (The SLM has a maximum frame rate of more than 500 Hz, but the control loop implemented here ran only at 2 Hz since SLM and image acquisition were not closely integrated.) Probing phase modulations were generated by summing Zernike modes Z1 through Z10 with coefficients drawn form a uniform random distribution in the range of -1 to 1 and were displayed on the SLM while corresponding fluorescence images I_f were recorded.

The unknown aberration phase function was then found in an optimization process

with the goal of matching measured and simulated images:

$$\underset{\phi_{\text{aberration}}}{\arg\min} \sum_{j=1}^{N} \text{loss}(S(\phi_{\text{SLM}_j}, \phi_{\text{aberration}}), I_{\text{f}_j}). \tag{4.6}$$

Here, SLM_j and $\phi_{\text{aberration}_j}$ are pairs of SLM probing modulations and corresponding fluorescence images recorded in the two-photon microscope. S is the microscope model as specified in (4.5). The loss function is defined to reflect the similarity between simulated and measured fluorescent images:

$$\text{loss}(\text{prediction}, \text{target}) = -r\,[\text{prediction}, \text{target}] \cdot \ln\Big(\sum^{\text{pixels}} |\text{prediction}|\Big), \tag{4.7}$$

where $r\,[\text{prediction}, \text{target}]$ is Pearson's correlation coefficient, and $\ln\left(\sum^{\text{pixels}} |\text{prediction}|\right)$ is an additional cost factor for light intensity conservation. Since Pearson's correlation coefficient is not sensitive to the magnitude of the prediction, the optimizer likely converges to a solution which provides high correlation, but discards some of the light by redirecting it out of the field of view, and therefore usually does not result in good corrections. Therefore, additionally introducing the sum of the total intensity promotes solutions that do not discard excitation intensity. The logarithm ensures that the slope of this regularization factor is always smaller than that of the correlation coefficient, making it a secondary optimization goal.

The model (4.5) was implemented using Tensorflow 2.4 [85], adapting the angular spectrum method from [144] and using the optimization algorithm Adam with a learning rate of 0.01. According to expression (4.5), the phase $\phi_{\text{aberration}}$ is represented as a real-valued tensor, which is a requirement for optimization variables in Tensorflow. All modulations and sample responses were packed in a single batch and used all at once in each of the optimizer's iterations. 1000 optimization steps were typically sufficient for reaching a correlation coefficient between model and observations of > 0.9. The optimization took between 1 and 2 minutes on a workstation with four Nvidia Titan RTX GPUs used in data parallel mode. The optimization was terminated when the correlation coefficient between computational model and experimental data plateaued. The resulting aberration phase function was negated (multiplied by -1) for displaying on the SLM and in this way results in the correction of the aberration.

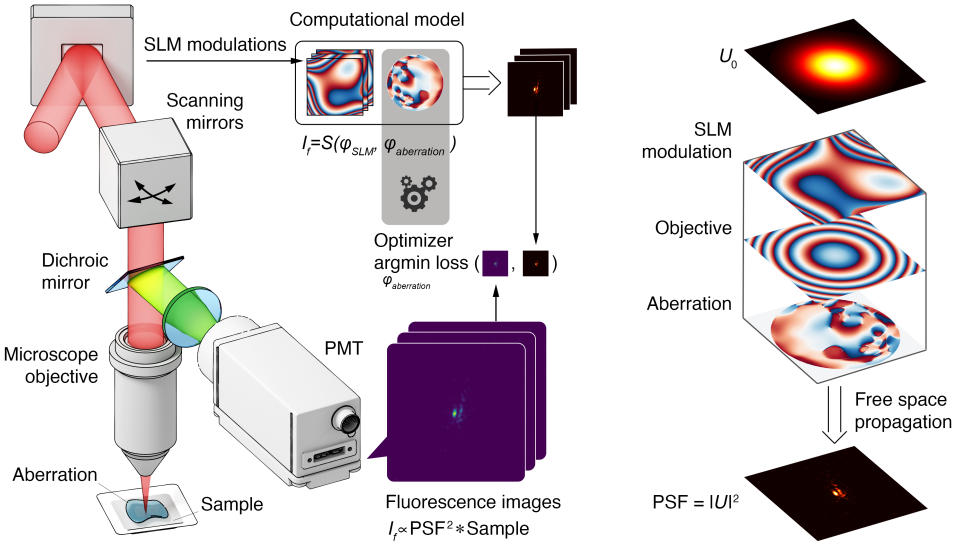

Figure 4.1: Left: Schematic of the two-photon microscope and corresponding model optimization. A laser beam is scanned with scanning mirrors and focused through an objective. Fluorescence light is collected with a dichroic mirror onto a photomultiplier tube. A computational model is set up to describe the microscope in the absence of aberrations. After introducing aberrations, the computational model receives phase modulations displayed on the SLM as input. The model output is a set of point spread function (PSF) images that are compared with experimentally recorded PSF images through the loss function. The optimizer (running in Tensorflow on a GPU) finds a sample aberration (and corresponding correction) by matching of the model output with experimental PSF images. Right: The computational model is formulated in expression (4.5). The beam cross-section, represented as a complex amplitude, is multiplied by phase objects representing SLM probing modulation, objective, and aberration, respectively, and is propagated to the focal plane of the objective using the angular spectrum method to calculate the resulting PSF. The two-photon image is the convolution of the squared PSF intensity and the object function, resulting in just the point spread function squared for a guide star. The beam profile U_0 and objective parameters are adjusted to describe the experimental setup. The SLM modulation is the model input, the PSF is the model output, the aberration is found through optimization.

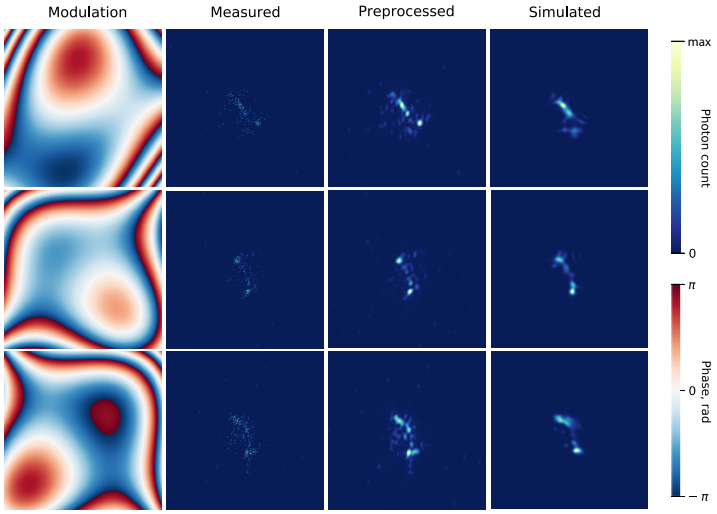

Figure 4.2: Correspondence between computationally generated and experimentally measured images of fluorescent beads. Three representative examples (rows), recorded in an aberrating sample: probing modulations displayed on SLM (first column), and corresponding PSF images as measured with photon counting (second column), preprocessed for model fitting (third column) and simulated with the optimized model. Field of view size is $40 \times 40\mu$m.

4.5 Two-photon imaging through aberrations

To test the approach experimentally, a sample aberration was introduced by covering the fluorescent beads with a layer of vacuum grease on a microscope cover slide. For correcting the induced aberrations, images were taken with a single guide star at the center of a field of view with dimensions of $60 \times 40\mu$m.

Two representative results are shown in Fig. 4.3. Three orthogonal maximum intensity projections, before and after correction, of a fluorescent bead recorded in a volume with axial step size of 0.25 μm between planes are displayed. The third and sixth rows show the improved intensity profiles along representative cross-sections through the fluorescent bead in lateral and axial directions, respectively. Corrections resulted in an increase in intensity and an improved focus with a full width at half maximum (FWHM) after correction of 0.9μm for both samples, and an axial FWHM of 14μm and 5.2μm, respectively (measured with a 1μm diameter bead). The intensity profiles before correction could not be fitted with Gaussians. The slices at the focal plane (at maximum intensity) were averaged over four frames (axially spaced by 0.25μm). Axial profiles were averaged over 3×3 pixels around the center of the focus (maximum intensity) and averaged over the lateral dimensions.

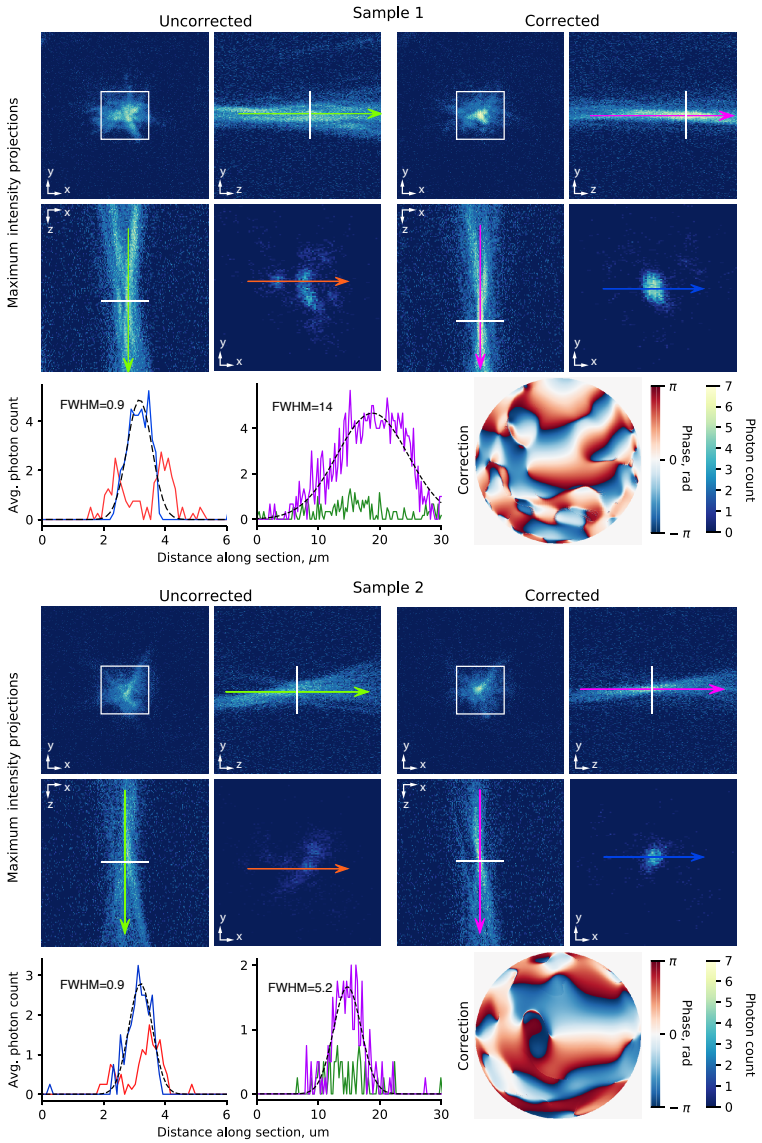

Figure 4.3: Two representative examples of two-photon volume images of a 1μm diameter fluorescent bead embedded in agarose before and after correction. Sample 1, top row, left: Maximum intensity projection of volume image of a fluorescent bead in axial (z) direction (see bottom row for color bar). Projections along x- and y-axes are shown to the right (first row, left center) and below (second row, left). Second row, left center: slice at maximum intensity, indicated by white lines in x- and y-projections averaged over 4 frames recorded with 0.25μm axial spacing. Image is zoomed-in as indicated by white box in top left image, size is $10 \times 10\mu$m. Top row, center right: same as left side after correction, again with corresponding x- and y- projections. Second row, right: slice at maximum intensity, indicated by white lines in x- and y-projections averaged over 4 frames recorded with 0.25μm axial spacing after correction. Third row, left: lateral cross-sections before and after correction as indicated by correspondingly colored arrows in row two, including Gaussian fit of corrected profile (black dashed line). Third row, center: axial cross sections along the correspondingly colored arrows in the second row including Gaussian fit of corrected image. Third row, right: aberration correction. Sample 2: as described for sample 1.

4.6 Discussion and conclusions

We developed a differentiable model-based approach for adaptive optics for two-photon scanning microscopy. The method takes advantage of combining a differentiable model of the known microscope and unknown sample with the optimization techniques implemented in machine learning frameworks [126]. We show that, with an appropriate cost function (equation 4.7), a small number of probing modulations (recorded at high frame rates and with low photon count rates as often observed when imaging *in vivo*) is sufficient for finding sample aberrations through model optimization and to correct them.

Different from optimization approaches that directly aim to optimize focus intensity, the first optimization objective here was matching the focus shape of the model to the one observed in the microscope. However, we added an additional, secondary term to the cost function to also optimize image intensity directly.

A limitation of the current implementation for dynamic samples is the required correction time. Here, we used 20 probing modulations recorded at a frame rate of 30 Hz, thus requiring a minimum of 0.66 seconds for data acquisition. Model optimization took between 1 and 2 minutes, which is ultimately limited by the computational speed of the GPU and could be accelerated with improved or more GPUs.

As seen in Fig. 3.3, the focus after optimization did in particular in axial direction not reach the diffraction limit (as measured with 1 μm diameter fluorescent beads). While such axially extended point spread functions are often used for *in vivo* imaging (see for example [169] for a recent discussion), the quality of the corrections could be improved in several ways. A limitation of the current data, in particular for correcting higher order aberrations, is their limited dynamic range. The dynamic range could for example be extended by combining multiple fluorescence images recorded with different integration times [170]. Additional improvements in performance are expected from using a model approximation that is more accurate for high numerical aperture objectives than the one used here [171]. Together, such improvements will more accurately reflect the physical setup and aberrations and therefore improve optimization results. As an alternative to using multiple modulations recorded in the same focal plane, also axial slices or an entire volume could be used for optimization.

Compared with other optimization approaches that rely on iterative methods, including prior information about the experimental setup additionally constrains the optimization

process [150]. Compared to neural network approaches [87, 90, 138, 92, 172, 141, 93, 147, 125, 173], differentiable model-based approaches have the advantage that they don't rely on a predetermined model of sample aberrations.

Overall, the presented approach, similar to other iterative approaches, can be used for correcting aberrations that are approximately stationary, and is under these conditions compatible with imaging in biological samples.

CHAPTER 5

Conclusion

This thesis presents our work on machine learning methods for wavefront sensing for adaptive optics in laser scanning microscopy. As described in the introduction, this is a challenging problem due to the imaging geometry which hinders direct wavefront sensing without introducing or generating guidestars in some form, which however is often invasive or impractical. The alternative of using backscattered light raises the problem of aberration identification accumulated in the excitation and detection paths.

From a computational imaging point of view, we have a system that produces images conditioned by an unknown aberration. The resulting inverse problem that has to be solved therefore lies in finding this aberration based on the recorded images. Since an analytical inverse solution does not exist, and since the problem might be ill-posed (considering for example that intensity imaging discards phase information), wavefront sensing is challenging.

However, in the absence of an analytical model, deep learning can be applied to establish a mapping between input and output. For this, a neural network is trained on datasets of images and corresponding aberration labels and serves as a proxy of the inverse model. An alternative way to solve the inverse problem is by optimizing the forward model, which in our case exists, since image formation can be mathematically described using Fourier optics. We implemented the forward model with a deep learning framework allowing automatic differentiation to enable its efficient optimization using gradient-based methods.

In the following, we discuss the results of the projects presented in Chapters 2, 3 and 4, as well as their limitations, and make an outlook for future work.

5.1 Limitations and future work

Adaptive optics with reflected light and deep neural networks

We relied on a deep neural network model to recognize aberrations from reflected light distributions imaged in an epidetection configuration. Reflected light provides a much stronger signal source than fluorescence for aberration detection, and was used for both finding excitation corrections with reflective guidestars as well as for separating excitation and detection aberrations with a planar reflective sample.

While the latter planar reflective sample can not be embedded in biological specimens, the developed method for dual-pass corrections could be extended to arbitrary scattering samples in future work. Datasets could be collected for example from tissue phantoms in the same way as described in this thesis and networks could be trained to recognize excitation and detection aberrations under these conditions.

Although the problem of finding two combined aberrations, such as excitation and detection aberration, at the same time can be problematic because of possible self-cancellation of some aberration modes [54], some asymmetry between excitation and detection paths could be beneficial, and is even introduced in some systems by design [174]. A slight asymmetry has been measured in our microscope in a calibration step, and it could be intentionally amplified to improve performance.

Further, one could take advantage of improved methods for wavefront sensing. Reflected focus images vary over a wide range of intensities and are therefore problematic to capture and to use as network input. Intensities can change by several orders of magnitude across a few pixels within one image, and finer details are potentially lost in quantization errors. Therefore, for example distinguishing between two weakly aberrated foci can rely on small intensity variations in only a few pixels. This in turn can be ambiguous and could contribute to overfitting during model training.

To address this issue, such high intensity features could alternatively be transformed and distributed across the whole field of view of the camera by optical preconditioning of the wavefront sensor. In [94] several transformations of the light field before imaging were tried out. A microlens array could be a good candidate for preconditioning (which was for example used in combination with deep learning in [93]), or even a random scatterer, with the purpose of increasing signal variance across more camera pixels. Another advantage of optical preconditioning is that it allows the phase information of the wavefront to be

extracted from a single image, eliminating the need of out-of-focus images (as used in our work described in Chapter 2).

For obtaining corrections we found it useful to diversify the network input by varying the focal plane over a small axial range of the sample. This resulted in slight variations of the confocal volume images, and the aberrations could be inferred by averaging the predictions based on these images. Instead of using mechanical scanning, this input diversification could also be achieved with SLM modulations, which would allow to probe the sample with arbitrary excitation modulations. The deep learning model could therefore be adjusted to accept diversified inputs with a suitable probing strategy.

Another practical problem encountered when using deep learning methods with confocal light images is that the intensity of the images cannot be universally calibrated in the microscope for different specimens. The training dataset was normalized to the maximum intensity of each sample, therefore discarding the relative intensity variations between differently aberrated foci. This situation could be improved by implementing a probing strategy and normalizing the images within a batch of probes, which could carry more information about the PSF than a single image.

Differentiable model-based adaptive optics with transmitted and reflected light

We demonstrated a model-based approach to infer the unknown aberrations of an imaging system through a gradient-based optimization process implemented within a deep learning framework. The imaging system was mathematically modelled, yielding a function that simulates image formation, is differentiable, and contains unknown aberrations as optimization parameters.

A proof-of-concept setup was built based on the geometry of epidetection imaging in a confocal microscope, reproducing the dual-pass problem of backscattered light detection. Our method was able to disentangle the excitation and detection path aberrations and to correct the focus inside the sample based on reflected light only.

While the setup for demonstrating this method recreated the illumination and detection geometry of a laser scanning reflection microscope it also had some important differences: first, the lenses used to focus the light in the sample had low numerical aperture (NA), making it qualitatively different from focusing light with a high NA objective as commonly used for two-photon or confocal imaging. Additionally, we used a mirror as a sample behind the aberrating material (as in the deep learning method presented in Chapter 2).

Lastly, the angular spectrum method used to calculate light propagation relies on the paraxial beam approximation, meaning that the angle of convergence of the beam is shallow and the transverse direction of wave propagation is neglected. For applications with high NA microscope objectives a different model might be needed.

Another challenge was scattered light that did not reach the detector and could therefore not be accounted for by the model, resulting in only partial corrections. This was observed with some more strongly aberrating samples and could be remedied by introducing a non-random sample probing strategy as well as by optimizing the detection path of the microscope to ensure that most of the light is detected.

Differentiable model-based adaptive optics for two-photon microscopy

We adapted the differentiable model-based aberration inference described above for a two-photon microscope with fluorescent guidestars. For this, we modelled image formation in a two-photon microscope conditioned by an aberration which was treated as an optimization variable. The aberrated sample was probed with several phase modulations and the model was matched to observations with gradient-based optimization by altering the aberration parameters. This gradient-based optimization made the process efficient and required only a few samples to converge.

Image formation in the microscope was modelled by calculating propagation of the aberrated wavefront through free space after modulation with the SLM, objective, and (unknown) phase aberration, respectively. Fluorescence images of a guidestar were modelled as the square of the intensity of the resulting PSF, which accounted for the two-photon process. The angular spectrum method was used for this, and the simulation parameters (resolution, geometry) were fitted to match the model's output to images of the unaberrated microscope with pixel-to-pixel precision.

This however presented a challenge, since modelling a focused beam can become computationally expensive, especially when a high-NA objective is used. First, the focal region is discretized with a specified resolution. Then, in every point of that grid all the complex amplitudes of the source angular spectrum are integrated with their corresponding amplitude and phase offsets that are accumulated over their respective paths of propagation. Naïve computation of that integral is inefficient, so we used the angular spectrum method together with two-dimensional FFT. This however imposes limitations on the input and output resolution of the model, because of the algorithm's constraints: FFT calculates the

transform at the same resolution as the input, making it impossible to sample the focal region at an arbitrary desired resolution, and in order to increase the sample density, zero padding of the input has to be used. On the other hand the k-space (angular spectrum) is typically populated very sparsely, with only a small low spatial frequency band being used, and additional zero padding would only make the situation worse. To remedy that, a different algorithm for the angular spectrum integration could be used that allows to change the resolution of the output, such as non-uniform fast Fourier transform or chirp-z transform [175]. One has to be careful with selecting the resolutions of the pupil and focal planes to make sure that aliasing errors do not appear due to undersampling. Additionally, for high NA objectives a more suitable modelling approach would be the Debye-Wolf integral using a vectorial electric field model, that is, taking light polarization into account [176]. Nevertheless, the simpler model used here could be accurately fitted to the setup and could be used to find corrections.

5.2 Discussion and outlook

In this thesis we introduced two novel approaches for aberration correction suitable for two-photon fluorescence microscopy. The first method, based on deep-learning, is fast at predicting corrections. However, as with any neural network, the resulting model is constrained by the training dataset to a limited range of predicted corrections. The second method, which relies on optimization, does not have this limitation, but comes at the cost of requiring additional computations and therefore slower correction speeds. Both approaches address the same problem from different perspective and both have their own advantages and disadvantages.

Some improvements could be introduced that would benefit both methods. The deep learning method could be extended to take advantage of the SLM located in the excitation path to probe the sample and take several measurements as input. This is reminiscent of tomographic approaches for reconstructing a sample, or in this case an aberration. For example in [177] a recurrent neural network is designed to take a sequence of projection images to reconstruct the volume of a sample.

The differentiable model could be further improved for a high-NA objective calculation by using the vectorial Debye-Wolf integral. This computation is rather slow even with GPU acceleration, and therefore a more efficient integration algorithm should be used. Currently, the computational cost of extending the model to also include a reflected light

path is prohibitive.

The current implementation of the differentiable models relies on reconstructing the PSF of the system conditioned on aberrations, which requires imaging of a guidestar. While fluorescent guidestars are routinely used in biological imaging, a more flexible approach without guidestars could be envisioned. Image formation with arbitrary objects could be simulated (using the convolution of the unknown PSF and the unknown object function), and both, the PSF as well as the object function could be free parameters for differentiable optimization.

Both, the neural network and the optimization approach, could be combined to complement each other to improve correction results, and a seamless integration is possible since both rely on the same algorithmic framework. For example, adding a deep prior could improve optimization performance of the differentiable forward model: a pretrained neural network could serve as deep prior and provide initial estimates of aberrations. These estimates could then be refined in the differentiable model. This could reduce the number of iterations required for optimization and the differentiable model would at the same time refine and improve the neural network solution, therefore allowing corrections beyond those included in the training dataset.

A different combination of the (known) forward model and the inverse model acquired through training could also be implemented. Both models could be combined and the inverse model could be learned with synthetic data, using the forward model as a generator of PSF images that are then fed directly into the trainable inverse model. In this way, one could avoid creating a labelled dataset with the setup, at least for imaging with guidestars which do not depend on the sample properties. An approach similar to this one was implemented in a paper that appeared shortly after our deep learning publication [173], however using a model that was not optimized for a specific setup and included only low order aberrations. Such a self-supervised learning loop can also be utilized to optimize probing strategies to detect aberrations, like in [123].

The developed approaches for detecting two aberrations at the same time, either using deep neural networks or using model optimization, could also be applied for multi-conjugate adaptive optics. Using these methods for finding corrections at the same time in multiple layers would potentially allow to compensate for more strongly aberrating samples.

Finally, in this thesis, we only considered two-dimensional images, which is a common approximation in adaptive optics [64, 178]. However, biological samples typically vary similarly in all three dimensions, and therefore the common assumption that all corrections occur within the same focal plane, as also used in our model, is a limitation. Therefore, in the future it will be important to extend the approaches developed here by taking into account three-dimensional focal distributions and samples.

References

[1] Charles Jr Seymour. Dark chamber and light-filled room: Vermeer and the camera obscura. *The Art Bulletin*, 46(3):323–331, 1964.

[2] Edward G Steward. *Fourier optics: an introduction*. Courier Corporation, 2004.

[3] Mina R Bionta, Felix Ritzkowsky, Marco Turchetti, Yujia Yang, Dario Cattozzo Mor, William P Putnam, Franz X Kärtner, Karl K Berggren, and Phillip D Keathley. On-chip sampling of optical fields with attosecond resolution. *Nature Photonics*, 15(6):456–460, 2021.

[4] Bahaa E A Saleh and Malvin Carl Teich. *Fundamentals of photonics*. John Wiley & Sons Inc, 2019.

[5] Joseph W Goodman. *Introduction to Fourier optics, 3rd ed.* Roberts and Company Publishers, 2005.

[6] Max Born and Emil Wolf. *Principles of optics: electromagnetic theory of propagation, interference and diffraction of light*. Elsevier, 2013.

[7] David L Fried. Varieties of isoplanatism. In *Imaging through the Atmosphere*, volume 75, pages 20–29. International Society for Optics and Photonics, 1976.

[8] Stephane Perrin and Paul Montgomery. Fourier optics: basic concepts. *arXiv preprint arXiv:1802.07161*, 2018.

[9] Eva Rittweger, Kyu Young Han, Scott E Irvine, Christian Eggeling, and Stefan W Hell. Sted microscopy reveals crystal colour centres with nanometric resolution. *Nature Photonics*, 3(3):144–147, 2009.

[10] Michael J Rust, Mark Bates, and Xiaowei Zhuang. Sub-diffraction-limit imaging by stochastic optical reconstruction microscopy (storm). *Nature methods*, 3(10):793–796, 2006.

[11] Mats GL Gustafsson. Surpassing the lateral resolution limit by a factor of two using structured illumination microscopy. *Journal of microscopy*, 198(2):82–87, 2000.

[12] Dieter W Pohl, Winfried Denk, and Mark Lanz. Optical stethoscopy: Image recording with resolution $\lambda/20$. *Applied physics letters*, 44(7):651–653, 1984.

[13] Henry C King. The invention and early development of the achromatic telescope. *Popular Astronomy*, 56:75, 1948.

[14] Robert B Leighton. Concerning the problem of making sharper photographs of the planets. *Scientific American*, 194(6):157–166, 1956.

[15] John W Hardy. Adaptive optics. *Scientific American*, 270(6):60–65, 1994.

[16] James C Wyant. Use of an ac heterodyne lateral shear interferometer with real–time wavefront correction systems. *Applied optics*, 14(11):2622–2626, 1975.

[17] Robert Tyson. *Adaptive optics engineering handbook*, volume 67. CRC Press, 1999.

[18] Enrico Marchetti, Roland Brast, Bernard Delabre, Robert Donaldson, Enrico Fedrigo, Christoph Frank, Norbert Hubin, Johann Kolb, Jean-Louis Lizon, Massimiliano Marchesi, et al. On-sky testing of the multi-conjugate adaptive optics demonstrator. *The Messenger*, 129(8), 2007.

[19] Cardinal Warde, James T McCann, Vern Shrauger, H-H Ieong, Ali Ersen, XY Wang, and J Hubbard. Membrane mirror light modulator technology. In *Diffractive/Holographic Technologies and Spatial Light Modulators VII*, volume 3951, pages 191–199. International Society for Optics and Photonics, 2000.

[20] Rüdiger Paschotta. Article on deformable mirrors in the rp photonics encyclopedia. `https://www.rp-photonics.com/deformable_mirrors.html`. Accessed: 2021-09-30.

[21] Dana Dudley, Walter M Duncan, and John Slaughter. Emerging digital micromirror device (dmd) applications. In *MOEMS display and imaging systems*, volume 4985, pages 14–25. International Society for Optics and Photonics, 2003.

[22] David Dayton, John Gonglewski, Sergio Restaino, Jeffrey Martin, James Phillips, Mary Hartman, Stephen Browne, Paul Kervin, Joshua Snodgrass, Nevin Heimann, et al. Demonstration of new technology mems and liquid crystal adaptive optics on bright astronomical objects and satellites. *Optics Express*, 10(25):1508–1519, 2002.

[23] Kaustubh Banerjee, Pouya Rajaeipour, Çağlar Ataman, and Hans Zappe. Optofluidic adaptive optics. *Applied optics*, 57(22):6338–6344, 2018.

[24] Sebastianus A Goorden, Jacopo Bertolotti, and Allard P Mosk. Superpixel-based spatial amplitude and phase modulation using a digital micromirror device. *Optics express*, 22(15):17999–18009, 2014.

[25] James M Florence and Richard D Juday. Full-complex spatial filtering with a phase mostly dmd. In *Wave Propagation and Scattering in Varied Media II*, volume 1558, pages 487–498. International Society for Optics and Photonics, 1991.

[26] Vincent Bagnoud and Jonathan D Zuegel. Independent phase and amplitude control of a laser beam by use of a single-phase-only spatial light modulator. *Optics letters*, 29(3):295–297, 2004.

[27] Adrián Peña and Mikkel F Andersen. Complete polarization and phase control with a single spatial light modulator for the generation of complex light fields. *Laser Physics*, 28(7):076201, 2018.

[28] Kevin J Mitchell, Sergey Turtaev, Miles J Padgett, Tomáš Čižmár, and David B Phillips. High-speed spatial control of the intensity, phase and polarisation of vector beams using a digital micro-mirror device. *Optics express*, 24(25):29269–29282, 2016.

[29] Lars Erdmann, Arnaud Deparnay, Gunter Maschke, Mario Längle, and Robert Brunner. Moems-based lithography for the fabrication of micro-optical components. *Journal of Micro/Nanolithography, MEMS, and MOEMS*, 4(4):041601, 2005.

[30] Patrick S Salter and Martin J Booth. Adaptive optics in laser processing. *Light: Science & Applications*, 8(1):1–16, 2019.

[31] M Hatzenbichler, M Geppert, R Seemann, and J Stampfl. Additive manufacturing of photopolymers using the texas instruments dlp lightcrafter. In *Emerging Digital Micromirror Device Based Systems and Applications V*, volume 8618, page 86180A. International Society for Optics and Photonics, 2013.

[32] René Lynge Eriksen, Vincent Ricardo Daria, and Jesper Glückstad. Fully dynamic multiple-beam optical tweezers. *Optics Express*, 10(14):597–602, 2002.

[33] William J Dallas. Computer-generated holograms. In *Digital holography and three-dimensional display*, pages 1–49. Springer, 2006.

[34] Andrew M Weiner. Femtosecond pulse shaping using spatial light modulators. *Review of scientific instruments*, 71(5):1929–1960, 2000.

[35] Marvin Minsky. Memoir on inventing the confocal scanning microscope. *Scanning*, 10(4):128–138, 1988.

[36] Marvin Minsky. Microscopy apparatus us patent 3013467. *USP Office, Ed. US*, 1961.

[37] Paul Davidovits and M David Egger. Scanning laser microscope. *Nature*, 223(5208):831–831, 1969.

[38] Harekrushna Sahoo. Fluorescent labeling techniques in biomolecules: a flashback. *Rsc Advances*, 2(18):7017–7029, 2012.

[39] Kurt Thorn. Genetically encoded fluorescent tags. *Molecular biology of the cell*, 28(7):848–857, 2017.

[40] Junichi Nakai, Masamichi Ohkura, and Keiji Imoto. A high signal-to-noise ca 2+ probe composed of a single green fluorescent protein. *Nature biotechnology*, 19(2):137–141, 2001.

[41] Winfried Denk, James H Strickler, and Watt W Webb. Two-photon laser scanning fluorescence microscopy. *Science*, 248(4951):73–76, 1990.

[42] Chris Xu, Warren Zipfel, Jason B Shear, Rebecca M Williams, and Watt W Webb. Multiphoton fluorescence excitation: new spectral windows for biological nonlinear microscopy. *Proceedings of the National Academy of Sciences*, 93(20):10763–10768, 1996.

[43] Emily C Rothstein, Michael Nauman, Scott Chesnick, and Robert S Balaban. Multiphoton excitation microscopy in intact animals. *Journal of microscopy*, 222(1):58–64, 2006.

[44] Thomas A Pologruto, Bernardo L Sabatini, and Karel Svoboda. ScanImage: flexible software for operating laser scanning microscopes. *Biomedical engineering online*, 2(1):13, 2003.

[45] David L. Fried. Statistics of a geometric representation of wavefront distortion. *JoSA*, 55(11):1427–1435, 1965.

[46] Bernard Roelof Andries Nijboer. The diffraction theory of optical aberrations: Part ii: Diffraction pattern in the presence of small aberrations. *Physica*, 13(10):605–620, 1947.

[47] Vasudevan Lakshminarayanan and Andre Fleck. Zernike polynomials: a guide. *Journal of Modern Optics*, 58(7):545–561, 2011.

[48] Berge Tatian. Aberration balancing in rotationally symmetric lenses. *JOSA*, 64(8):1083–1091, 1974.

[49] Cosmas Mafusire and Tjaart PJ Krüger. Strehl ratio and amplitude-weighted generalized orthonormal zernike-based polynomials. *Applied optics*, 56(8):2336–2345, 2017.

[50] Robert J Noll. Zernike polynomials and atmospheric turbulence. *JOsA*, 66(3):207–211, 1976.

[51] Ben C Platt and Roland Shack. History and principles of shack-hartmann wavefront sensing, 2001.

[52] HW Friedman. Sodium-layer laser guide stars. Technical report, Lawrence Livermore National Lab., CA (United States), 1993.

[53] Q Hu, J Wang, J Antonello, M Hailstone, M Wincott, R Turcotte, D Gala, and MJ Booth. A universal framework for microscope sensorless adaptive optics: Generalized aberration representations. *APL Photonics*, 5(10):100801, 2020.

[54] Martin J Booth. Adaptive optics in microscopy. *Optical and Digital Image Processing: Fundamentals and Applications*, pages 295–322, 2011.

[55] L Sherman, JY Ye, O Albert, and TB Norris. Adaptive correction of depth-induced aberrations in multiphoton scanning microscopy using a deformable mirror. *Journal of microscopy*, 206(1):65–71, 2002.

[56] O Albert, L Sherman, G Mourou, TB Norris, and G Vdovin. Smart microscope: an adaptive optics learning system for aberration correction in multiphoton confocal microscopy. *Optics letters*, 25(1):52–54, 2000.

[57] P N Marsh, D Burns, and J M Girkin. Practical implementation of adaptive optics in multiphoton microscopy. *Optics express*, 11(10):1123–1130, 2003.

[58] Amanda J Wright, David Burns, Brett A Patterson, Simon P Poland, Gareth J Valentine, and John M Girkin. Exploration of the optimisation algorithms used in the implementation of adaptive optics in confocal and multiphoton microscopy. *Microscopy Research and Technique*, 67(1):36–44, 2005.

[59] Delphine Débarre, Martin J Booth, and Tony Wilson. Image based adaptive optics through optimisation of low spatial frequencies. *Optics Express*, 15(13):8176–8190, 2007.

[60] Martin J Booth, Mark AA Neil, and Tony Wilson. Aberration correction for confocal imaging in refractive-index-mismatched media. *Journal of microscopy*, 192(2):90–98, 1998.

[61] Martin J Booth, Mark AA Neil, Rimas Juškaitis, and Tony Wilson. Adaptive aberration correction in a confocal microscope. *Proceedings of the National Academy of Sciences*, 99(9):5788–5792, 2002.

[62] Daniel E Milkie, Eric Betzig, and Na Ji. Pupil-segmentation-based adaptive optical microscopy with full-pupil illumination. *Optics letters*, 36(21):4206–4208, 2011.

[63] Martin J Booth. Wave front sensor-less adaptive optics: a model-based approach using sphere packings. *Optics express*, 14(4):1339–1352, 2006.

[64] Delphine Débarre, Edward J Botcherby, Tomoko Watanabe, Shankar Srinivas, Martin J Booth, and Tony Wilson. Image-based adaptive optics for two-photon microscopy. *Optics letters*, 34(16):2495–2497, 2009.

[65] Oscar Azucena, Justin Crest, Jian Cao, William Sullivan, Peter Kner, Donald Gavel, Daren Dillon, Scot Olivier, and Joel Kubby. Wavefront aberration measurements and corrections through thick tissue using fluorescent microsphere reference beacons. *Optics express*, 18(16):17521–17532, 2010.

[66] Oscar Azucena, Justin Crest, Shaila Kotadia, William Sullivan, Xiaodong Tao, Marc Reinig, Donald Gavel, Scot Olivier, and Joel Kubby. Adaptive optics wide-field microscopy using direct wavefront sensing. *Optics letters*, 36(6):825–827, 2011.

[67] Xiaodong Tao, Bautista Fernandez, Oscar Azucena, Min Fu, Denise Garcia, Yi Zuo, Diana C Chen, and Joel Kubby. Adaptive optics confocal microscopy using direct wavefront sensing. *Optics letters*, 36(7):1062–1064, 2011.

[68] Rodrigo Aviles-Espinosa, Jordi Andilla, Rafael Porcar-Guezenec, Omar E. Olarte, Marta Nieto, Xavier Levecq, David Artigas, and Pablo Loza-Alvarez. Measurement and correction of in vivo sample aberrations employing a nonlinear guide-star in two-photon excited fluorescence microscopy. *Biomedical Optics Express*, 2(11):3135, 2011.

[69] Xiaodong Tao, Oscar Azucena, Min Fu, Yi Zuo, Diana C Chen, and Joel Kubby. Adaptive optics microscopy with direct wavefront sensing using fluorescent protein guide stars. *Optics letters*, 36(17):3389–3391, 2011.

[70] Marcus Feierabend, Markus Rückel, and Winfried Denk. Coherence-gated wave-front sensing in strongly scattering samples. *Optics letters*, 29(19):2255–2257, 2004.

[71] Markus Rueckel, Julia A Mack-Bucher, and Winfried Denk. Adaptive wavefront correction in two-photon microscopy using coherence-gated wavefront sensing. *Proceedings of the National Academy of Sciences*, 103(46):17137–17142, 2006.

[72] Markus Rueckel and Winfried Denk. Coherence-gated wavefront sensing using a virtual shack-hartmann sensor. In *Advanced Wavefront Control: Methods, Devices, and Applications IV*, volume 6306, page 63060H. International Society for Optics and Photonics, 2006.

[73] Saad A Rahman and Martin J Booth. Direct wavefront sensing in adaptive optical microscopy using backscattered light. *Applied optics*, 52(22):5523–5532, 2013.

[74] Frank Rosenblatt. *The perceptron, a perceiving and recognizing automaton*. Cornell Aeronautical Laboratory, 1957.

[75] Marvin Minsky and Seymour A Papert. Perceptrons, 1969.

[76] George Cybenko. Approximation by superpositions of a sigmoidal function. *Mathematics of control, signals and systems*, 2(4):303–314, 1989.

[77] Kurt Hornik, Maxwell Stinchcombe, and Halbert White. Multilayer feedforward networks are universal approximators. *Neural networks*, 2(5):359–366, 1989.

[78] David E Rumelhart, Geoffrey E Hinton, and Ronald J Williams. Learning representations by back-propagating errors. *nature*, 323(6088):533–536, 1986.

[79] Alex Krizhevsky, Ilya Sutskever, and Geoffrey E Hinton. Imagenet classification with deep convolutional neural networks. *Advances in neural information processing systems*, 25:1097–1105, 2012.

[80] Yann LeCun, Léon Bottou, Yoshua Bengio, and Patrick Haffner. Gradient-based learning applied to document recognition. *Proceedings of the IEEE*, 86(11):2278–2324, 1998.

[81] Yann LeCun, Koray Kavukcuoglu, and Clément Farabet. Convolutional networks and applications in vision. In *Proceedings of 2010 IEEE international symposium on circuits and systems*, pages 253–256. IEEE, 2010.

[82] Vinod Nair and Geoffrey E Hinton. Rectified linear units improve restricted boltzmann machines. In *Icml*, 2010.

[83] Geoffrey E Hinton, Nitish Srivastava, Alex Krizhevsky, Ilya Sutskever, and Ruslan R Salakhutdinov. Improving neural networks by preventing co-adaptation of feature detectors. *arXiv preprint arXiv:1207.0580*, 2012.

[84] Rajat Raina, Anand Madhavan, and Andrew Y Ng. Large-scale deep unsupervised learning using graphics processors. In *Proceedings of the 26th annual international conference on machine learning*, pages 873–880, 2009.

[85] Martín Abadi, Ashish Agarwal, Paul Barham, Eugene Brevdo, Zhifeng Chen, Craig Citro, Greg S. Corrado, Andy Davis, Jeffrey Dean, Matthieu Devin, Sanjay Ghemawat, Ian Goodfellow, Andrew Harp, Geoffrey Irving, Michael Isard, Yangqing Jia, Rafal Jozefowicz, Lukasz Kaiser, Manjunath Kudlur, Josh Levenberg, Dandelion Mané, Rajat Monga, Sherry Moore, Derek Murray, Chris Olah, Mike Schuster, Jonathon Shlens, Benoit Steiner, Ilya Sutskever, Kunal Talwar, Paul Tucker, Vincent Vanhoucke, Vijay Vasudevan, Fernanda Viégas, Oriol Vinyals, Pete Warden, Martin Wattenberg, Martin Wicke, Yuan Yu, and Xiaoqiang Zheng. TensorFlow: Large-scale machine learning on heterogeneous systems, 2015. Software available from tensorflow.org.

[86] Adam Paszke, Sam Gross, Francisco Massa, Adam Lerer, James Bradbury, Gregory Chanan, Trevor Killeen, Zeming Lin, Natalia Gimelshein, Luca Antiga, Alban Desmaison, Andreas Kopf, Edward Yang, Zachary DeVito, Martin Raison, Alykhan Tejani, Sasank Chilamkurthy, Benoit Steiner, Lu Fang, Junjie Bai, and Soumith Chintala. Pytorch: An imperative style, high-performance deep learning library. In H. Wallach, H. Larochelle, A. Beygelzimer, F. d'Alché-Buc, E. Fox, and R. Garnett, editors, *Advances in Neural Information Processing Systems 32*, pages 8024–8035. Curran Associates, Inc., 2019.

[87] J Roger P Angel, P Wizinowich, M Lloyd-Hart, and D Sandler. Adaptive optics for array telescopes using neural-network techniques. *Nature*, 348(6298):221–224, 1990.

[88] E Keith Hege, Jacques Maurice Beckers, Peter A Strittmatter, and Donald W McCarthy. Multiple mirror telescope as a phased array telescope. *Applied optics*, 24(16):2565–2576, 1985.

[89] Robert A Gonsalves. Phase retrieval and diversity in adaptive optics. *Optical Engineering*, 21(5):215829, 1982.

[90] Scott W Paine and James R Fienup. Machine learning for improved image-based wavefront sensing. *Optics letters*, 43(6):1235–1238, 2018.

[91] Christian Szegedy, Vincent Vanhoucke, Sergey Ioffe, Jon Shlens, and Zbigniew Wojna. Rethinking the inception architecture for computer vision. In *Proceedings of the IEEE conference on computer vision and pattern recognition*, pages 2818–2826, 2016.

[92] Torben Andersen, Mette Owner-Petersen, and Anita Enmark. Neural networks for image-based wavefront sensing for astronomy. *Optics letters*, 44(18):4618–4621, 2019.

[93] Lejia Hu, Shuwen Hu, Wei Gong, and Ke Si. Learning-based Shack-Hartmann wavefront sensor for high-order aberration detection. *Optics Express*, 27(23):33504–33517, 2019.

[94] Yohei Nishizaki, Matias Valdivia, Ryoichi Horisaki, Katsuhisa Kitaguchi, Mamoru Saito, Jun Tanida, and Esteban Vera. Deep learning wavefront sensing. *Optics express*, 27(1):240–251, 2019.

[95] Ralph W Gerchberg. A practical algorithm for the determination of phase from image and diffraction plane pictures. *Optik*, 35:237–246, 1972.

[96] James R Fienup. Phase-retrieval algorithms for a complicated optical system. *Applied optics*, 32(10):1737–1746, 1993.

[97] Andreas Griewank and Andrea Walther. *Evaluating derivatives: principles and techniques of algorithmic differentiation*. SIAM, 2008.

[98] Alden S Jurling and James R Fienup. Applications of algorithmic differentiation to phase retrieval algorithms. *JOSA A*, 31(7):1348–1359, 2014.

[99] Matthew M Loper and Michael J Black. OpenDR: An approximate differentiable renderer. In *European Conference on Computer Vision*, pages 154–169. Springer, 2014.

[100] Felix Petersen, Amit H Bermano, Oliver Deussen, and Daniel Cohen-Or. Pix2vex: Image-to-geometry reconstruction using a smooth differentiable renderer. *arXiv preprint arXiv:1903.11149*, 2019.

[101] Grégoire Nieto, Salma Jiddi, and Philippe Robert. Robust point light source estimation using differentiable rendering. *arXiv preprint arXiv:1812.04857*, 2018.

[102] Merlin Nimier-David, Delio Vicini, Tizian Zeltner, and Wenzel Jakob. Mitsuba 2: A retargetable forward and inverse renderer. *ACM Transactions on Graphics (TOG)*, 38(6):1–17, 2019.

[103] Paige Bailey, Sofien Bouaziz, Shan Carter, Josh Gordon, Christian Häne, Alexander Mordvintsev, Julien Valentin, and Martin Wicke. Differentiable graphics with tensorflow 2.0. In *ACM SIGGRAPH 2019 Courses*, SIGGRAPH '19, New York, NY, USA, 2019. Association for Computing Machinery.

[104] Shubham Tulsiani, Tinghui Zhou, Alexei A Efros, and Jitendra Malik. Multi-view supervision for single-view reconstruction via differentiable ray consistency. In *Proceedings of the IEEE conference on computer vision and pattern recognition*, pages 2626–2634, 2017.

[105] Hiroharu Kato, Yoshitaka Ushiku, and Tatsuya Harada. Neural 3d mesh renderer. In *Proceedings of the IEEE conference on computer vision and pattern recognition*, pages 3907–3916, 2018.

[106] Dmitry Ulyanov, Andrea Vedaldi, and Victor Lempitsky. Deep image prior. In *Proceedings of the IEEE Conference on Computer Vision and Pattern Recognition*, pages 9446–9454, 2018.

[107] Sören Dittmer, Tobias Kluth, Peter Maass, and Daniel Otero Baguer. Regularization by architecture: A deep prior approach for inverse problems. *Journal of Mathematical Imaging and Vision*, 62(3):456–470, 2020.

[108] Kyle Genova, Forrester Cole, Aaron Maschinot, Aaron Sarna, Daniel Vlasic, and William T Freeman. Unsupervised training for 3d morphable model regression. In *Proceedings of the IEEE Conference on Computer Vision and Pattern Recognition*, pages 8377–8386, 2018.

[109] Deniz Beker, Hiroharu Kato, Mihai Adrian Morariu, Takahiro Ando, Toru Matsuoka, Wadim Kehl, and Adrien Gaidon. Monocular differentiable rendering for self-supervised 3d object detection. In *Computer Vision–ECCV 2020: 16th European Conference, Glasgow, UK, August 23–28, 2020, Proceedings, Part XXI 16*, pages 514–529. Springer, 2020.

[110] Georgios Pavlakos, Luyang Zhu, Xiaowei Zhou, and Kostas Daniilidis. Learning to estimate 3d human pose and shape from a single color image. In *Proceedings of the IEEE Conference on Computer Vision and Pattern Recognition*, pages 459–468, 2018.

[111] Filipe de Avila Belbute-Peres, Kevin Smith, Kelsey Allen, Josh Tenenbaum, and J Zico Kolter. End-to-end differentiable physics for learning and control. *Advances in neural information processing systems*, 31:7178–7189, 2018.

[112] Yuanming Hu, Luke Anderson, Tzu-Mao Li, Qi Sun, Nathan Carr, Jonathan Ragan-Kelley, and Frédo Durand. Difftaichi: Differentiable programming for physical simulation. *arXiv preprint arXiv:1910.00935*, 2019.

[113] Samuel Schoenholz and Ekin Dogus Cubuk. Jax md: a framework for differentiable physics. *Advances in Neural Information Processing Systems*, 33, 2020.

[114] Junbang Liang, Ming Lin, and Vladlen Koltun. Differentiable cloth simulation for inverse problems. In H. Wallach, H. Larochelle, A. Beygelzimer, F. d'Alché-Buc, E. Fox, and R. Garnett, editors, *Advances in Neural Information Processing Systems*, volume 32. Curran Associates, Inc., 2019.

[115] Kiwon Um, Robert Brand, Philipp Holl, Nils Thuerey, et al. Solver-in-the-loop: Learning from differentiable physics to interact with iterative pde-solvers. *arXiv preprint arXiv:2007.00016*, 2020.

[116] Philipp Holl, Vladlen Koltun, and Nils Thuerey. Learning to control pdes with differentiable physics. *arXiv preprint arXiv:2001.07457*, 2020.

[117] Eric Heiden, David Millard, Hejia Zhang, and Gaurav S Sukhatme. Interactive differentiable simulation. *arXiv preprint arXiv:1905.10706*, 2019.

[118] Moritz Geilinger, David Hahn, Jonas Zehnder, Moritz Bächer, Bernhard Thomaszewski, and Stelian Coros. Add: analytically differentiable dynamics for multi-body systems with frictional contact. *ACM Transactions on Graphics (TOG)*, 39(6):1–15, 2020.

[119] Youssef SG Nashed, Tom Peterka, Junjing Deng, and Chris Jacobsen. Distributed automatic differentiation for ptychography. *Procedia Computer Science*, 108:404–414, 2017.

[120] Kevin C Zhou and Roarke Horstmeyer. Diffraction tomography with a deep image prior. *Optics Express*, 28(9):12872–12896, 2020.

[121] Fei Wang, Yaoming Bian, Haichao Wang, Meng Lyu, Giancarlo Pedrini, Wolfgang Osten, George Barbastathis, and Guohai Situ. Phase imaging with an untrained neural network. *Light: Science & Applications*, 9(1):1–7, 2020.

[122] Emrah Bostan, Reinhard Heckel, Michael Chen, Michael Kellman, and Laura Waller. Deep phase decoder: self-calibrating phase microscopy with an untrained deep neural network. *Optica*, 7(6):559–562, 2020.

[123] Michael Kellman, Emrah Bostan, Michael Chen, and Laura Waller. Data-driven design for fourier ptychographic microscopy. In *2019 IEEE International Conference on Computational Photography (ICCP)*, pages 1–8. IEEE, 2019.

[124] Huang Linhai and Changhui Rao. Wavefront sensorless adaptive optics: a general model-based approach. *Optics express*, 19(1):371–379, 2011.

[125] Ivan Vishniakou and Johannes D Seelig. Wavefront correction for adaptive optics with reflected light and deep neural networks. *Optics express*, 28(10):15459–15471, 2020.

[126] Ivan Vishniakou and Johannes D Seelig. Differentiable model-based adaptive optics with transmitted and reflected light. *Optics Express*, 28(18):26436–26446, 2020.

[127] Ivan Vishniakou and Johannes D Seelig. Differentiable model-based adaptive optics for two-photon microscopy. *Optics Express*, 29(14):21418–21427, 2021.

[128] Jason N D Kerr and Winfried Denk. Imaging in vivo: watching the brain in action. *Nature Reviews Neuroscience*, 9(3):195, 2008.

[129] Cristina Rodríguez and Na Ji. Adaptive optical microscopy for neurobiology. *Current opinion in neurobiology*, 50:83–91, 2018.

[130] Stefan Rotter and Sylvain Gigan. Light fields in complex media: Mesoscopic scattering meets wave control. *Reviews of Modern Physics*, 89(1):15005, 2017.

[131] Martin J Booth. Adaptive optics in microscopy. *Philosophical Transactions of the Royal Society A: Mathematical, Physical and Engineering Sciences*, 365(1861):2829–2843, 2007.

[132] Andrew K Dunn, Colin Smithpeter, Ashley J Welch, and Rebecca Richards-Kortum. Sources of contrast in confocal reflectance imaging. *Applied optics*, 35(19):3441–3446, 1996.

[133] Sungsam Kang, Pilsung Kang, Seungwon Jeong, Yongwoo Kwon, Taeseok D Yang, Jin Hee Hong, Moonseok Kim, Kyung-Deok Song, Jin Hyoung Park, Jun Ho Lee, and Others. High-resolution adaptive optical imaging within thick scattering media using closed-loop accumulation of single scattering. *Nature communications*, 8(1):2157, 2017.

[134] Seokchan Yoon, Hojun Lee, Jin Hee Hong, Yong-Sik Lim, and Wonshik Choi. Laser scanning reflection-matrix microscopy for label-free in vivo imaging of a mouse brain through an intact skull. *arXiv preprint arXiv:1910.04681*, 2019.

[135] Amaury Badon, Victor Barolle, Kristina Irsch, Albert C Boccara, Mathias Fink, and Alexandre Aubry. Distortion matrix concept for deep imaging in optical coherence microscopy. *arXiv preprint arXiv:1910.07252*, 2019.

[136] Seokchan Yoon, Moonseok Kim, Mooseok Jang, Youngwoon Choi, Wonjun Choi, Sungsam Kang, and Wonshik Choi. Deep optical imaging within complex scattering media. *Nature Reviews Physics*, pages 1–18, 2020.

[137] D G Sandler, T K Barrett, D A Palmer, R Q Fugate, and W J Wild. Use of a neural network to control an adaptive optics system for an astronomical telescope. *Nature*, 351(6324):300, 1991.

[138] Robin Swanson, Masen Lamb, Carlos Correia, Suresh Sivanandam, and Kiriakos Kutulakos. Wavefront reconstruction and prediction with convolutional neural networks. In *Adaptive Optics Systems VI*, volume 10703, page 107031F. International Society for Optics and Photonics, 2018.

[139] Yiye Zhang, Chenxue Wu, Yanchun Song, Ke Si, Yao Zheng, Lejia Hu, Jiajia Chen, Limin Tang, and Wei Gong. Machine learning based adaptive optics for doughnut-shaped beam. *Optics Express*, 27(12):16871–16881, 2019.

[140] Huimin Ma, Haiqiu Liu, Yan Qiao, Xiaohong Li, and Wu Zhang. Numerical study of adaptive optics compensation based on Convolutional Neural Networks. *Optics Communications*, 433:283–289, 2019.

[141] Yuncheng Jin, Yiye Zhang, Lejia Hu, Haiyang Huang, Qiaoqi Xu, Xinpei Zhu, Limeng Huang, Yao Zheng, Hui-Liang Shen, Wei Gong, and Others. Machine learning guided rapid focusing with sensor-less aberration corrections. *Optics express*, 26(23):30162–30171, 2018.

[142] Yangjie Xu, Dong He, Qiang Wang, Hongyang Guo, Qing Li, Zongliang Xie, and Yongmei Huang. An Improved Method of Measuring Wavefront Aberration Based on Image with Machine Learning in Free Space Optical Communication. *Sensors*, 19(17):3665, 2019.

[143] Bridget M Hanser, Mats G L Gustafsson, David A Agard, and John W Sedat. Phase retrieval for high-numerical-aperture optical systems. *Optics letters*, 28(10):801–803, 2003.

[144] Luis Miguel Sanchez Brea. Diffractio, python module for diffraction and interference optics. `https://pypi.org/project/diffractio/`, 2019.

[145] Leonhard Möckl, Petar N Petrov, and W E Moerner. Accurate phase retrieval of complex point spread functions with deep residual neural networks. *arXiv preprint arXiv:1906.01748*, 2019.

[146] Alex Turpin, Ivan Vishniakou, and Johannes D Seelig. Light scattering control in transmission and reflection with neural networks. *Optics express*, 26(23):30911–30929, 2018.

[147] Shengfu Cheng, Huanhao Li, Yunqi Luo, Yuanjin Zheng, Puxiang Lai, and Others. Artificial intelligence-assisted light control and computational imaging through scattering media. *Journal of Innovative Optical Health Sciences*, 12(4):1930006, 2019.

[148] Robert A Gonsalves. Perspectives on phase retrieval and phase diversity in astronomy. In *Adaptive Optics Systems IV*, volume 9148, page 91482P. International Society for Optics and Photonics, 2014.

[149] H Song, R Fraanje, G Schitter, H Kroese, G Vdovin, and M Verhaegen. Model-based aberration correction in a closed-loop wavefront-sensor-less adaptive optics system. *Optics express*, 18(23):24070–24084, 2010.

[150] Huizhen Yang, Oleg Soloviev, and Michel Verhaegen. Model-based wavefront sensorless adaptive optics system for large aberrations and extended objects. *Optics express*, 23(19):24587–24601, 2015.

[151] Jacopo Antonello and Michel Verhaegen. Modal-based phase retrieval for adaptive optics. *JOSA A*, 32(6):1160–1170, 2015.

[152] Gregory Ongie, Ajil Jalal, Christopher A Metzler Richard G Baraniuk, Alexandros G Dimakis, and Rebecca Willett. Deep learning techniques for inverse problems in imaging. *IEEE Journal on Selected Areas in Information Theory*, 2020.

[153] Tzu-Mao Li, Miika Aittala, Frédo Durand, and Jaakko Lehtinen. Differentiable monte carlo ray tracing through edge sampling. *ACM Transactions on Graphics (TOG)*, 37(6):1–11, 2018.

[154] Jonas Degrave, Michiel Hermans, Joni Dambre, and Francis Wyffels. A differentiable physics engine for deep learning in robotics. *Frontiers in neurorobotics*, 13:6, 2019.

[155] Eric Heiden, Ziang Liu, Ragesh K Ramachandran, and Gaurav S Sukhatme. Physics-based Simulation of Continuous-Wave LIDAR for Localization, Calibration and Tracking. *arXiv preprint arXiv:1912.01652*, 2019.

[156] Atilim Gunes Baydin, Barak A Pearlmutter, Alexey Andreyevich Radul, and Jeffrey Mark Siskind. Automatic differentiation in machine learning: a survey. *Journal of machine learning research*, 18, 2018.

[157] Charles C Margossian. A review of automatic differentiation and its efficient implementation. *Wiley Interdisciplinary Reviews: Data Mining and Knowledge Discovery*, 9(4):e1305, 2019.

[158] Lu Lu, Xuhui Meng, Zhiping Mao, and George E Karniadakis. DeepXDE: A deep learning library for solving differential equations. *arXiv preprint arXiv:1907.04502*, 2019.

[159] François Rigaut and Benoit Neichel. Multiconjugate adaptive optics for astronomy. *Annual Review of Astronomy and Astrophysics*, 56:277–314, 2018.

[160] Zvi Kam, Peter Kner, David Agard, and John W Sedat. Modelling the application of adaptive optics to wide-field microscope live imaging. *Journal of microscopy*, 226(1):33–42, 2007.

[161] Jörgen Thaung, Per Knutsson, Zoran Popovic, and Mette Owner-Petersen. Dual-conjugate adaptive optics for wide-field high-resolution retinal imaging. *Optics express*, 17(6):4454–4467, 2009.

[162] Reinhard Heckel and Mahdi Soltanolkotabi. Denoising and Regularization via Exploiting the Structural Bias of Convolutional Generators. *arXiv preprint arXiv:1910.14634*, 2019.

[163] Steven L Brunton, Bernd R Noack, and Petros Koumoutsakos. Machine learning for fluid mechanics. *Annual Review of Fluid Mechanics*, 52:477–508, 2020.

[164] Ivo M Vellekoop. Feedback-based wavefront shaping. *Optics express*, 23(9):12189–12206, 2015.

[165] Stuart M Jefferies, Michael Lloyd-Hart, E Keith Hege, and James Georges. Sensing wave-front amplitude and phase with phase diversity. *Applied optics*, 41(11):2095–2102, 2002.

[166] Bridget M Hanser, Mats GL Gustafsson, DA Agard, and John W Sedat. Phase-retrieved pupil functions in wide-field fluorescence microscopy. *Journal of microscopy*, 216(1):32–48, 2004.

[167] Markus Giftthaler, Michael Neunert, Markus Stäuble, Marco Frigerio, Claudio Semini, and Jonas Buchli. Automatic differentiation of rigid body dynamics for optimal control and estimation. *Advanced Robotics*, 31(22):1225–1237, 2017.

[168] Connor Schenck and Dieter Fox. Spnets: Differentiable fluid dynamics for deep neural networks. *arXiv preprint arXiv:1806.06094*, 2018.

[169] Alexander Song, Jeff L Gauthier, Jonathan W Pillow, David W Tank, and Adam S Charles. Neural Anatomy and Optical Microscopy (NAOMi) Simulation for evaluating calcium imaging methods. *Journal of Neuroscience Methods*, page 109173, 2021.

[170] Claudio Vinegoni, Paolo Fumene Feruglio, and Ralph Weissleder. High dynamic range fluorescence imaging. *IEEE Journal of Selected Topics in Quantum Electronics*, 25(1):1–7, 2018.

[171] Nguyen Hieu Thao, Oleg Soloviev, and Michel Verhaegen. Phase retrieval based on the vectorial model of point spread function. *JOSA A*, 37(1):16–26, 2020.

[172] Torben Andersen, Mette Owner-Petersen, and Anita Enmark. Image-based wavefront sensing for astronomy using neural networks. *Journal of Astronomical Telescopes, Instruments, and Systems*, 6(3):34002, 2020.

[173] Debayan Saha, Uwe Schmidt, Qinrong Zhang, Aurelien Barbotin, Qi Hu, Na Ji, Martin J Booth, Martin Weigert, and Eugene W Myers. Practical sensorless aberration estimation for 3d microscopy with deep learning. *Optics express*, 28(20):29044–29053, 2020.

[174] Rafael Navarro and M Angeles Losada. Phase transfer and point-spread function of the human eye determined by a new asymmetric double-pass method. *JOSA A*, 12(11):2385–2392, 1995.

[175] Tomoyoshi Shimobaba, Kyoji Matsushima, Takashi Kakue, Nobuyuki Masuda, and Tomoyoshi Ito. Scaled angular spectrum method. *Optics letters*, 37(19):4128–4130, 2012.

[176] Emil Wolf. Electromagnetic diffraction in optical systems – i. an integral representation of the image field. *Proceedings of the Royal Society of London. Series A. Mathematical and Physical Sciences*, 253(1274):349–357, 1959.

[177] Iksung Kang, Alexandre Goy, and George Barbastathis. Dynamical machine learning volumetric reconstruction of objects' interiors from limited angular views. *Light: Science & Applications*, 10(1):1–21, 2021.

[178] Lina Streich, Juan Carlos Boffi, Ling Wang, Khaleel Alhalaseh, Matteo Barbieri, Ronja Rehm, Senthilkumar Deivasigamani, Cornelius T Gross, Amit Agarwal, and Robert Prevedel. High-resolution structural and functional deep brain imaging using adaptive optics three-photon microscopy. *Nature Methods*, 18(10):1253–1258, 2021.

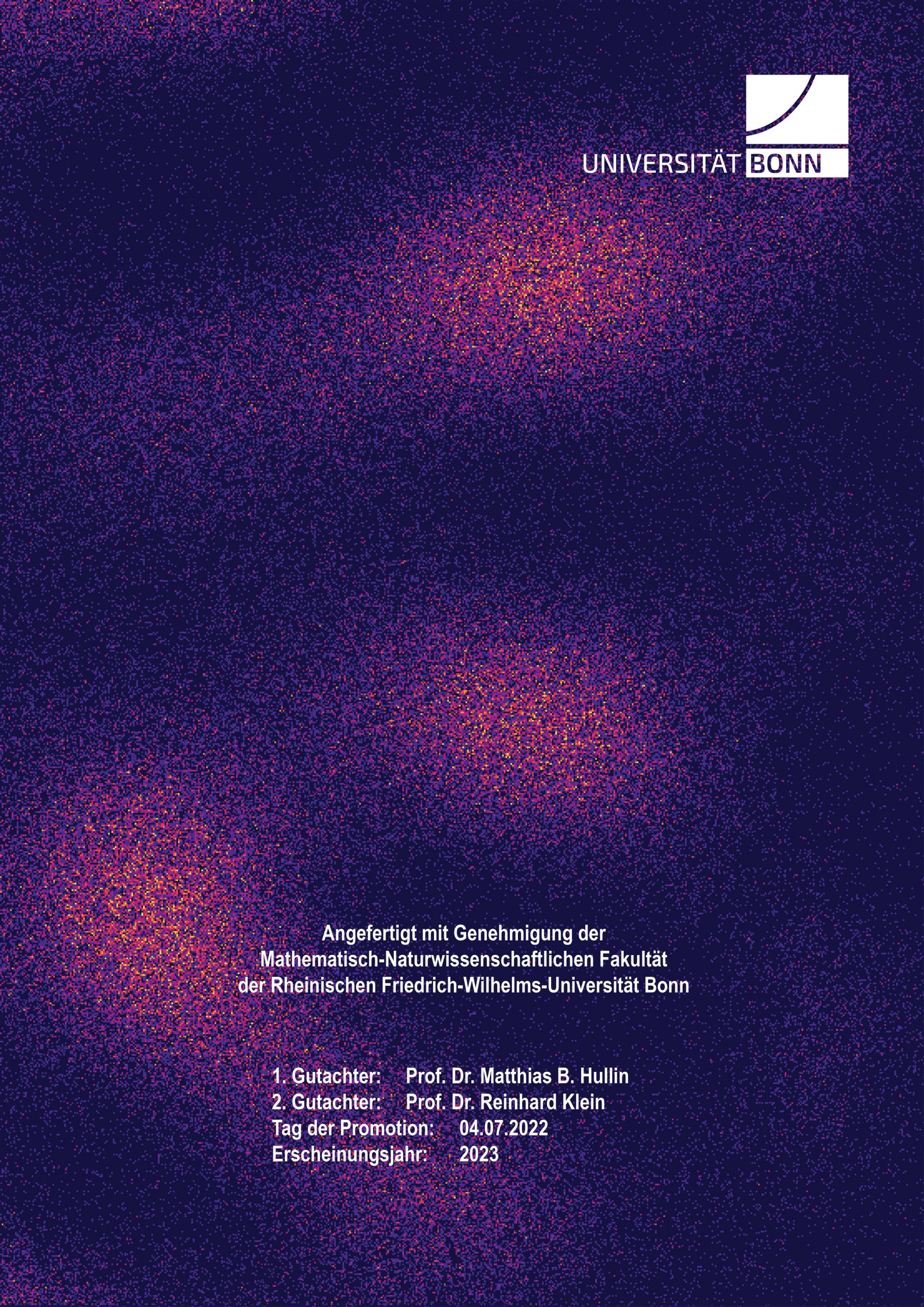

Angefertigt mit Genehmigung der
Mathematisch-Naturwissenschaftlichen Fakultät
der Rheinischen Friedrich-Wilhelms-Universität Bonn

1. Gutachter: Prof. Dr. Matthias B. Hullin
2. Gutachter: Prof. Dr. Reinhard Klein
Tag der Promotion: 04.07.2022
Erscheinungsjahr: 2023